Karlsruhe Institute of Technology

Collocated versus staggered grid Finite Difference modeling in isotropic elastic media

Master's thesis of

Zuoyi Shi

at the Geophysical Institute (GPI)
KIT-Department of Physics
Karlsruhe Institute of Technology (KIT)

Date of submission:
30.03.2026

Supervisor: Prof. Dr. Thomas Bohlen
Co-supervisor: apl. Prof. Dr. Joachim Ritter

Abstract

Seismic modeling simulates wave propagation to understand the Earth's subsurface and predict ground motion. The finite difference (FD) method is a key numerical approach for its efficiency in seismic modeling. Among the FD methods, the staggered-grid FD (SG-FD, also called velocity-stress finite-difference) method is widely used for its accuracy in seismic wave simulations. However, the wavefield interpolation in anisotropic media significantly increases computational time. The wavefield interpolation is performed in every timestep, which requires more runtime and memory usage. The collocated-grid FD (CG-FD) method, avoiding interpolation, offers a potential alternative approach.

This thesis presents a systematic comparison between CG-FD and SG-FD methods for 2D wave propagation in isotropic media. The CG-FD schemes are separated into acoustic and elastic cases, while the SG-FD scheme works for both cases. The simplified versions for homogeneous media are also provided.

The comparison covers stability and numerical dispersion. Based on plane-wave analysis, the derivation of the formulas for the stability limit and numerical dispersion relation is provided in this thesis. For the CG-FD scheme, the stability limit formulas for arbitrary orders of spatial accuracy are proposed in this thesis. The grid scan method is used to find the global stability limit boundary, and the results are verified. Furthermore, the stability boundary of the acoustic CG-FD is explicitly compared with the traditional stability limit. For elastic CG-FD, the stability limit and numerical dispersion depend on the S-wave to P-wave velocity ratio. In addition, an accuracy analysis of numerical dispersion is provided.

A homogeneous model and a two-layer model are used for simulating the snapshots and seismograms of the wavefield. In the results of the homogeneous model, the seismograms are compared with the analytical solution. In the results of the heterogeneous model, a comparison between CG-FD and SG-FD is provided.

The results show that, in the acoustic case, CG-FD and SG-FD exhibit nearly identical dispersion behavior and comparable numerical accuracy. In the elastic case, CG-FD provides a less restrictive stability limit than SG-FD but suffers from stronger directional numerical dispersion, especially for diagonal wave propagation and smaller S-wave to P-wave velocity ratios. These findings indicate that CG-FD can serve as a feasible alternative to SG-FD in isotropic media, although a higher order of spatial accuracy is generally required to achieve comparable dispersion performance. The study provides a basis for future extensions to anisotropic media.

List of Figures

Contents

Chapter 1

Introduction

Accurate and efficient numerical simulation of seismic wave propagation is a core requirement in seismic imaging and inversion. In realistic subsurface models, wave equations need to be solved to predict the full wavefield in heterogeneous media (Kosloff and Baysal, 1982; Moczo, Robertsson, et al., 2007). Among existing numerical approaches, the finite difference (FD) method remains one of the most widely used due to its direct solution of the wave equations, high computational efficiency, and high accuracy (Virieux, 1986; Moczo, Robertsson, et al., 2007; Igel, 2017). FD modeling of seismic wave propagation can be traced back to early layered-medium studies such as Alterman and Karal Jr (1968), and it was subsequently developed into a broader computational framework for heterogeneous media by later work such as Boore (1972).

For elastic-wave modeling, staggered-grid finite-difference (SG-FD) schemes based on the first-order velocity–stress formulation are widely used for their accuracy in seismic wave simulations. Virieux (1984, 1986) established the second-order SG-FD formulations for SH-wave and P–SV wave propagation in heterogeneous media, and Levander (1988) extended the P–SV formulation to fourth-order spatial accuracy. Later work further analyzed the stability and numerical dispersion of staggered-grid schemes and improved their performance through higher-orders accuracy or optimized coefficients (Moczo, Kristek, et al., 2000; Liu and Sen, 2011; Tan and Huang, 2014). Because stress and particle-velocity components are stored at different spatial locations, SG-FD schemes generally exhibit favorable stability and numerical dispersion behavior (Virieux, 1986; Moczo, Kristek, et al., 2000; Moczo, Robertsson, et al., 2007).

At the same time, collocated-grid finite-difference (CG-FD) formulations remain attractive because all parameters are stored at the same grid points. In seismology, second-order displacement-stress formulations on collocated grids were already used in early synthetic-seismogram studies (Kelly et al., 1976; Marfurt, 1984). However, compared with SG-FD, collocated-grid formulations for elastic-wave propagation are often regarded as being more sensitive to numerical dispersion or suffer from unphysical oscillations (Marfurt, 1984; Moczo, Robertsson, et al., 2007).

When moving from isotropic to anisotropic media, the systematic re-evaluation on CG-FD becomes more important. In anisotropic modeling, the complexity of the medium necessitates parameter averaging or awkward interpolation, increasing computational load. To improve this, existing research has refined grid arrangements and parameter placement, leading to the development of several alternative staggered grid layouts—such as rotated staggered grid and Lebedev-type grid (Saenger, Gold, et al., 2000; Saenger and Bohlen, 2004; Lisitsa and Vishnevskiy, 2010; Gao and Huang, 2017; Koene et al., 2021). Recent

work on 3D anisotropic FD modeling on standard staggered grids likewise highlights the additional implementation cost caused by wavefield interpolation and parameter placement issues (Mai, 2024). These developments motivate a renewed assessment of whether a collocated-grid strategy can provide an alternative approach, provided that its theoretical properties are first clarified in the simpler isotropic case.

Despite the long history of FD modeling, a systematic and direct comparison of the stability limit and numerical dispersion behavior between CG-FD and SG-FD for 2D isotropic acoustic and elastic wave propagation at different spatial orders remains useful. This thesis focuses on the isotropic case for a clear comparison of different grid arrangements, as it eliminates the confounding factors associated with anisotropy. It allows stability limits and numerical dispersion to be analyzed in a controlled setting and compared against analytical or benchmark solutions. It provides the theoretical and numerical baseline needed before extending CG-FD formulations to anisotropic media, where the potential benefits of collocated placement may become more pronounced. Furthermore, it is essential to investigate both acoustic and elastic formulations. The acoustic equations describe scalar wave propagation, whereas the elastic equations involve coupled P- and S-waves, leading to fundamentally different stability and dispersion behaviors for the CG-FD method.

The aim of this thesis is to compare CG-FD and SG-FD for 2D wave propagation in isotropic media from both theoretical and numerical perspectives. The comparison spans both acoustic and elastic formulations across homogeneous and heterogeneous models. First, we systematically analyze the theoretical properties, including stability limits, numerical dispersion relations, and accuracy analysis. Then, we validate these theoretical findings numerically through wavefield snapshots and seismograms. For the CG-FD scheme, Marfurt (1984) only derives the second-order accuracy stability-limit expressions for elastic cases. For the acoustic case, Lines et al. (1999) provides a generalized stability-limit expression derived from von Neumann analysis as a sufficient condition. This thesis develops the stability-limit expressions for arbitrary orders of spatial accuracy in the isotropic acoustic and elastic cases and evaluates their global bounds numerically using a grid-scan procedure. These results are then compared with those of the SG-FD scheme. Particular attention is paid to directional numerical dispersion and the role of the velocity ratio $\gamma = v_s/v_p$, because this parameter strongly influences the simulated quality.

The main findings can be summarized as follows. In the acoustic case, CG-FD and SG-FD show very similar numerical dispersion behavior and comparable stability limits. In the elastic case, CG-FD admits a less restrictive stability limit than SG-FD, but it exhibits stronger dispersion, especially for diagonal propagation and for smaller values of γ. These results indicate that CG-FD can serve as a feasible alternative to SG-FD in isotropic media, although it generally requires a higher order of spatial accuracy to achieve comparable dispersion performance. Beyond the immediate isotropic comparison, the results establish a foundation for future extensions to anisotropic media.

The remainder of this thesis is organized as follows. Chapter 2 introduces the wave equations for isotropic acoustic and elastic wave propagation in homogeneous and heterogeneous media. Chapter 3 presents the FD operators and the numerical implementation of the CG-FD and SG-FD schemes. Chapter 4 derives the stability conditions and numerical dispersion relations. Chapter 5 evaluates these theoretical properties numerically. Chapter 6 compares both schemes in homogeneous models using snapshots, seismograms, and analytical solutions. Chapter 7 presents results for a simple heterogeneous two-layer model. Finally, chapter 8 summarizes the main conclusions and outlines directions for future work. To facilitate the reproduction of the results presented in this thesis, the complete MATLAB source code is publicly available on GitHub (Shi, 2026).

Chapter 2

Wave Theory

This chapter describes the two fundamental equations of wave theory: the equation of motion and the isotropic stress–strain relation. Based on these two equations, the second-order wave equation can be derived for the collocated-grid (CG) finite-difference (FD) method, while the first-order wave equations are obtained for the staggered-grid (SG) finite-difference (FD) method. The SG-FD method is also commonly referred to as the velocity–stress finite-difference method.

For the second-order equations, this section presents the elastic and acoustic wave equations for the elastic and acoustic cases, respectively. Different versions are also provided for homogeneous and heterogeneous media.

For the first-order equations, only one version is provided, which can be used for both elastic and acoustic cases as well as for both homogeneous and heterogeneous media.

2.1 Basic equations

2.1.1 Equation of motion

The equation of motion is derived from Newton's second law. It describes the motion of particles in a medium. The equation is written as (Lay and Wallace, 1995, eq. 2.37)

$$\rho \frac{\partial^2 u_i}{\partial t^2} = \frac{\partial \sigma_{ij}}{\partial x_j} + f_i. \tag{2.1}$$

In eq. 2.1: ρ is the density of the medium; u_i and σ_{ij} are the components of the displacement vector and the stress tensor, respectively; f_i corresponds to the external body force; $i, j = 1, 2, 3$ correspond to the x_1, x_2, x_3 axes of the Cartesian coordinate system, respectively. The equation describes the balance of forces between inertial force, total internal force, and additional force.

We convert the displacement into the velocity using $v_i = \partial u_i / \partial t$. Eq. 2.1 can be written in first-order form as follows:

$$\rho \frac{\partial v_i}{\partial t} = \frac{\partial \sigma_{ij}}{\partial x_j} + f_i. \tag{2.2}$$

This thesis adopts the Einstein summation convention, which implies summation over repeated subscripts. For example, the stress derivative term in eq. 2.1 is expanded as

$$\frac{\partial \sigma_{ij}}{\partial x_j} = \sum_{j=1}^{3} \frac{\partial \sigma_{ij}}{\partial x_j} = \frac{\partial \sigma_{i1}}{\partial x_1} + \frac{\partial \sigma_{i2}}{\partial x_2} + \frac{\partial \sigma_{i3}}{\partial x_3}. \tag{2.3}$$

2.1.2 Isotropic stress–strain relation

The stress–strain relation is derived from Hooke's law. It describes the elastic properties of the medium. For a linear isotropic elastic medium, the stress–strain relationship is (Lay and Wallace, 1995, eq. 2.44):

$$\sigma_{ij} = \lambda\theta\delta_{ij} + 2\mu\epsilon_{ij}, \tag{2.4}$$

where λ and μ are the Lamé parameters, representing the material properties. μ is also called the shear modulus. θ is the cubic dilatation, expressed as: $\theta = \epsilon_{11} + \epsilon_{22} + \epsilon_{33}$. δ_{ij} is the Kronecker delta. ϵ_{ij} is called the deformation tensor, which is described as $\epsilon_{ij} = 1/2 \cdot (\partial u_i/\partial x_j + \partial u_j/\partial x_i)$.

2.2 Elastic wave equations for heterogeneous media

2.2.1 2D first-order elastic wave equations for staggered grid

This thesis only considers the two-dimensional (2D) x_1–x_2 case ($i, j = 1, 2$). In section 3.3, the first-order wave equations are required for the velocity-stress finite-difference method, which uses a staggered grid. By combining eq. 2.2 with the time derivative of eq. 2.4, the resulting equations are expressed as (Virieux, 1986, eq. 2)

$$\begin{aligned}
\rho\frac{\partial v_1}{\partial t} &= \frac{\partial \sigma_{11}}{\partial x_1} + \frac{\partial \sigma_{12}}{\partial x_2} + f_1, \\
\rho\frac{\partial v_2}{\partial t} &= \frac{\partial \sigma_{12}}{\partial x_1} + \frac{\partial \sigma_{22}}{\partial x_2} + f_2, \\
\frac{\partial \sigma_{11}}{\partial t} &= (\lambda + 2\mu)\frac{\partial v_1}{\partial x_1} + \lambda\frac{\partial v_2}{\partial x_2}, \\
\frac{\partial \sigma_{22}}{\partial t} &= (\lambda + 2\mu)\frac{\partial v_2}{\partial x_2} + \lambda\frac{\partial v_1}{\partial x_1}, \\
\frac{\partial \sigma_{12}}{\partial t} &= \mu\left(\frac{\partial v_1}{\partial x_2} + \frac{\partial v_2}{\partial x_1}\right),
\end{aligned} \tag{2.5}$$

which can describe the P-SV wave propagation in 2D heterogeneous media. For heterogeneous media, the material parameters λ, μ, and the density ρ are spatially dependent; i.e., $\lambda = \lambda(x_1, x_2)$, $\mu = \mu(x_1, x_2)$, and $\rho = \rho(x_1, x_2)$. This principle applies to all other wave equations for heterogeneous media in this thesis.

2.2.2 2D second-order elastic wave equation for collocated grid

We combine the equation of motion and the isotropic stress–strain relation to obtain the second-order elastic wave equation. The 2D elastic wave equation for isotropic heterogeneous media is written as

$$\begin{aligned}
\rho\frac{\partial^2 u_1}{\partial t^2} &= (\lambda + 2\mu)\left(\frac{\partial^2 u_1}{\partial x_1^2} + \frac{\partial^2 u_2}{\partial x_1 \partial x_2}\right) + \mu\left(\frac{\partial^2 u_1}{\partial x_2^2} - \frac{\partial^2 u_2}{\partial x_1 \partial x_2}\right) \\
&\quad + \frac{\partial \lambda}{\partial x_1}\left(\frac{\partial u_1}{\partial x_1} + \frac{\partial u_2}{\partial x_2}\right) + \frac{\partial \mu}{\partial x_2}\left(\frac{\partial u_1}{\partial x_2} + \frac{\partial u_2}{\partial x_1}\right) + 2\frac{\partial \mu}{\partial x_1}\frac{\partial u_1}{\partial x_1} + f_1, \\
\rho\frac{\partial^2 u_2}{\partial t^2} &= (\lambda + 2\mu)\left(\frac{\partial^2 u_2}{\partial x_2^2} + \frac{\partial^2 u_1}{\partial x_1 \partial x_2}\right) + \mu\left(\frac{\partial^2 u_2}{\partial x_1^2} - \frac{\partial^2 u_1}{\partial x_1 \partial x_2}\right) \\
&\quad + \frac{\partial \lambda}{\partial x_2}\left(\frac{\partial u_1}{\partial x_1} + \frac{\partial u_2}{\partial x_2}\right) + \frac{\partial \mu}{\partial x_1}\left(\frac{\partial u_1}{\partial x_2} + \frac{\partial u_2}{\partial x_1}\right) + 2\frac{\partial \mu}{\partial x_2}\frac{\partial u_2}{\partial x_2} + f_2.
\end{aligned} \tag{2.6}$$

Note that the terms corresponding to $(\lambda + 2\mu)$ and μ in eq. 2.6 govern the P-wave and S-wave propagation behavior, respectively. This is why no further simplification is performed here. Furthermore, the equation includes several terms involving the spatial derivatives of λ, μ and ρ, which contain the contribution of medium heterogeneity to wave propagation.

2.3 Acoustic wave equations for heterogeneous media

Apart from the elastic case, this thesis considers the acoustic cases. For SG-FD, we still use first-order elastic wave equations for the acoustic case, but the shear modulus μ vanishes. For CG-FD, in the acoustic case, the second-order acoustic wave equation is used. Besides $\mu = 0$, the stress tensor reduces to a hydrostatic state, i.e., $\sigma_{ij} = -p\delta_{ij}$, where p is a scalar pressure, and the negative sign means the pressure is compressional. Based on the above assumptions, the form for heterogeneous media is written as (Tarantola, 1984, eq. 1)

$$\frac{1}{\lambda}\frac{\partial^2 p}{\partial t^2} = \nabla \cdot \left(\frac{1}{\rho}\nabla p\right) + s. \tag{2.7}$$

In this thesis we only consider the 2D situation. Therefore, eq. 2.7 can be written as

$$\frac{1}{\lambda}\frac{\partial^2 p}{\partial t^2} = \frac{\partial p}{\partial x_1}\frac{\partial}{\partial x_1}\left(\frac{1}{\rho}\right) + \frac{1}{\rho}\frac{\partial^2 p}{\partial x_1^2} + \frac{\partial p}{\partial x_2}\frac{\partial}{\partial x_2}\left(\frac{1}{\rho}\right) + \frac{1}{\rho}\frac{\partial^2 p}{\partial x_2^2} + s, \tag{2.8}$$

which will be used for the acoustic approximation of CG-FD in heterogeneous media.

2.4 Simplification of equations in homogeneous media

For homogeneous media, the above wave equations still work, but they can be simplified for faster numerical simulation. For SG-FD, we still apply eq. 2.5 for homogeneous media. For CG-FD, the elastic and acoustic wave equations are simplified in this section.

2.4.1 2D second-order elastic wave equation for homogeneous media

For a homogeneous medium, ρ, λ, and μ are spatially invariant, i.e., $\partial\lambda/\partial x_i = 0$ and $\partial\mu/\partial x_i = 0$. Therefore, eq. 2.6 simplifies to the 2D second-order elastic wave equation for homogeneous media (Kelly et al., 1976, eq. 1):

$$\begin{aligned}
\rho\frac{\partial^2 u_1}{\partial t^2} &= (\lambda + 2\mu)\left(\frac{\partial^2 u_1}{\partial x_1^2} + \frac{\partial^2 u_2}{\partial x_1 \partial x_2}\right) + \mu\left(\frac{\partial^2 u_1}{\partial x_2^2} - \frac{\partial^2 u_2}{\partial x_1 \partial x_2}\right) + f_1, \\
\rho\frac{\partial^2 u_2}{\partial t^2} &= (\lambda + 2\mu)\left(\frac{\partial^2 u_2}{\partial x_2^2} + \frac{\partial^2 u_1}{\partial x_1 \partial x_2}\right) + \mu\left(\frac{\partial^2 u_2}{\partial x_1^2} - \frac{\partial^2 u_1}{\partial x_1 \partial x_2}\right) + f_2.
\end{aligned} \tag{2.9}$$

Furthermore, eq. 2.9 can be simplified as (Lay and Wallace, 1995, eq. 2.52)

$$\rho\frac{\partial^2 \mathbf{u}}{\partial t^2} = (\lambda + 2\mu)\nabla(\nabla \cdot \mathbf{u}) - \mu\nabla \times (\nabla \times \mathbf{u}) + \mathbf{f}, \tag{2.10}$$

which is the standard form widely used in elastic wave theory.

2.4.2 2D acoustic wave equation for homogeneous media

For the homogeneous media, there is no spatial variation in λ and ρ, i.e., $\partial(1/\rho)/\partial x_i = 0$. Eq. 2.8 can be rewritten as

$$\frac{\partial^2 p}{\partial t^2} = \alpha^2\left(\frac{\partial^2 p}{\partial x_1^2} + \frac{\partial^2 p}{\partial x_2^2}\right) + s, \tag{2.11}$$

where $\alpha = \sqrt{\lambda/\rho}$ is the P-wave velocity in the acoustic case.

2.5 Sources

This section discusses two different sources for the acoustic and elastic cases. Specifically, it introduces the Ricker wavelet and its integrated form as a source, which are essential for aligning the waveforms when comparing results between the CG-FD and SG-FD methods.

2.5.1 Pressure source & force source

This thesis considers both the elastic case and the acoustic case, which employ different sources. For the elastic case, we can apply a point vertical or horizontal force source to simulate directional excitation underground, which typically represents an impulsive seismic source. Note that in this thesis, the force source used here is a vertical source. For the acoustic case, the source is typically provided by air guns, which generate compressed air in the water. Therefore, we employ a pressure source for the acoustic case. Because the numerical models considered here are solid media, when we apply a pressure source, we actually implement an acoustic approximation.

2.5.2 Ricker wavelet & its integrated form

The Ricker wavelet is adopted as the source waveform for the finite-difference method with the collocated grid. The mathematical expression is given by:

$$\begin{aligned} s &= (1 - 2\tau^2)e^{-\tau^2}, \\ \tau &= \pi(t - t_d)f_c, \\ t_d &= 1/f_c, \end{aligned} \tag{2.12}$$

where f_c is the central frequency of the Ricker wavelet. In this thesis, f_c of all the sources in all the methods is 80 Hz.

Since the particle velocity in SG-FD is the time derivative of displacement in CG-FD, integrating the source wavelet in the velocity-stress formulation yields the same physical response as the original wavelet in the displacement formulation. In order to ensure a consistent source representation, we use the integrated form of the Ricker wavelet as a source for SG-FD to match the waveform characteristics of the collocated grid finite-difference method. The expression is given by:

$$\begin{aligned} s &= \tau e^{-\tau^2}, \\ \tau &= \pi(t - t_d)f_c, \\ t_d &= 1/f_c. \end{aligned} \tag{2.13}$$

In eq. 2.12 and 2.13, t_d represents the time delay, which is set to ensure that the source amplitude starts from zero at the initial physical time ($t = 0$). Without this delay, when applying the simulation, a sudden amplitude step would occur, injecting high-frequency numerical artifacts into the simulation. Typically, t_d is set to $1/f_c$. However, there is also a time shift during the actual simulation, which will be discussed in detail in section 3.3.1.

Chapter 3

Finite-Difference Theory & Implementation

The finite-difference (FD) method is one of the direct methods that solve the full wave equation. It uses the values of surrounding points to approximate the derivatives at each grid point, thus solving partial differential equations (PDEs) through iterative formulas. Igel (2017) provides derivations for second-order accuracy 2D FD schemes, including acoustic CG-FD and elastic SG-FD. Based on this, this chapter introduces the arbitrary orders of accuracy 2D schemes of both SG-FD and CG-FD, including both acoustic and elastic cases. Some theory for implementation is also introduced.

3.1 Finite-Difference operators and coefficients

The construction of the finite-difference scheme for the wave equation depends on the discretization of the derivative term. To obtain a discrete approximation of the derivative terms, this section utilizes the Taylor series expansion of spatially symmetric points for combinations. By adding or subtracting p_m and p_{-m}, odd-order or even-order interference terms can be selectively eliminated, thereby constructing a system of linear equations for solving the undetermined coefficients (Cynar, 1987, eq. 4 and 7).

3.1.1 Second-order normal derivative operator (for CG)

Time and space are discretized into the numerical spectral and temporal grids, i.e., for any continuous parameter p, we have $p(x, y, t) = p(ih, jh, n\Delta t)$, which is displayed by $p[i, j, n]$ or $p^n_{i,j}$ in this thesis. i, j, n represent the numbers of grid points, and h, Δt are the grid spacing and time step, respectively. Consider an arbitrary point as point zero, with a value of p_0. The value of a neighboring point, located at a distance of mh from point zero, is p_m. p_m can be calculated using a Taylor series expansion. p_m and p_{-m} are given as

$$\begin{aligned} p_m &= p_0 + mh\,p' + \frac{m^2h^2}{2}p'' + \sum_{k=3}^{N}\frac{m^k h^k p^{(k)}}{k!}, \\ p_{-m} &= p_0 - mh\,p' + \frac{m^2h^2}{2}p'' + \sum_{k=3}^{N}\frac{(-m)^k h^k p^{(k)}}{k!}. \end{aligned} \tag{3.1}$$

By summing p_m and p_{-m}, the odd-order derivatives in the Taylor series expansion are

eliminated, resulting in the relationship between p_{-m}, p_m, p_0, and p'':

$$m^2 p'' = \frac{p_m + p_{-m} - 2p_0}{h^2} - \frac{2}{h^2}\sum_{k=2}^{N}\frac{p^{(2k)}m^{2k}h^{2k}}{(2k)!} = \frac{p_m + p_{-m} - 2p_0}{h^2} + o(h^2). \tag{3.2}$$

This provides a second-order derivative approximation in space. Similarly, a second-order derivative approximation can be obtained in time. Applying a scale coefficient called the FD coefficient a_m to each term of eq. 3.2. a_m satisfies

$$\sum_{m=1}^{M} m^2 a_m = 1, \quad \sum_{m=1}^{M} m^{2k} a_m = 0, \quad k = 2, \ldots, M. \tag{3.3}$$

There are M equations corresponding to M unknowns a_m. Therefore, for different M, a set of solutions for a_m can be obtained. This procedure eliminates the terms with $m^{2k}, k = 2, ...M$, in the Taylor expansion. The truncation error improves from $o(h^2)$ to $o(h^{2M})$; i.e., the order of accuracy is determined by the spatial accuracy order $2M$. Similarly, it can be applied over time with a temporal order N. The overall order of accuracy is denoted as $O(N, 2M)$. In this work, the FD coefficient is applied only in space, so the method is of accuracy order $O(2, 2M)$. Therefore, in this thesis, for example, if the second-order accuracy is mentioned, it means $2M = 2$.

If we consider p at an arbitrary grid point (i, j), the second-order derivative approximation can be obtained from eq. 3.2 as:

$$\frac{\partial^2 p[i,j]}{\partial x_i^2} \approx \sum_{m=1}^{M} a_m \frac{p[i+m,j] + p[i-m,j] - 2p[i,j]}{h^2}. \tag{3.4}$$

3.1.2 First-order & second-order mixed derivative operator (for CG)

Starting from eq. 3.1, the relationship of p_m, p_{-m}, and p' can be expressed as

$$mp' = \frac{p_m - p_{-m}}{2h} - \frac{1}{h}\sum_{k=2}^{N}\frac{m^{2k-1}h^{2k-1}p^{(2k-1)}}{(2k-1)!} = \frac{p_m - p_{-m}}{2h} + o(h^2). \tag{3.5}$$

Apply the FD coefficient b_m to each term. b_m satisfies

$$\sum_{m=1}^{M} m b_m = 1, \quad \sum_{m=1}^{M} m^{2k-1} b_m = 0, \quad k = 2, \ldots, M. \tag{3.6}$$

There are M equations corresponding to M unknowns b_m, eliminating the coefficient of p' and improving the truncation error from $o(h^2)$ to $o(h^{2M})$. After applying b_m, p' is given by

$$p' = \sum_{m=1}^{M} b_m \frac{p_m - p_{-m}}{2h} + o(h^{2M}). \tag{3.7}$$

For the mixed derivative $\partial^2 p[i,j]/\partial x_1 \partial x_2$, we first derive the approximation of $\partial p[i,j]/\partial x_2$:

$$\frac{\partial p[i,j]}{\partial x_2} \approx \sum_{m=1}^{M} b_m \frac{p[i,j+m] - p[i,j-m]}{2h}, \tag{3.8}$$

which can be used in first-order derivative approximation in CG-FD. Then take the derivative in another direction. The mixed derivative approximation is

$$\frac{\partial^2 p[i,j]}{\partial x_1 \partial x_2} \approx \sum_{m=1}^{M} b_m \sum_{n=1}^{M} b_n \frac{p[i+m,j+n] + p[i-m,j-n] - p[i+m,j-n] - p[i-m,j+n]}{4h^2}. \tag{3.9}$$

Note that for the second-order accuracy, the operator of eq. 3.9 spans a 3×3 footprint; for the fourth-order accuracy, it spans a 5×5 footprint, and so on.

3.1.3 First-order derivative operator (for SG)

Similarly to section 3.1.1, in the x_i direction, perform the Taylor series expansion around $p_{j+1/2}$ and take $p_{j+m} - p_{j-m}$:

$$(2m-1)p'_{j+\frac{1}{2}} = \frac{1}{h}(p_{j+m} - p_{j-m}) + o(h^{2k-1}). \tag{3.10}$$

Apply the FD coefficient β_m, which improves the error term to $o(h^{2M})$. β_m satisfies

$$\sum_{m=1}^{M} (2m-1)\beta_m = 1, \quad \sum_{m=1}^{M} (2m-1)^{2k-1}\beta_m = 0, \quad k = 2, ..., M. \tag{3.11}$$

Note that β_m is a purely numerical weighting coefficient, which is distinguished from the S-wave velocity β. Eq. 3.10 represents the first-order derivative approximation of $p_{j+0.5}$. From eq. 3.10, we can obtain the approximation of p'_j:

$$\frac{\partial p_j}{\partial x_i} \approx \sum_{m=1}^{M} \beta_m \frac{p(x_{j-0.5+m}) - p(x_{j+0.5-m})}{h}. \tag{3.12}$$

3.1.4 Difference operator notations

To simplify the expressions of the FD schemes in the following sections and enhance readability, we introduce a set of compact difference operator notations based on the approximations derived above.

Operators for the collocated grid (CG)

We define the first-order central difference operators D_{x_1} and D_{x_2} based on eq. 3.8 as:

$$D_{x_1}[u]_{i,j} = \sum_{m=1}^{M} b_m \frac{u_{i+m,j} - u_{i-m,j}}{2h}, \tag{3.13}$$

$$D_{x_2}[u]_{i,j} = \sum_{m=1}^{M} b_m \frac{u_{i,j+m} - u_{i,j-m}}{2h}. \tag{3.14}$$

Then the second-order mixed derivative (eq. 3.9) can be simply expressed as the nested application of the first-order operators:

$$D_{x_1 x_2}[u]_{i,j} = D_{x_1}[D_{x_2}[u]]_{i,j}. \tag{3.15}$$

The second-order normal difference operators $D_{x_1 x_1}$ and $D_{x_2 x_2}$ based on eq. 3.4 are denoted as:

$$D_{x_1 x_1}[u]_{i,j} = \sum_{m=1}^{M} a_m \frac{u_{i+m,j} - 2u_{i,j} + u_{i-m,j}}{h^2}, \tag{3.16}$$

$$D_{x_2 x_2}[u]_{i,j} = \sum_{m=1}^{M} a_m \frac{u_{i,j+m} - 2u_{i,j} + u_{i,j-m}}{h^2}. \tag{3.17}$$

Operators for the staggered grid (SG)

We define the staggered difference operators based on eq. 3.12 as:

$$\tilde{D}_{x_1}[p]_{i,j} = \sum_{m=1}^{M} \beta_m \frac{p_{i+m-0.5,j} - p_{i-m+0.5,j}}{h}, \tag{3.18}$$

3.2 Numerical implementation for CG-FD

For the 2D CG-FD method, discretize $p(x_1, x_2, t)$ into $p(ih, jh, n\Delta t)$. A collocated grid is created. Fig. 3.1 shows a collocated grid, where all the parameters are in the same grid points.

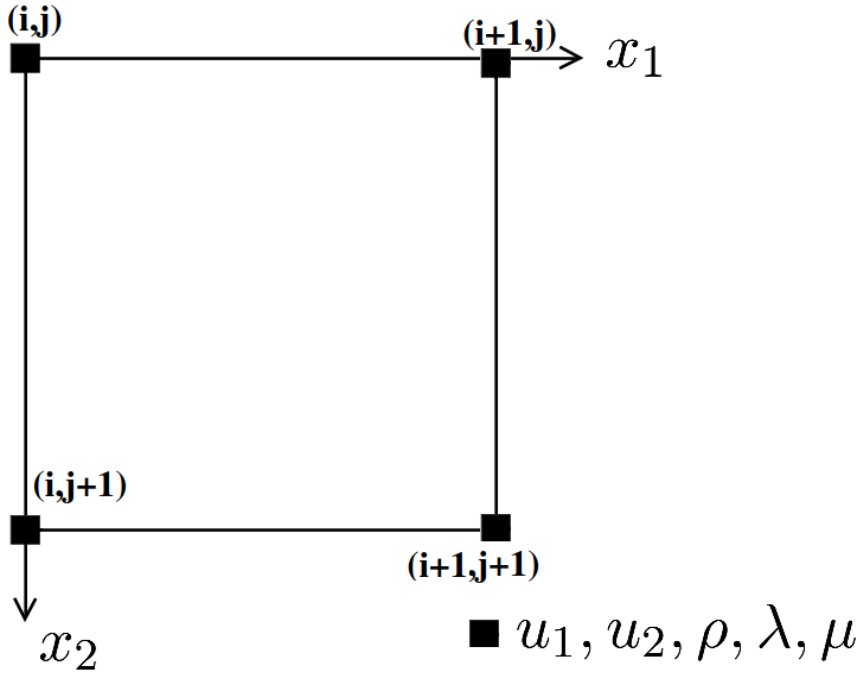

Figure 3.1: *The 2D collocated grid. The parameters are all assigned to the only type of full-grid points.*

3.2.1 Elastic wave equation implementation

In the second-order elastic wave equation, there are second-order normal and mixed derivatives. For homogeneous media, Kelly et al. (1976, eq. 2) gives the second-order accuracy of FD scheme formulas. For arbitrary orders of accuracy, we substitute eq. 3.4 and 3.9 into eq. 2.9, the update formulas are:

$$\begin{aligned}
(u_1)_{i,j}^{n+1} &= 2(u_1)_{i,j}^{n} - (u_1)_{i,j}^{n-1} + \Delta t^2 \Big[\alpha^2 D_{x_1x_1}[u_1] + \beta^2 D_{x_2x_2}[u_1] + (\alpha^2 - \beta^2) D_{x_1x_2}[u_2]\Big]_{i,j}^{n}, \\
(u_2)_{i,j}^{n+1} &= 2(u_2)_{i,j}^{n} - (u_2)_{i,j}^{n-1} + \Delta t^2 \Big[\alpha^2 D_{x_2x_2}[u_2] + \beta^2 D_{x_1x_1}[u_2] + (\alpha^2 - \beta^2) D_{x_1x_2}[u_1]\Big]_{i,j}^{n},
\end{aligned} \tag{3.19}$$

where $\alpha = \sqrt{(\lambda + 2\mu)/\rho}$ is the P-wave velocity, and $\beta = \sqrt{\mu/\rho}$ is the S-wave velocity. Note that the Courant number $r = \alpha\Delta t/h$.

For heterogeneous media, according to eq. A.1, the wave equation includes extra terms compared to eq. 2.9, which are spatially varying Lamé parameters. Therefore, the update

formula is:

$$
\begin{aligned}
(u_1)_{i,j}^{n+1} &= 2(u_1)_{i,j}^{n} - (u_1)_{i,j}^{n-1} + \Delta t^2 \Big[\alpha^2 D_{x_1x_1}[u_1] + \beta^2 D_{x_2x_2}[u_1] + (\alpha^2 - \beta^2) D_{x_1x_2}[u_2]\Big]_{i,j}^{n} \\
&\quad + \frac{\Delta t^2}{\rho_{i,j}} \Big[\lambda_1 (D_{x_1}[u_1] + D_{x_2}[u_2]) + \mu_2 (D_{x_2}[u_1] + D_{x_1}[u_2]) + 2\mu_1 D_{x_1}[u_1]\Big]_{i,j}^{n}, \\
(u_2)_{i,j}^{n+1} &= 2(u_2)_{i,j}^{n} - (u_2)_{i,j}^{n-1} + \Delta t^2 \Big[\alpha^2 D_{x_2x_2}[u_2] + \beta^2 D_{x_1x_1}[u_2] + (\alpha^2 - \beta^2) D_{x_1x_2}[u_1]\Big]_{i,j}^{n} \\
&\quad + \frac{\Delta t^2}{\rho_{i,j}} \Big[\lambda_2 (D_{x_1}[u_1] + D_{x_2}[u_2]) + \mu_1 (D_{x_2}[u_1] + D_{x_1}[u_2]) + 2\mu_2 D_{x_2}[u_2]\Big]_{i,j}^{n},
\end{aligned}
\tag{3.20}
$$

where λ_1, μ_1 and λ_2, μ_2 represent the spatial derivatives in x_1, x_2, respectively.

3.2.2 Acoustic wave equation implementation

In the second-order acoustic wave equation, there are second-order normal derivatives and first-order derivatives. If we substitute eq. 3.4 into eq. 2.11 and eq. 2.8, we can obtain the FD update formula in the acoustic case for homogeneous media as follows:

$$
p_{i,j}^{n+1} = 2\,p_{i,j}^{n} - p_{i,j}^{n-1} + \Delta t^2 \alpha^2 \Big[D_{x_1x_1}[p] + D_{x_2x_2}[p]\Big]_{i,j}^{n}, \tag{3.21}
$$

and for heterogeneous media, as follows:

$$
p_{i,j}^{n+1} = 2\,p_{i,j}^{n} - p_{i,j}^{n-1} + \Delta t^2 \alpha_{i,j}^2 \Big[D_{x_1x_1}[p] + D_{x_2x_2}[p]\Big]_{i,j}^{n} + \lambda_{i,j} \Delta t^2 \Big[w_1 D_{x_1}[p] + w_2 D_{x_2}[p]\Big]_{i,j}^{n}, \tag{3.22}
$$

with $w_{i,j} = 1/\rho_{i,j}$. w_1, w_2 are the spatial derivatives in x_1, x_2, respectively.

3.3 Numerical implementation for SG-FD

For a consistent comparison, the SG-FD parameters are discretized using identical intervals, ensuring that each respective variable occupies an equivalent grid dimension to that of the CG-FD scheme. The spatial arrangement of these variables in a standard staggered grid is shown in fig. 3.2 (Virieux, 1986, fig. 1). Unlike the CG configuration, the SG scheme distributes variables across one full grid node and three supplementary half-grid nodes, each situated at a different relative coordinate to the full node.

The derivatives in the first-order wave equation are all first-order derivatives. Therefore, if we substitute eq. 3.12 into eq. 2.5, the FD scheme can be obtained as follows:

$$
\begin{aligned}
(\sigma_{11})_{i,j}^{n^+} &= (\sigma_{11})_{i,j}^{n^-} + \Delta t \Big[(\lambda + 2\mu) \tilde{D}_{x_1}[v_1] + \lambda \tilde{D}_{x_2}[v_2]\Big]_{i,j}^{n}, \\
(\sigma_{22})_{i,j}^{n^+} &= (\sigma_{22})_{i,j}^{n^-} + \Delta t \Big[(\lambda + 2\mu) \tilde{D}_{x_2}[v_2] + \lambda \tilde{D}_{x_1}[v_1]\Big]_{i,j}^{n}, \\
(\sigma_{12})_{i^+,j^+}^{n^+} &= (\sigma_{12})_{i^+,j^+}^{n^-} + \Delta t \Big[\mu (\tilde{D}_{x_2}[v_1] + \tilde{D}_{x_1}[v_2])\Big]_{i^+,j^+}^{n}, \\
(v_1)_{i^+,j}^{n} &= (v_1)_{i^+,j}^{n-1} + \Delta t \Big[\frac{1}{\rho_1} (\tilde{D}_{x_1}[\sigma_{11}] + \tilde{D}_{x_2}[\sigma_{12}])\Big]_{i^+,j}^{n^-}, \\
(v_2)_{i,j^+}^{n} &= (v_2)_{i,j^+}^{n-1} + \Delta t \Big[\frac{1}{\rho_2} (\tilde{D}_{x_1}[\sigma_{12}] + \tilde{D}_{x_2}[\sigma_{22}])\Big]_{i,j^+}^{n^-}.
\end{aligned}
\tag{3.23}
$$

where $\sigma_{12}^{n+}[i^+, j^+]$ represents the value at the staggered grid point $(ih + h/2, jh + h/2, n\Delta t + \Delta t/2)$. $\alpha = \sqrt{(\lambda + 2\mu)/\rho}$ is P-wave velocity, and $\beta = \sqrt{\mu/\rho}$ is SV-wave velocity. For the acoustic wave, set $\mu = 0$, $\sigma_{12} = 0$ and $\sigma_{11} = \sigma_{22} = -p$.

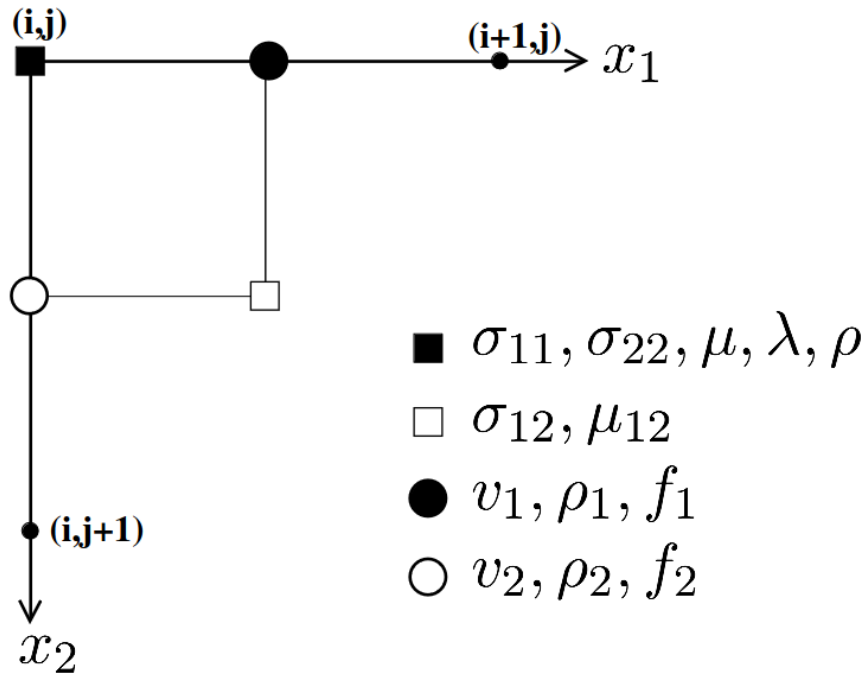

Figure 3.2: *The 2D standard staggered grid (SSG)(Virieux, 1986, fig. 1). Parameters are assigned to four types of grid points: one full-grid position and three spatially distinct half-grid positions.*

3.3.1 Numerical implementation of source terms

In addition to the time delay $1/f_c$ mentioned in section 2.5.2, which ensures the Ricker wavelet has a physically smooth onset starting from $t = 0$, an extra time shift is applied in FD implementation. In the FD numerical implementation, the discrete-time series is counted starting from $t = \Delta t$. To ensure the source can be numerically aligned with the discrete temporal grid, an extra time shift Δt should be applied to the Ricker wavelet generally.

Specifically, in the staggered grid (SG-FD) implementation, for the pressure source, the pressure field is physically and logically updated half a time step (e.g., 1.5 Δt shift) relative to the velocity field (Δt shift). In the programming implementation, the time index of the pressure field is typically delayed and mapped to an integer time step. Therefore, in order to match the indexing logic of the program and ensure the physical alignment of the wavefield on the time axis, we applied a total time shift of $2\Delta t$ to the pressure source.

3.4 Green's function

A Green's-function solution is required as an analytical benchmark for comparison with the FD result. The time Fourier transform of the wavefield is given by (Carcione et al., 1988, eq. B3a to B4b):

$$\begin{aligned} \tilde{u}_1(d,\omega,v_p,v_s) &= \frac{F}{2\pi\rho}\cdot\frac{x_1x_2}{d^2}\left[\tilde{G}_1(d,\omega,v_p,v_s)+\tilde{G}_2(d,\omega,v_p,v_s)\right], \\ \tilde{u}_2(d,\omega,v_p,v_s) &= \frac{F}{2\pi\rho}\cdot\frac{1}{d^2}\left[x_2^2\tilde{G}_1(d,\omega,v_p,v_s)-x_1^2\tilde{G}_2(d,\omega,v_p,v_s)\right], \end{aligned} \tag{3.24}$$

where

$$\begin{aligned}\tilde{G}_1(d,\omega,v_p,v_s) &= -i\frac{\pi}{2}\left[\frac{1}{v_p^2}H_0^{(2)}\left(\frac{\omega}{v_p}\right)+\frac{1}{\omega d v_s}H_1^{(2)}\left(\frac{\omega}{dv_s}\right)-\frac{1}{\omega d v_p}H_1^{(2)}\left(\frac{\omega}{dv_p}\right)\right],\\ \tilde{G}_2(d,\omega,v_p,v_s) &= i\frac{\pi}{2}\left[\frac{1}{v_s^2}H_0^{(2)}\left(\frac{\omega}{dv_s}\right)-\frac{1}{\omega d v_s}H_1^{(2)}\left(\frac{\omega}{dv_s}\right)+\frac{1}{\omega d v_p}H_1^{(2)}\left(\frac{\omega}{dv_p}\right)\right].\end{aligned} \tag{3.25}$$

In eq. 3.24, F is a constant that gives the magnitude of the force. The force is impulsive and acts in the positive x_2 direction. d represents the radial distance between the source point and the receiver point. ω is the angular frequency. v_p and v_s are the velocities of the P-wave and S-wave, respectively. In eq. 3.25, $\tilde{G}_1$ and $\tilde{G}_2$ are the time Fourier transforms of the Green's function solutions $G_1(d,t)$ and $G_2(d,t)$, respectively. $H_0^{(2)}$ and $H_1^{(2)}$ represent the zero- and first-order Hankel functions of the second kind, respectively.

$\tilde{G}_1$ and $\tilde{G}_2$ in eq. 3.25 are used for the analytical solution of the elastic case. In the acoustic case, the 2D analytical solution is given as (Morse and Feshbach, 1946, eq. 7.2.18)

$$\tilde{G}^{\mathrm{2D}} = \sqrt{\frac{2\pi v_p}{\omega d}}e^{-ikd}e^{-i\pi/4}, \tag{3.26}$$

which is the solution for the far-field approximation.

Chapter 4

Stability & Dispersion Analysis

This chapter primarily analyzes the stability limits and numerical dispersion relations of CG-FD and SG-FD. To obtain these relations, we employ a standard analytical approach: We assume a simple plane wave propagating in the medium and substitute it into the respective FD update schemes.

For SG-FD, the derivation of the dispersion relations mainly references existing literature (Liu and Sen, 2011). The detailed derivation process and corresponding stability analysis are provided in appendix C.

For CG-FD, we use a similar analysis method as SG-FD. Its complete mathematical derivation can also be found in appendix B. CG-FD uses different wave equations, which correspond to different stability limits and dispersion relations.

For brevity, the following sections of this chapter directly present and discuss the final formulas of these two methods. The comparative results are shown in chapter 5.

4.1 Stability and dispersion analysis of CG-FD

4.1.1 Stability and dispersion relation of FD method on elastic wave equation (homogeneous media)

The derivation is detailed in appendix B.1. We define the normal spatial components S_{11} and S_{22}, and along with the mixed spatial coupling component S_{12}, as follows:

$$\begin{aligned} S_{12} &= \sum_{m=1}^{M} b_m \sum_{l=1}^{M} b_l \frac{\sin(mk_1h)\sin(lk_2h)}{4}, \\ S_{11} &= \sum_{m=1}^{M} a_m \sin^2 \frac{mk_1h}{2}, \\ S_{22} &= \sum_{m=1}^{M} a_m \sin^2 \frac{mk_2h}{2}, \end{aligned} \tag{4.1}$$

where $k_1 = k\sin\theta$ and $k_2 = k\cos\theta$ are the wavenumber components in the x_1 and x_2 directions, respectively. To ensure the stability of the numerical simulation, the Courant number $r_p = \alpha\Delta t/h$ must strictly satisfy the theoretical stability threshold $r_{\max}$. By substituting the decoupled spatial terms into the analytical solution from appendix B.1, the stability limit for the 2D elastic CG-FD scheme is given by:

$$r_p \leq r_{\max} = \sqrt{\frac{2}{(1+\gamma^2)(S_{11}+S_{22}) + (1-\gamma^2)\sqrt{(S_{11}-S_{22})^2 + 4S_{12}^2}}}, \tag{4.2}$$

where $\gamma = \beta/\alpha$ is the S-wave to P-wave velocity ratio. For the second-order accuracy, i.e., $2M = 2$, eq. 4.2 reduces to (Marfurt, 1984)

$$r_{\max} = \frac{1}{\sqrt{1+\gamma^2}}. \tag{4.3}$$

For the higher-order accuracy, the verification is mentioned in section 5.2.2.

Furthermore, the numerical dispersion relation is characterized by the phase velocity ratio c_{fd}/c, where c_{fd} is the numerical phase velocity and c is the true physical phase velocity. The expression is divided into P-wave and S-wave dispersion relation:

$$\frac{c_{\text{fd}}}{c} = \frac{\omega\Delta t}{khr_p} = \frac{2}{khr_p}\arcsin\left(r_p\sqrt{\frac{1+\gamma^2}{2}\left(S_{11}+S_{22}\right)+\frac{1-\gamma^2}{2}\sqrt{\left(S_{11}-S_{22}\right)^2+4S_{12}^2}}\right) \tag{4.4}$$

or

$$\frac{c_{\text{fd}}}{c} = \frac{\omega\Delta t}{khr_s} = \frac{2}{khr_s}\arcsin\left(r_p\sqrt{\frac{1+\gamma^2}{2}\left(S_{11}+S_{22}\right)-\frac{1-\gamma^2}{2}\sqrt{\left(S_{11}-S_{22}\right)^2+4S_{12}^2}}\right). \tag{4.5}$$

Physically, the ratio c_{fd}/c quantifies the phase error introduced by the numerical discretization. An ideal ratio is equal to 1, in which case the simulated FD velocity is equal to the true velocity. Thus, a value closer to 1 indicates weaker numerical dispersion and higher simulation accuracy.

Note that eq. 4.2, 4.4 and 4.5 actually include r_p and r_s, where r_s is represented by r_p and γ. This means that the equations describe the individual effects of P-waves and S-waves, and the effects of their coupling. S_{11}, S_{22} and S_{12} represent spatial variations of the wavefield.

The analysis is based on the case of homogeneous media. For heterogeneous media, we can use the assumption of local homogeneity to estimate the stability condition and dispersion relation. That is, we treat a heterogeneous medium area as a composition of localized homogeneous areas, and the global simulation parameters are then strictly constrained by the most restrictive local conditions. However, if an exact analysis is needed, it is necessary to solve based on the heterogeneous elastic wave equation, because compared with the homogeneous elastic wave equation, some additional terms in the heterogeneous elastic wave equation can affect the results.

4.1.2 Stability and dispersion relation of FD method on acoustic wave equation (homogeneous media)

In the acoustic case, the analysis is based on the acoustic wave equation. We use the same analysis method as in the previous section. The derivation is detailed in appendix B.2. The stability limit is obtained as:

$$r_p \le r_{\max} = \frac{1}{\sqrt{\sum_{m=1}^{M} a_m\left[\sin^2\left(\frac{mkh\sin\theta}{2}\right)+\sin^2\left(\frac{mkh\cos\theta}{2}\right)\right]}}, \tag{4.6}$$

which is different from the generalized form (Lines et al., 1999):

$$r_{\max} = \frac{1}{\sqrt{\sum_{m=1}^{M}|a_m|+\left|\sum_{m=1}^{M}a_m\right|}}. \tag{4.7}$$

For eq. 4.6, we obtain the global minimum using the grid scan method. Its result is almost identical to that of eq. 4.7, but the conditions of eq. 4.6 are slightly more lenient. Eq. 4.7 gives a sufficient condition for stability. To simplify calculations, it amplifies the constraints and makes a conservative estimate, while eq. 4.6 does not perform this step.

Since this is irrelevant to the purpose of this thesis, further analysis is not provided here. More discussion on these topics is in appendix B.2.2. This thesis displays the results based on eq. 4.6, which is more accurate.

The numerical dispersion relation for the 2D CG-FD scheme for the acoustic case is

$$\frac{c_{\mathrm{fd}}}{c} = \frac{\omega \Delta t}{khr_p} = \frac{2}{khr_p} \arcsin\left[r_p \sqrt{\sum_{m=1}^{M} a_m \left[\sin^2\left(\frac{mkh\sin\theta}{2}\right) + \sin^2\left(\frac{mkh\cos\theta}{2}\right)\right]}\right]. \tag{4.8}$$

4.2 Stability and dispersion analysis of SG-FD

Liu and Sen (2011) gives the derivation of the dispersion relation. We also derived the stability constraint in the process. The detailed derivation is provided in appendix C. The stability constraint is obtained as

$$r_p \leq r_{\max} = \frac{1}{\sqrt{\left(\sum_{m=1}^{M} \beta_m \sin((m-0.5)k_1 h)\right)^2 + \left(\sum_{m=1}^{M} \beta_m \sin((m-0.5)k_2 h)\right)^2}}. \tag{4.9}$$

Different from CG-FD, the minimum position of $r_{\max}$ in eq. 4.9 is fixed. The minimum of $r_{\max}$ is always at $kh = \sqrt{2}\pi$, $\theta = n\pi/4$ with $n = 1, 3, 5, 7$. Therefore, eq. 4.9 can be simplified as

$$r_{\max} = \frac{1}{\sqrt{2}\sum_{m=1}^{M} |\beta_m|}, \tag{4.10}$$

which is used for the stability constraints of SG-FD in this thesis. The dispersion relation of SG-FD is given by (Liu and Sen, 2011)

$$\begin{aligned} \frac{c_{\mathrm{fd}}}{c} &= \frac{w\Delta t}{khr_p} \\ &\approx \frac{2}{khr_p} \arcsin \sqrt{r_p^2 \left[\left(\sum_{m=1}^{M} \beta_m \sin((m-0.5)k_1 h)\right)^2 + \left(\sum_{m=1}^{M} \beta_m \sin((m-0.5)k_2 h)\right)^2 \right]}, \end{aligned} \tag{4.11}$$

or

$$\begin{aligned} \frac{c_{\mathrm{fd}}}{c} &= \frac{w\Delta t}{khr_s} \\ &\approx \frac{2}{khr_s} \arcsin \sqrt{r_s^2 \left[\left(\sum_{m=1}^{M} \beta_m \sin((m-0.5)k_1 h)\right)^2 + \left(\sum_{m=1}^{M} \beta_m \sin((m-0.5)k_2 h)\right)^2 \right]}. \end{aligned} \tag{4.12}$$

Eq. 4.11 and 4.12 represent the dispersion relation of P-wave and S-wave, respectively.

Chapter 5

Evaluation of Stability & Dispersion Properties

This chapter numerically displays the stability and dispersion relations obtained in chapter 4. For eq. 4.2 and eq. 4.6, we used the grid scan method to obtain their numerical stability boundary, which needs to be verified using specific models. The verification is based on the checking model, which is adjusted by the homogeneous model displayed in this chapter.

5.1 Homogeneous model

Fig. 5.1 shows the homogeneous reference model used throughout this chapter. The density is $\rho = 2000\,\mathrm{kg/m^3}$. The S-wave to P-wave velocity ratio is $\gamma = 0.4$. In the acoustic case, we simply set $v_s = 0\,\mathrm{m/s}$. The verification models introduced in section 5.2.2 are obtained by slightly modifying this reference model in order to test the proposed stability limits.

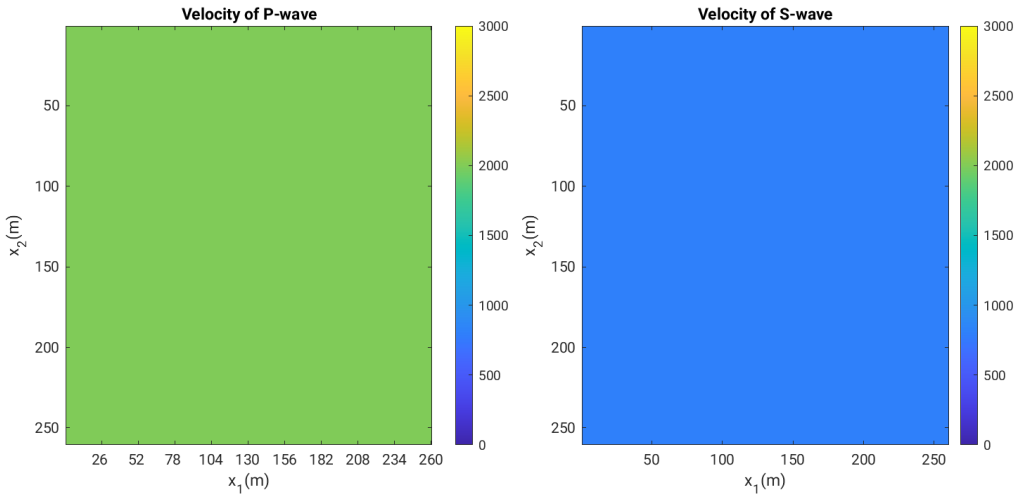

Figure 5.1: *Homogeneous model with* $v_p = 2000\,\mathrm{m/s}$ *(left),* $v_s = 800\,\mathrm{m/s}$ *(right). The grid size is* 260×260.

5.2 Stability verification

5.2.1 Grid scan method

The grid scan method is applied to eq. 4.2 and eq. 4.6. Taking eq. 4.2 as an example, $r_{\max}$ depends on five variables, which are M, θ, k, h, γ. Because k and h always appear together, they can be treated as a single combined variable through kh. For each selected pair of M and γ, we scan the $r_{\max}(\theta, kh)$ surface over the range $kh \in (0, \pi]$ and $\theta \in [0, 2\pi)$, and determine its global minimum. The resulting values can then be used as general stability limits for the corresponding parameter set.

The results obtained above can be used as a general solution. However, in practical simulations, the effective stability threshold may occasionally appear slightly less restrictive, particularly in noise-free cases with a finite source bandwidth. However, this issue is beyond the scope of the present thesis and is therefore not discussed further.

5.2.2 Numerical verification of the proposed stability limit

Eq. 4.2 and eq. 4.6 are the stability limits proposed in this thesis, which are verified in this section.

Elastic CG-FD

For the second-order accuracy, the stability limit is verified in theory (eq. 4.3). For higher spatial orders, the proposed limit can be verified numerically by constructing two models with Courant numbers slightly below and slightly above $r_{\max}$. If the proposed threshold is correct, the first model should remain stable, whereas the second should become unstable.

In this thesis, the homogeneous reference model uses $\gamma = 0.4$. As an example, we therefore verify the case $\gamma = 0.4$ and $2M = 4$,for which $r_{\max} \approx 0.8013$. To keep the verification models close to the reference model, we set $h = 1\,\mathrm{m}$ and $\Delta t = 0.0004\,\mathrm{s}$.

The first verification model uses $v_p = 2003\,\mathrm{m/s}$ and $v_s = \gamma v_p = 801.2\,\mathrm{m/s}$, giving $r_p = v_p \Delta t/h = 0.8012 < r_{\max}$. The corresponding snapshot results are shown in fig. 5.2, and the seismograms are shown in fig. 5.3. The results are plotted without normalization, and the late-time portion of the seismograms is enlarged in order to reveal any minor instability. Both the P-wave and S-wave arrivals are clearly visible. Absorbing boundary conditions are not applied because they are not relevant to the purpose of this test. For the recording length of 0.1 s, boundary reflections do not contaminate the receiver traces. If the case is unstable, as the time step increases, the values expand out of control. No numerical growth is observed, indicating that this simulation is stable.

The second verification model uses $v_p = 2004\,\mathrm{m/s}$ and $v_s = \gamma v_p = 801.6\,\mathrm{m/s}$,giving $r = v_p \Delta t/h = 0.8016 > r_{\max}$. The corresponding snapshots and seismograms are shown in figs. 5.4 and 5.5. Compared with the stable case, high-frequency and high-amplitude artifacts grow rapidly and eventually dominate the wavefield. These artifacts are also visible in the receiver records and begin to contaminate the S-wave portion of the seismograms.

Taken together, these two tests provide one stable and one unstable example that agree with the predicted threshold, thereby supporting the correctness of eq. 4.2.

Acoustic CG-FD

As discussed in section 4.1.2, the grid scan method yields a stability limit that is almost identical to the conservative result obtained from standard von Neumann analysis. Fig. 5.6

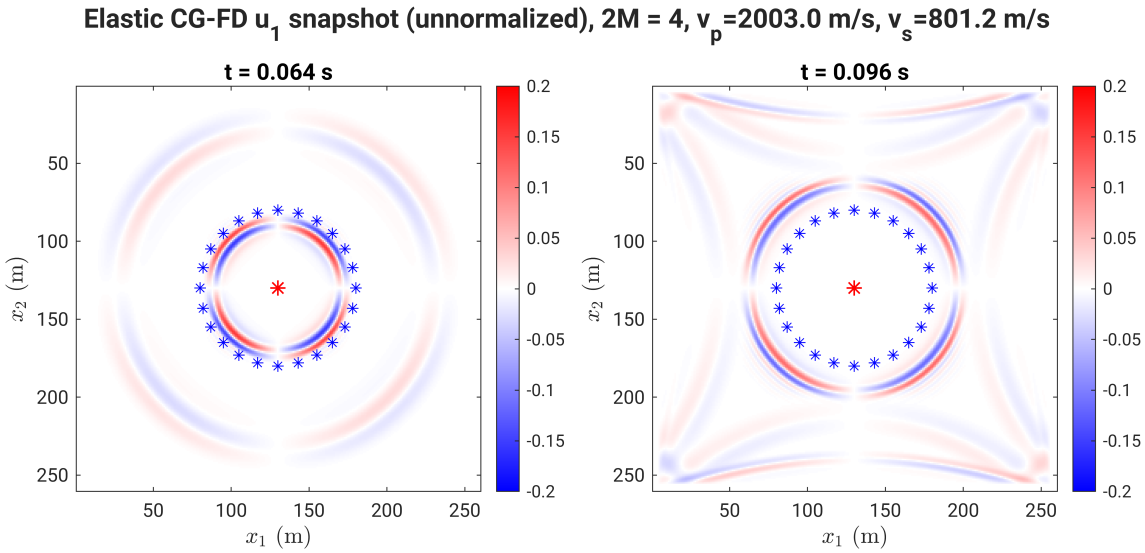

Figure 5.2: *The u_1 snapshot results of elastic CG-FD at $t = 0.064\,\mathrm{s}$ (left) and $t = 0.096\,\mathrm{s}$ (right). $\gamma = 0.4$, $2M = 4$, $v_p = 2003\,\mathrm{m/s}$, $v_s = 801.2\,\mathrm{m/s}$ and $r_p < r_{\max}$. The source is Ricker wave mentioned in section 2.5.2 with the center frequency $f_c = 80\,\mathrm{Hz}$. The blue and red points represent the receiver and source points, respectively. The amplitude is unnormalized.*

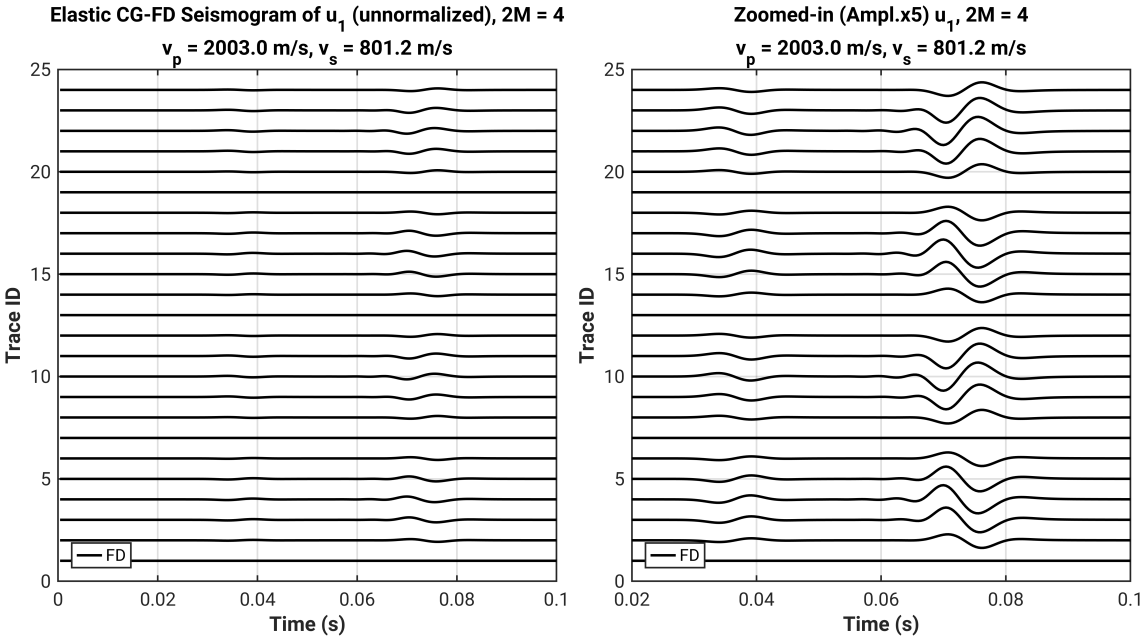

Figure 5.3: *Elastic CG-FD seismogram of u_1 with the full unnormalized waveforms (left) and zoomed-in view of the late-time waveforms with a $10\times$ amplification (right). $\gamma = 0.4$, $2M = 4$, $v_p = 2003\,\mathrm{m/s}$, $v_s = 801.2\,\mathrm{m/s}$ and $r_p < r_{\max}$. The trace IDs correspond to the receiver array shown in fig. 5.2, starting with 1 at the x_2 positive direction (bottom receiver) and increasing in a counterclockwise direction. The vertical spacing between adjacent traces is set such that a true amplitude of 1 exactly spans the distance to the neighboring baseline.*

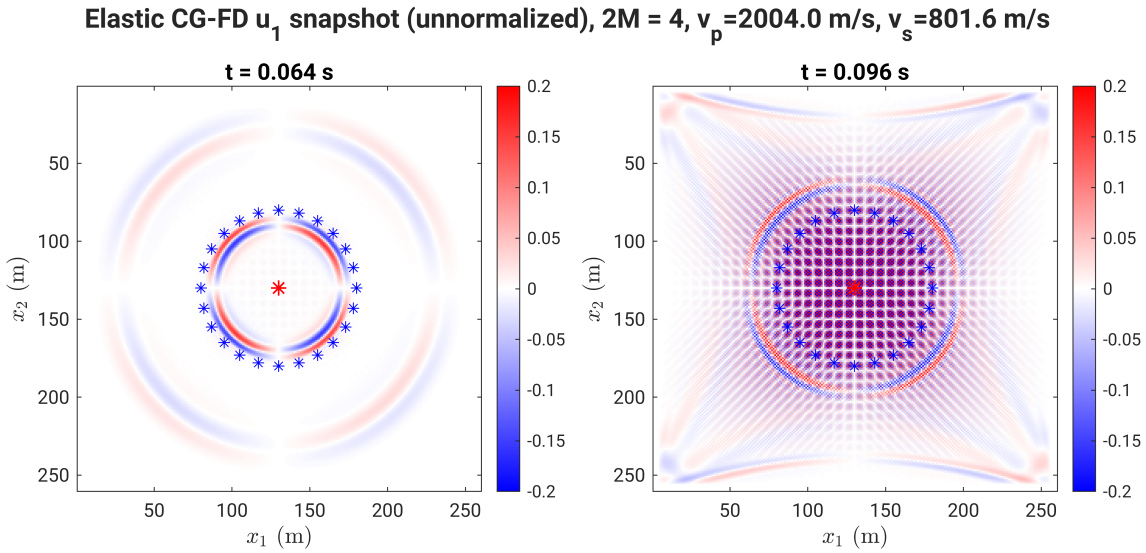

Figure 5.4: *The u_1 snapshot results of elastic CG-FD at $t = 0.064\,\mathrm{s}$ (left) and $t = 0.096\,\mathrm{s}$ (right). $v_p = 2004\,\mathrm{m/s}$, $v_s = 801.6\,\mathrm{m/s}$ and $r_p > r_{\max}$. Other configurations are same as in fig. 5.2.*

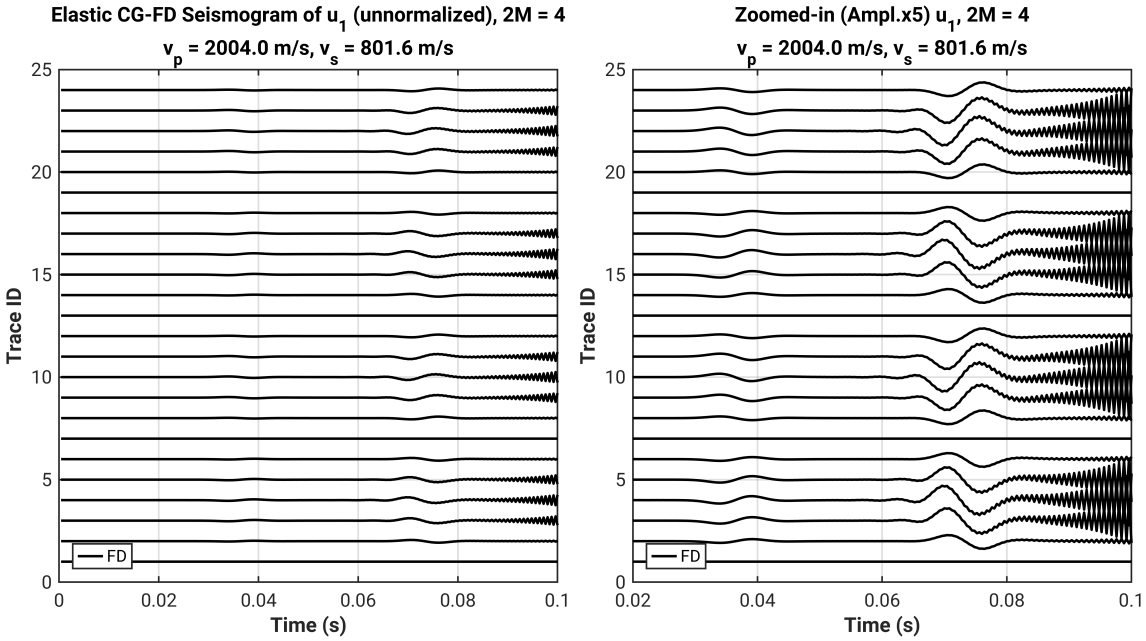

Figure 5.5: *Elastic CG-FD seismogram of u_1 with the full unnormalized waveforms (left) and zoomed-in view of the late-time waveforms with a $5\times$ amplification (right). The velocity model is consistent with fig. 5.4, and the trace configuration is the same as in fig. 5.3.*

shows that the two estimates differ only slightly. To verify the grid-scan result numerically, we construct a model whose Courant number lies between the two limits.

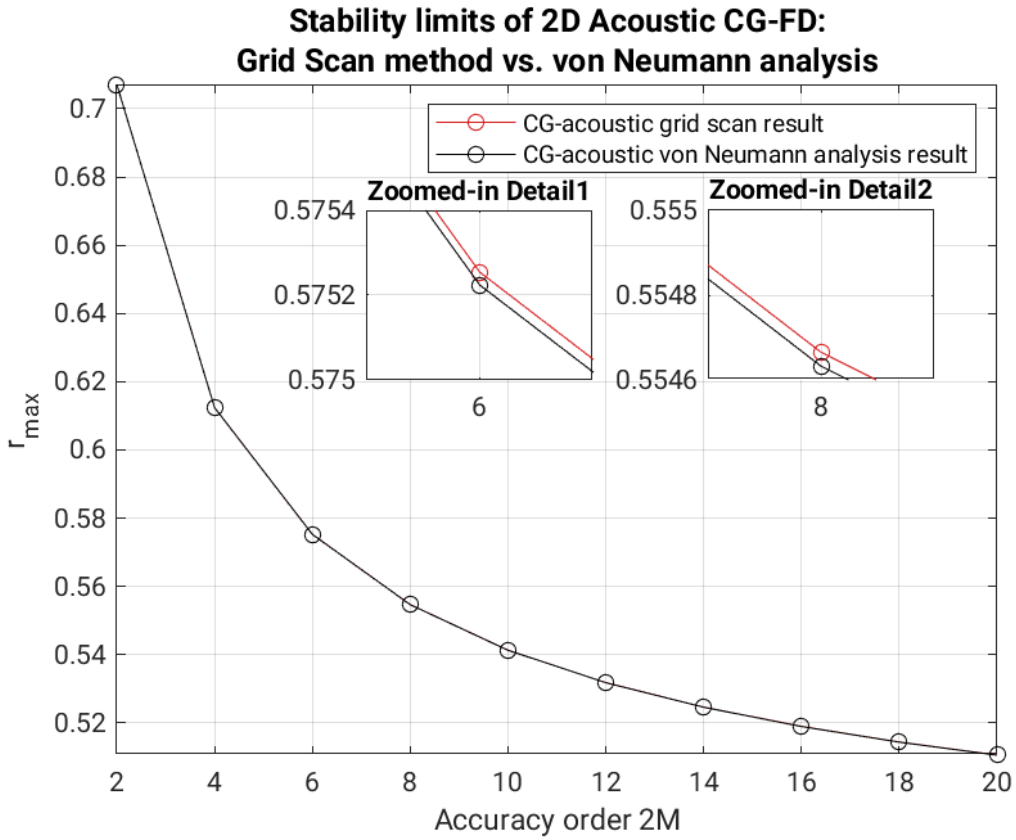

Figure 5.6: *Acoustic CG-FD stability limits from grid scan method (red) and von Neumann analysis (black). The results are presented as points because the orders of accuracy are all evens. A line graph is used to illustrate the corresponding trends.*

The verification model is homogeneous with $v_p = 2876.2\,\mathrm{m/s}$. We choose $h = 1\,\mathrm{m}$ and $\Delta t = 0.0002\,\mathrm{s}$, and then perform the acoustic CG-FD simulation. The resulting snapshots and seismograms are shown in figs. 5.7 and 5.8. The P-wave waveform is clearly visible and no instability-related artifacts are observed. This indicates that the simulation remains stable and supports the use of the grid scan method as a practical way to determine the less conservative global stability bound.

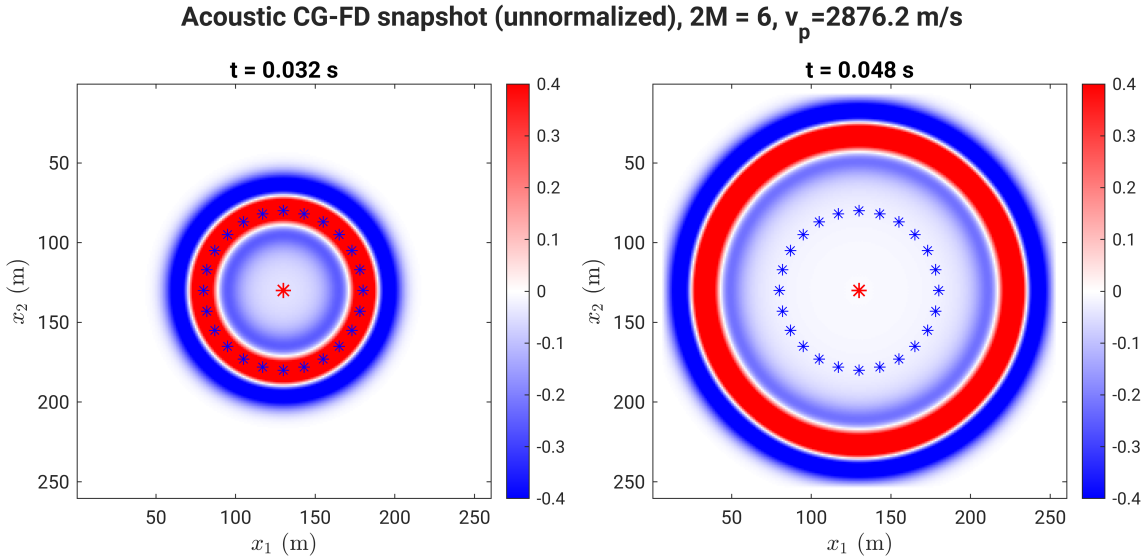

Figure 5.7: *The snapshot of acoustic CG-FD at* $t = 0.032\,\mathrm{s}$ *(left) and* $t = 0.048\,\mathrm{s}$ *(right).* $2M = 6$ *and* $v_p = 2876.2\,\mathrm{m/s}$. $r_p = 0.57524$ *lies between the* $r_{\max}$ *of grid scan method and von Neumann analysis. The positions of source and receivers are same as in fig. 5.2.*

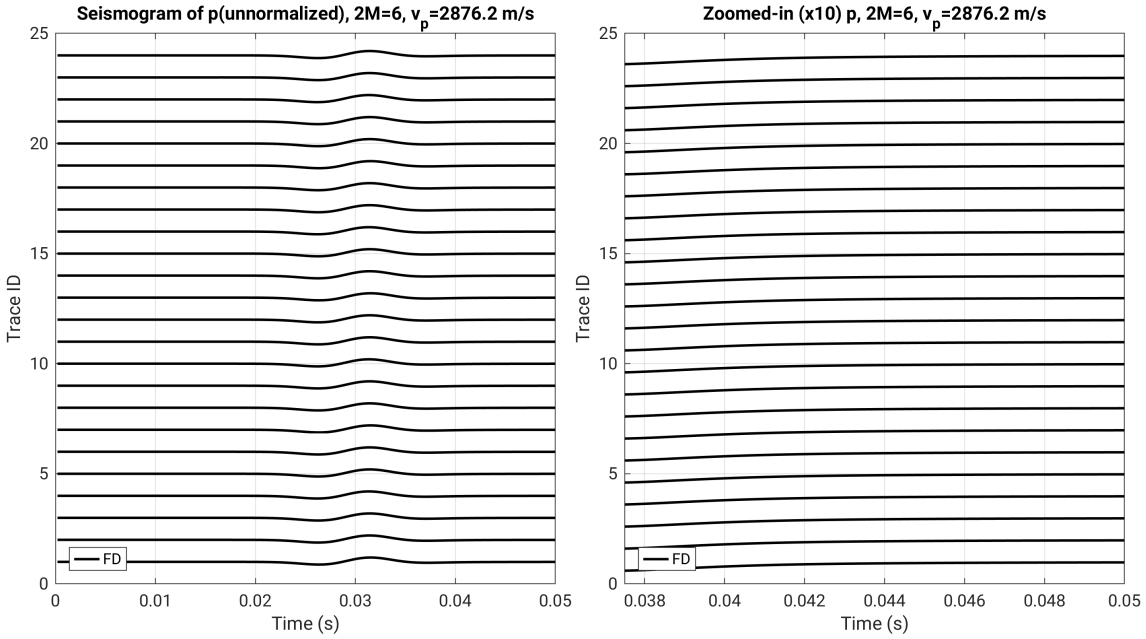

Figure 5.8: *Acoustic CG-FD seismogram of p with the full unnormalized waveforms (left) and zoomed-in view of the late-time waveforms with a* $10\times$ *amplification (right). The velocity model is consistent with fig. 5.7, and the trace configuration is the same as in fig. 5.3.*

5.3 Numerical stability boundaries

For CG-FD, the grid scan method is applied to eqs. 4.2 and 4.6 to obtain the stability limits for the elastic case and the acoustic case. For SG-FD, the stability limit is obtained from eq. 4.10, which applies to both cases. The results are summarized in fig. 5.9.

The figure shows that higher spatial accuracy generally requires a more restrictive stability limit. In elastic CG-FD, the limit also depends on γ, the S-wave to P-wave velocity ratio. Specifically, a larger γ leads to a smaller stability limit and a faster decrease of that limit with increasing γ. The acoustic CG-FD stability limit is lower than the elastic CG-FD limits shown here and is close to the SG-FD result. Overall, the figure indicates that CG-FD in homogeneous isotropic media has a less restrictive stability condition than SG-FD in the elastic case, whereas in the acoustic case the two methods are much closer.

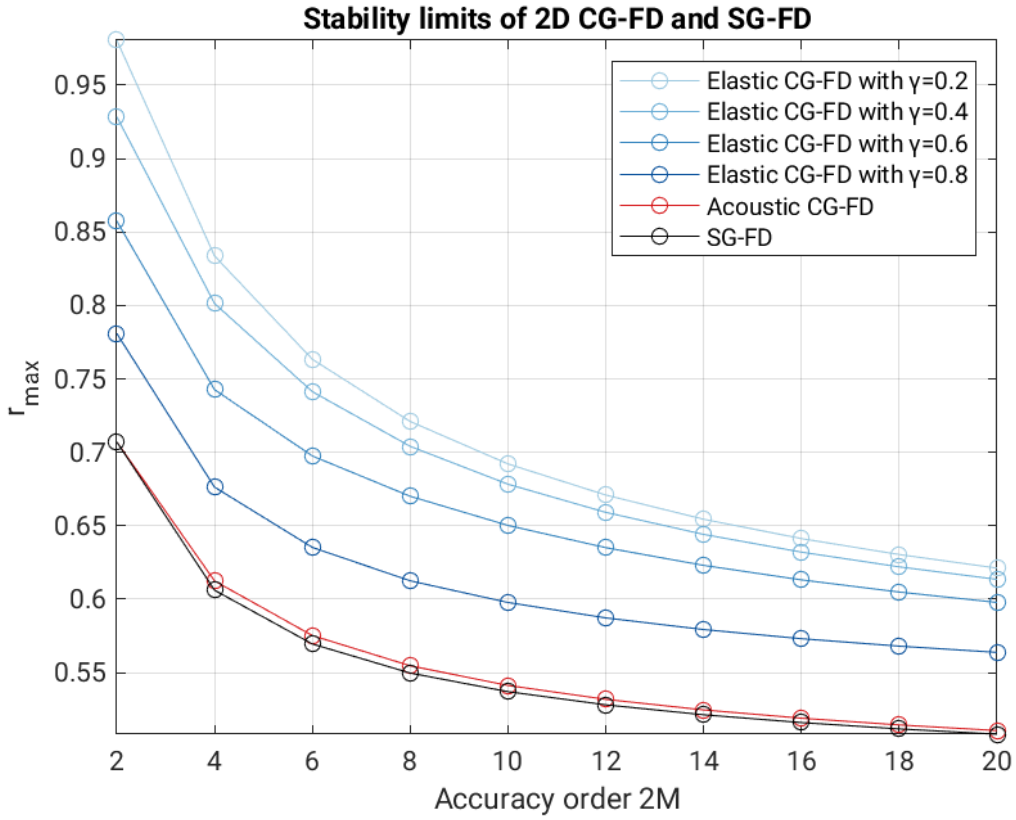

Figure 5.9: *The stability limits of CG-FD and SG-FD in both elastic case and acoustic case. The plot configuration is the same as in fig. 5.6. The results of SG-FD work both elastic and acoustic cases. Unlike SG-FD, CG-FD uses different equations, separating results in elastic and acoustic cases.*

5.4 Numerical dispersion relation

As mentioned in section 4.1.1, the evaluation of the numerical dispersion relation depends on how closely the wave velocity simulated by FD approximates the actual wave velocity; i.e., $c_{\mathrm{fd}}/c = 1$ is the ideal situation. Therefore, this section displays and evaluates the $c_{\mathrm{fd}}/c - kh$ curves.

5.4.1 P-wave numerical dispersion relation

Based on the theoretical formulations in eqs. 4.4 (elastic CG-FD), 4.8 (acoustic CG-FD), and 4.11 (SG-FD), we compute the P-wave dispersion curves for different propagation directions. Only two representative cases are shown here: propagation along the positive x_2 axis and propagation along the diagonal direction. Other directions lie between these two limiting cases and follow the same symmetry. The results are presented in figs. 5.10 and 5.11.

In both figures, c_{fd}/c remains close to unity at small kh, indicating weak numerical dispersion for low frequencies. As kh increases, the deviation between the simulated phase velocity and the actual physical velocity becomes increasingly larger. This means that the wavefield, which should propagate at a constant velocity in a homogeneous medium, is affected by the grid discretization in the FD simulation. Specifically, low-frequency and high-frequency components propagate at different and incorrect velocities. Nevertheless, as the order of spatial accuracy increases, the c_{fd}/c curves are closer to 1 at high kh, which means higher-order FD schemes effectively suppress numerical dispersion errors.

Fig. 5.10 shows the numerical dispersion curves of the P-wave propagating along the positive x_2-axis. In this direction, the CG-FD and SG-FD curves are identical or nearly identical for both the acoustic and elastic cases. Moreover, in the elastic CG-FD P-wave dispersion is essentially independent of γ in this propagation direction.

Fig. 5.11 shows the numerical dispersion curves of the P-wave propagating along the diagonal direction. We compare fig. 5.11 with 5.10. In the acoustic case, the P-wave dispersion of CG-FD remains very close to that of SG-FD. In the elastic case, however, the P-wave dispersion of CG-FD is worse than that of SG-FD, which is different from fig. 5.10. For elastic CG-FD, the P-wave dispersion is affected by γ, which is also different. Specifically, the smaller the γ, the worse the P-wave dispersion. Note that in fig. 5.11, not all dispersion curves show improvement compared with fig. 5.10. Specifically, some dispersion curves of elastic CG-FD with low γ are worse.

5.4.2 S-wave numerical dispersion relation

The S-wave dispersion curves for axial propagation are shown in fig. 5.12. Along the positive x_2 direction, the S-wave dispersion curves are very similar to the corresponding P-wave curves in fig. 5.10.

The S-wave dispersion curves for diagonal propagation are shown in fig. 5.13. Note that the vertical scale of c_{fd}/c in fig. 5.13 differs from that in fig. 5.11. In SG-FD, the P-wave and S-wave dispersion behaviors remain broadly similar. In elastic CG-FD, by contrast, the S-wave dispersion depends more strongly on γ than that of the P-wave. For relatively large γ, the S-wave phase velocity remains closer to the physical value. For a certain smaller γ, the deviation occurs on the opposite side of unity ($c_{\mathrm{fd}} > c$). As γ decreases further, the S-wave dispersion becomes increasingly severe. Although higher spatial order improves the results, the S-wave generally requires a higher order than the P-wave to achieve similarly small dispersion.

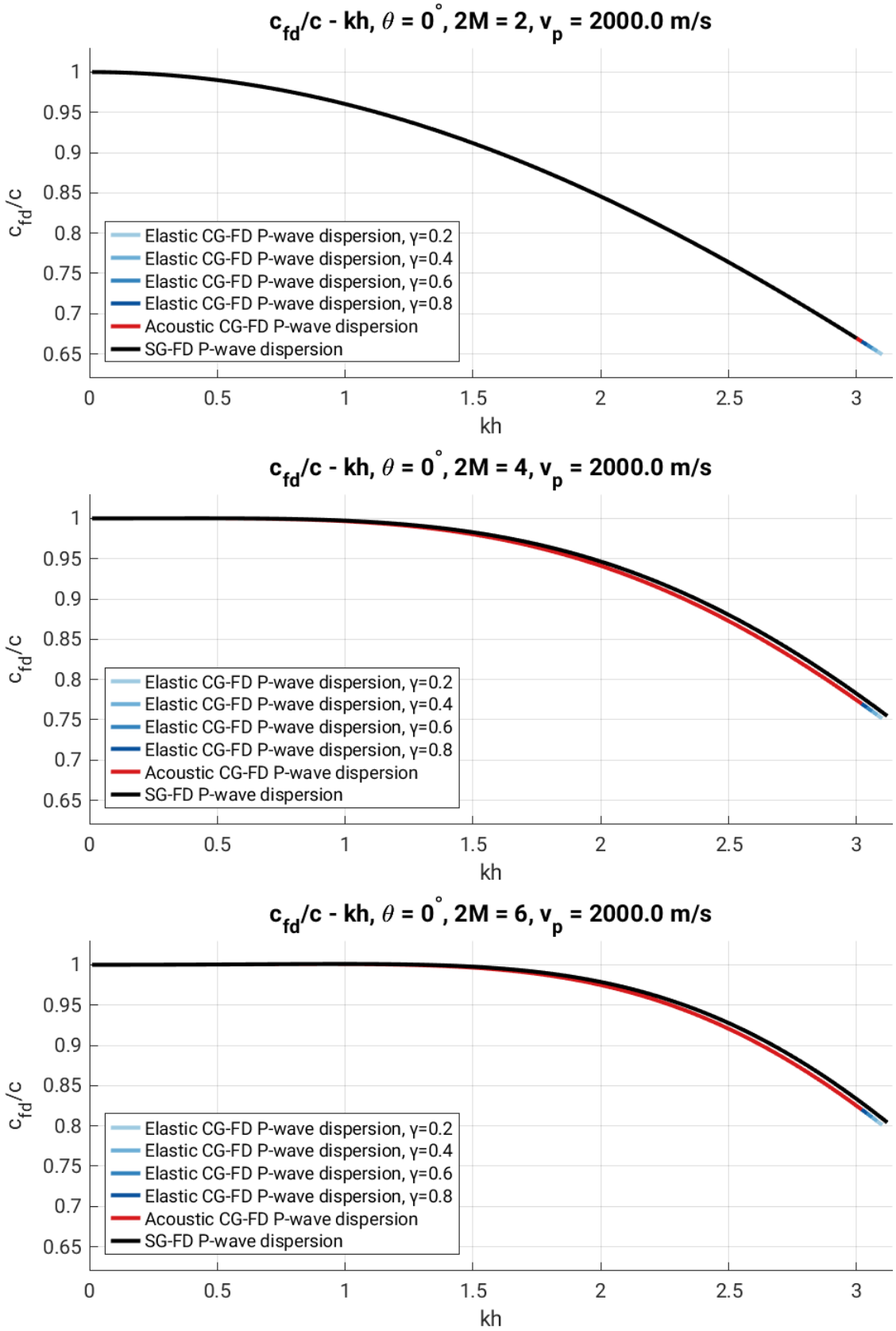

Figure 5.10: *The P-wave dispersion relation c_{fd}/c of collocated grid FD and staggered grid FD. $v_p = 2000\,\mathrm{m/s}$ corresponds to the homogeneous model of fig. 5.1. Propagation is along the positive direction of x_2-axis. Unlike SG-FD, CG-FD uses different equations, separating results in elastic and acoustic cases.*

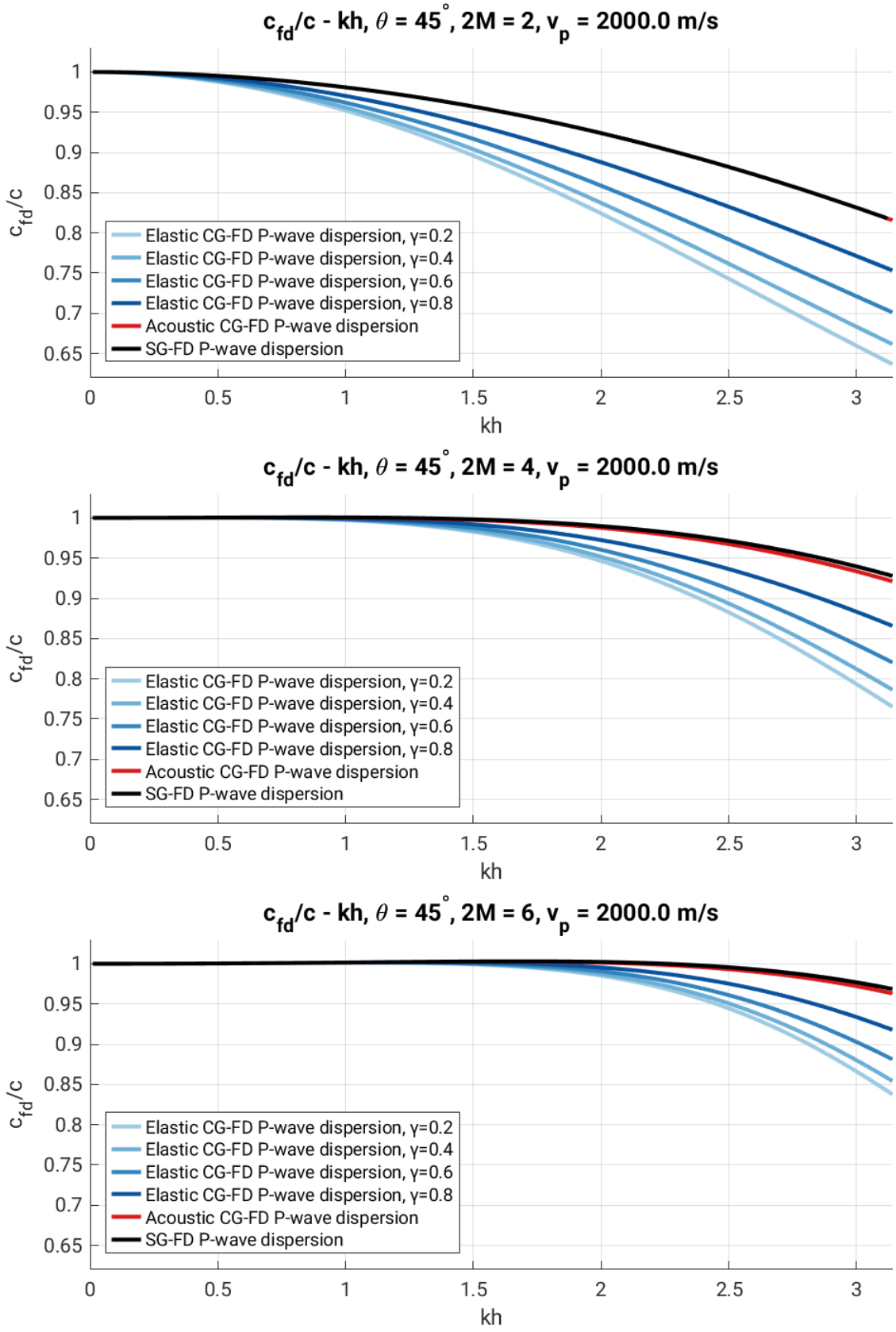

Figure 5.11: *The P-wave dispersion relation c_{fd}/c of CG-FD and SG-FD. The P-wave velocity and plot configuration for this figure are the same as that for fig. 5.10. Wave propagates along the diagonal direction.*

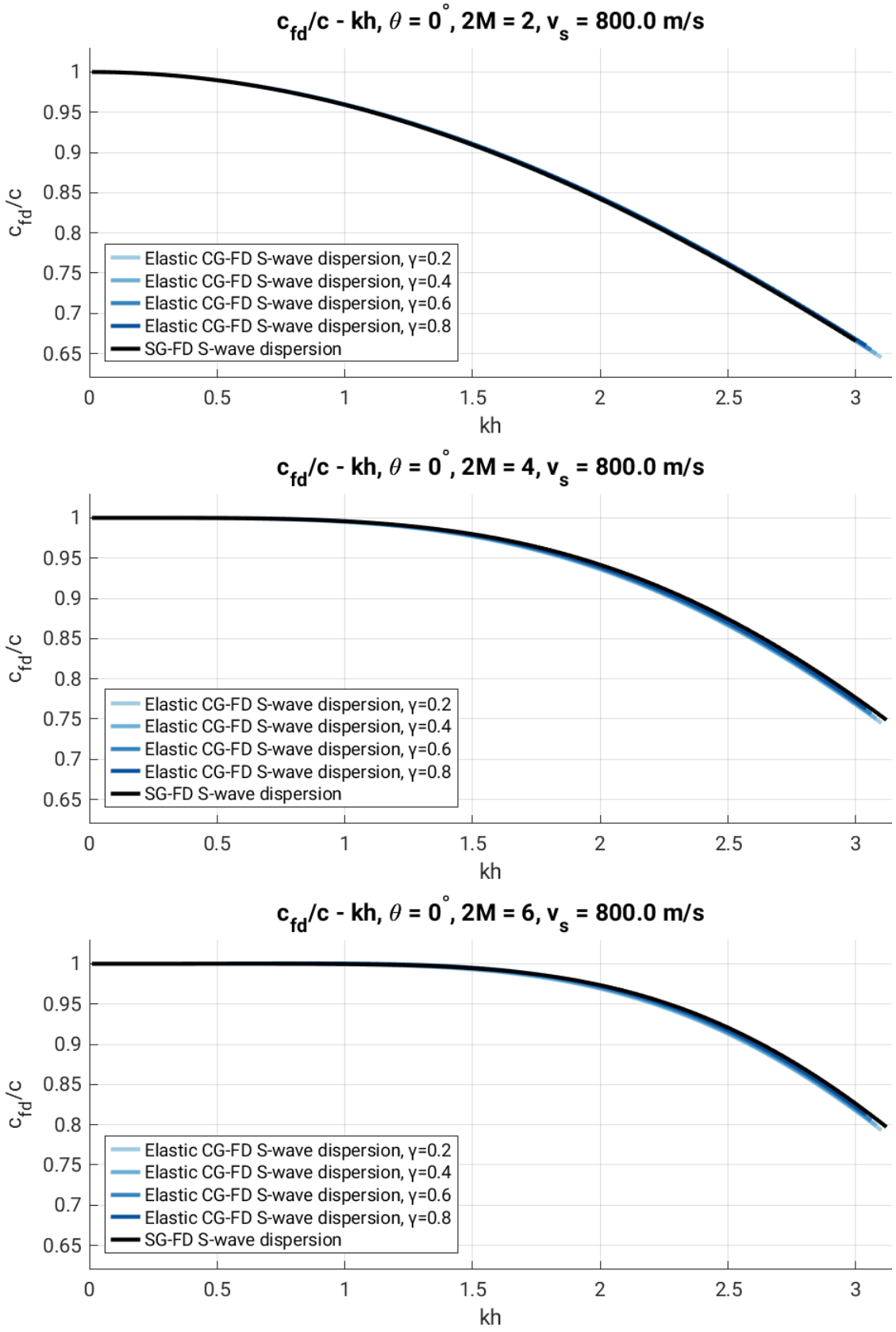

Figure 5.12: *The S-wave dispersion relation c_{fd}/c of CG-FD and SG-FD. $v_s = 800\,\mathrm{m/s}$ corresponds to the homogeneous model of fig. 5.1. Propagation is along the positive direction of x_2-axis.*

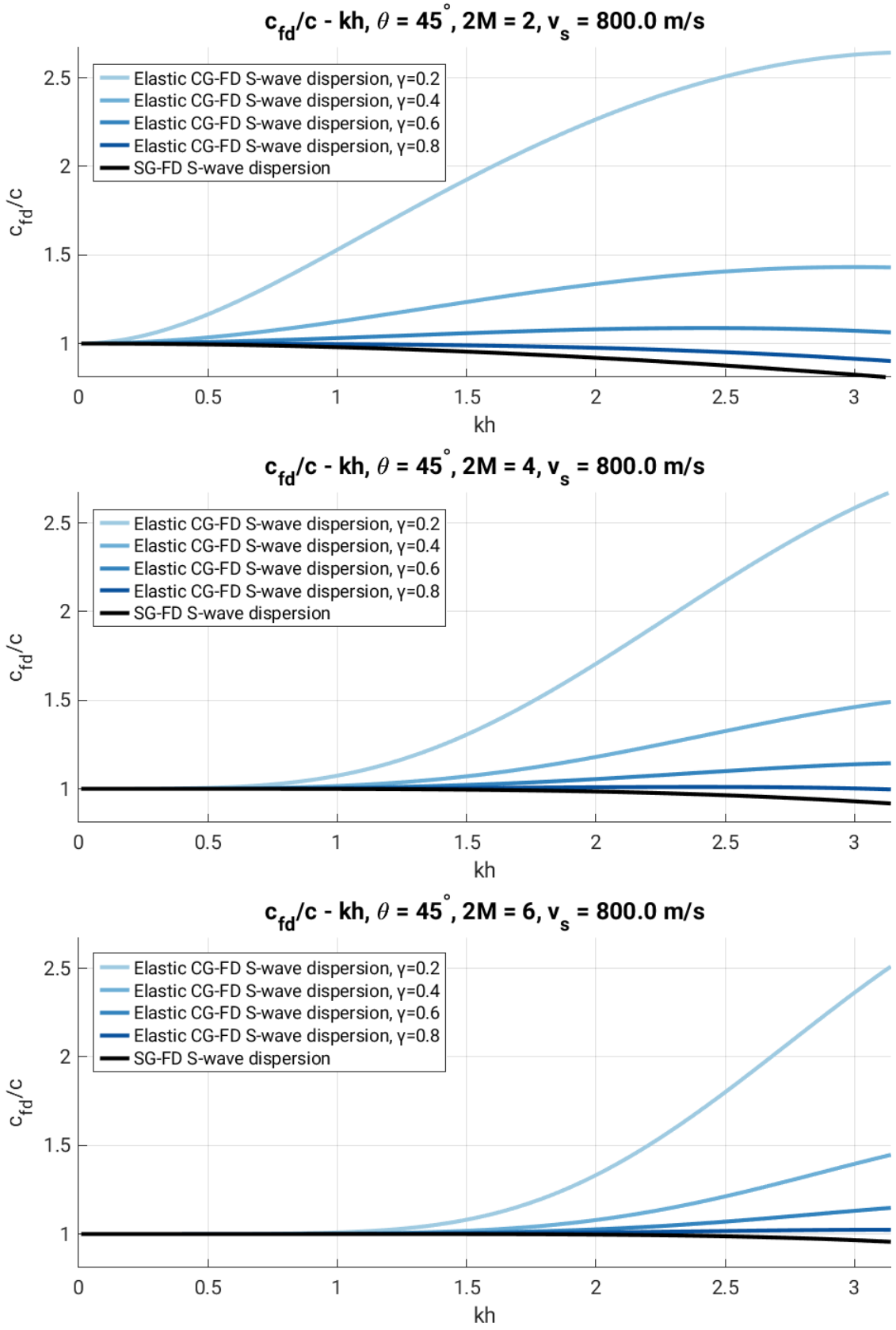

Figure 5.13: *The S-wave dispersion relation c_{fd}/c of CG-FD and SG-FD. $v_s = 800\,\mathrm{m/s}$ corresponds to the homogeneous model of fig. 5.1. Propagation is along the diagonal direction.*

5.5 Accuracy analysis on numerical dispersion

An accuracy analysis of the numerical dispersion is carried out for the reference model used in this thesis. Specifically, we compute the L^2-norm of $c_{\mathrm{fd}}/c - 1$ at $kh \approx 0.2513$ for the P-wave and at $kh \approx 0.6283$ for the S-wave. The value of k follows from $k = 2\pi f_c/c$, where c corresponds to P-wave velocity $v_p = 2000\,\mathrm{m/s}$ or S-wave velocity $v_s = 800\,\mathrm{m/s}$, and $f_c = 80\,\mathrm{Hz}$ is the central frequency of the source used in this thesis. $h = 1\,\mathrm{m}$ is the grid spacing of the FD method. The curves of the error with respect to the propagating angle θ are given in this section. Whenever additional simulation parameters are needed, they follow the homogeneous-medium setup used in chapter 6 if they are used.

5.5.1 Analysis of acoustic CG-FD

Fig. 5.14 shows the results of the accuracy analysis of acoustic CG-FD for different orders of accuracy. The error pattern is symmetric with respect to the axial and diagonal directions. At second order, the error is relatively large and varies strongly with propagation angle. The worst dispersion occurs along the coordinate axes, whereas the smallest error occurs in the diagonal directions. This angular dependence is strongly reduced at higher spatial orders. By sixth order, the remaining angle dependence is very weak.

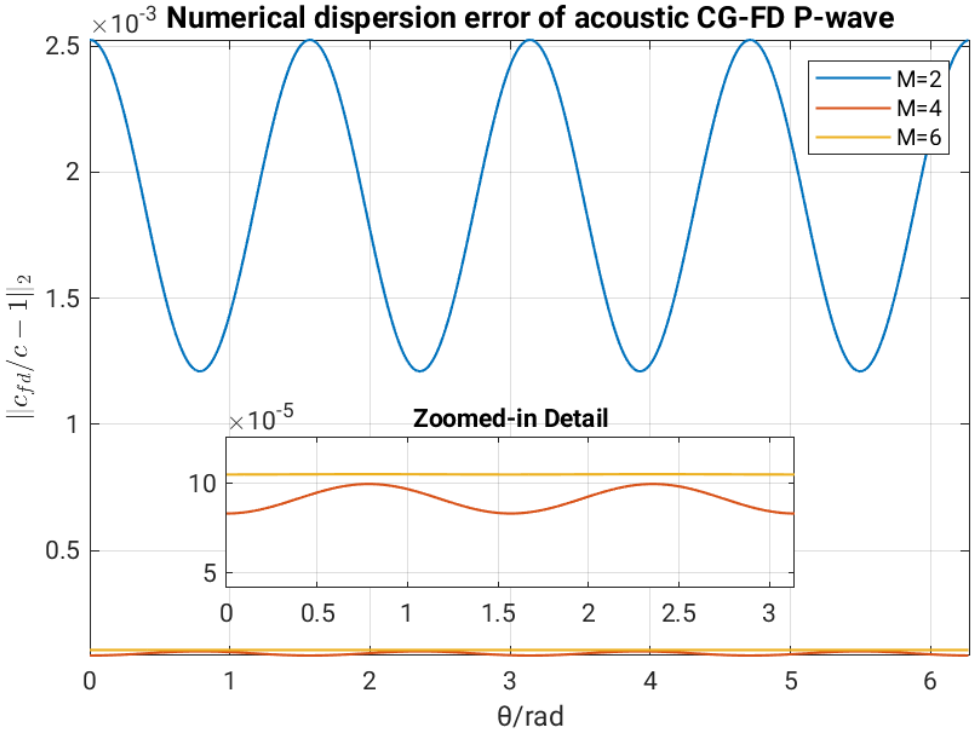

Figure 5.14: *Numerical dispersion error of acoustic CG-FD. The orders of accuracy are the second (blue), fourth (red) and sixth (orange), respectively. The error is calculated by the L^2-norm between c_{fd}/c and 1 when $kh \approx 0.2513$. kh is calculated by $k = 2\pi f_c/v_p$, where $v_p = 2000\,\mathrm{m/s}$, $f_c = 80\,\mathrm{Hz}$ and $h = 1\,\mathrm{m}$. $\Delta t = 0.0001\,\mathrm{s}$.*

Interestingly, it is observed that the sixth-order error curve does not decrease relative to the fourth-order curve. This occurs because the spatial dispersion in the fourth-order scheme effectively compensates for a larger portion of the temporal error. Consequently, the residual error at the sixth order is dominated by temporal rather than spatial dispersion. Additional tests with a smaller time step support this interpretation, although those results

are not shown here.

5.5.2 Analysis of elastic CG-FD

Fig. 5.15 shows the corresponding S-wave dispersion error. Compared with fig. 5.14, the angular dependence is similar in shape but weaker in amplitude. The smallest error occurs along the coordinate axes, whereas the largest error occurs in the diagonal directions, which is the opposite of the acoustic CG-FD case. At second order, the P-wave error is larger than in the acoustic case, but at fourth and sixth-order, the error is reduced to a similarly low level.

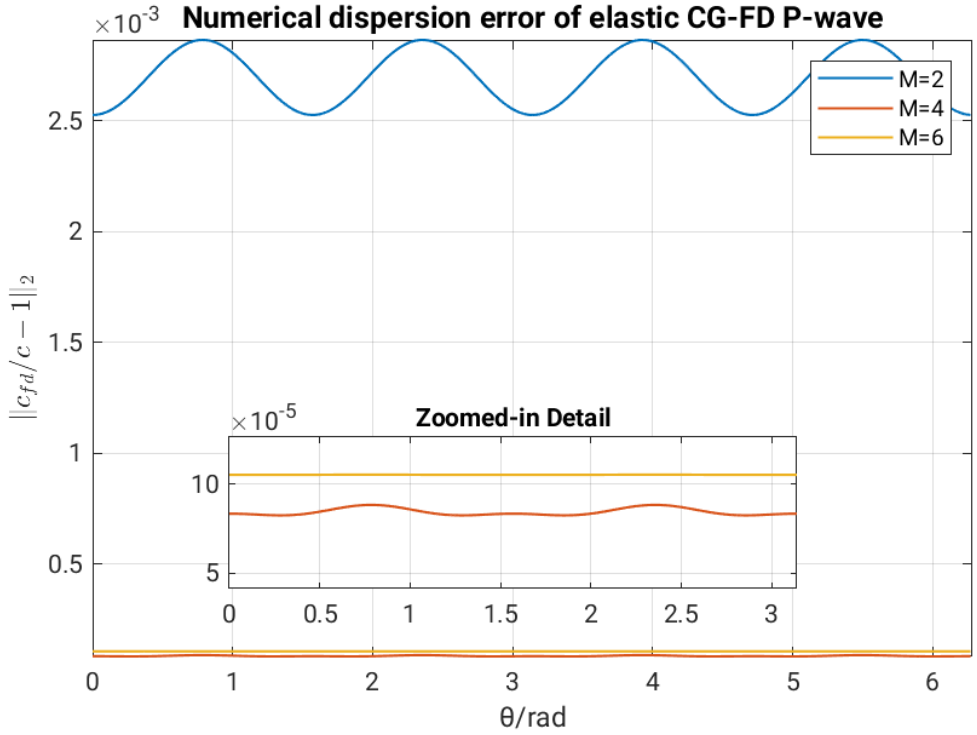

Figure 5.15: *Numerical dispersion error of P-wave in elastic CG-FD ($\gamma = 0.4$). The orders of accuracy are the second (blue), fourth (red) and sixth (orange), respectively. The error is calculated by the L^2-norm between c_{fd}/c and 1 when $kh \approx 0.2513$.*

Fig. 5.16 shows the accuracy analysis results on S-wave dispersion of elastic CG-FD for different orders of accuracy. Compared with the analysis of P-wave, the analysis of S-wave dispersion uses a larger kh, and S-waves have worse dispersion in curves, which causes a much larger error in S-wave dispersion. The error also shows a strong angular dependence. Specifically, the S-wave dispersion is concentrated in the axial and diagonal directions. In particular, the largest values occur near the diagonal directions. Although in the fourth and sixth-order accuracy, the error and the variation with respect to propagating angles are suppressed, the dependence on the propagating angle is still visible.

5.5.3 Analysis of SG-FD

Fig. 5.17 shows the accuracy analysis results on P-wave dispersion of SG-FD. The results are almost same as the results of acoustic CG-FD. Fig. 5.18 shows the accuracy analysis results for S-wave dispersion of SG-FD. The error of S-wave dispersion is larger than that of P-wave dispersion. At second order, both waves show a similar angular variation pattern,

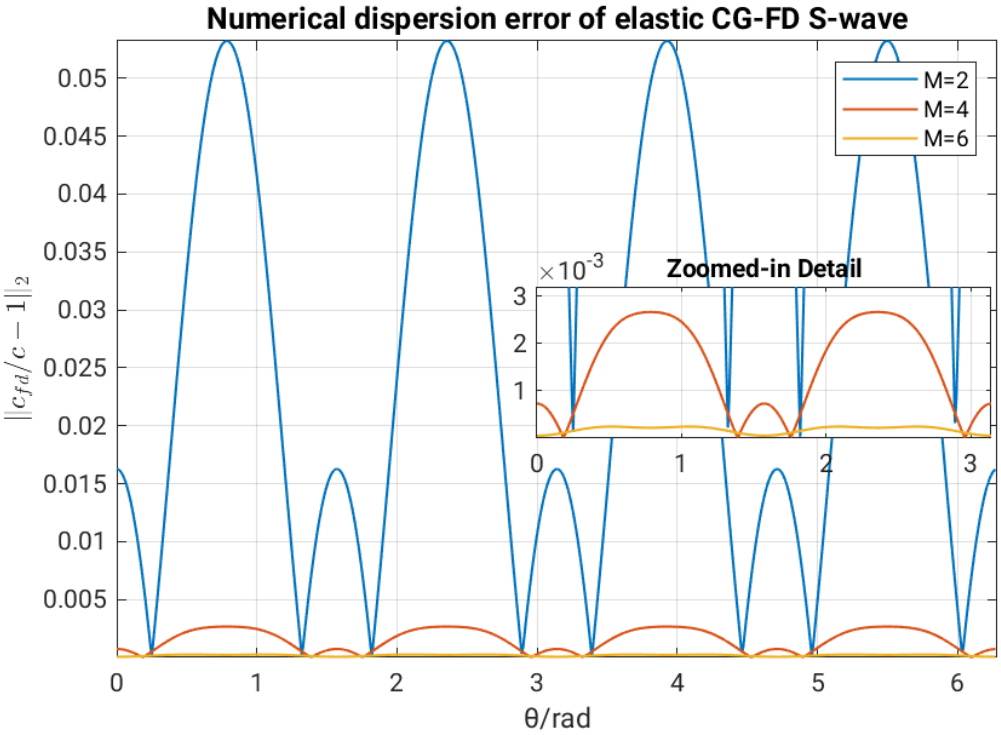

Figure 5.16: *Numerical dispersion error of S-wave in elastic CG-FD ($\gamma = 0.4$). The orders of accuracy are the second (blue), fourth (red) and sixth (orange), respectively. The error is calculated by the L^2-norm between c_{fd}/c and 1 when $kh \approx 0.6283$. kh is calculated by $k = 2\pi f_c/v_s$, where $v_s = 800\,\mathrm{m/s}$, $f_c = 80\,\mathrm{Hz}$ and $h = 1\,\mathrm{m}$. $\Delta t = 0.0001\,\mathrm{s}$.*

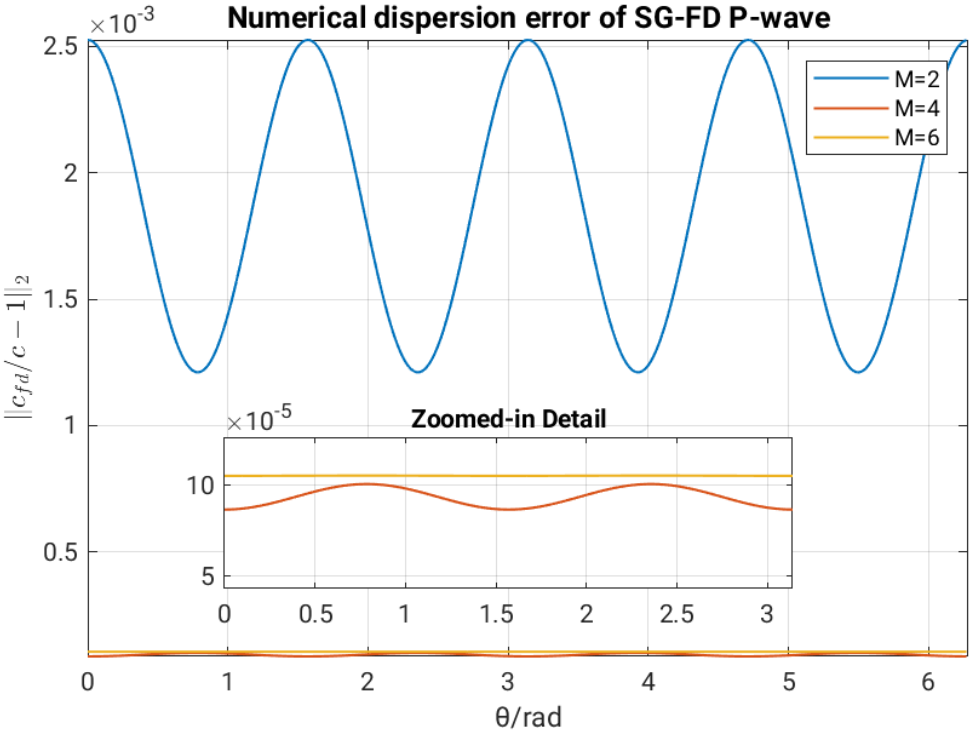

Figure 5.17: *Numerical dispersion error of P-wave in elastic SG-FD. The orders of accuracy are the 2nd (blue), 4th (orange), and 6th (yellow), respectively. The error is calculated by the L^2-norm between c_{fd}/c and 1 when $kh \approx 0.2513$.*

whereas at sixth order the angular dependence remains more visible for the S-wave than for the P-wave.

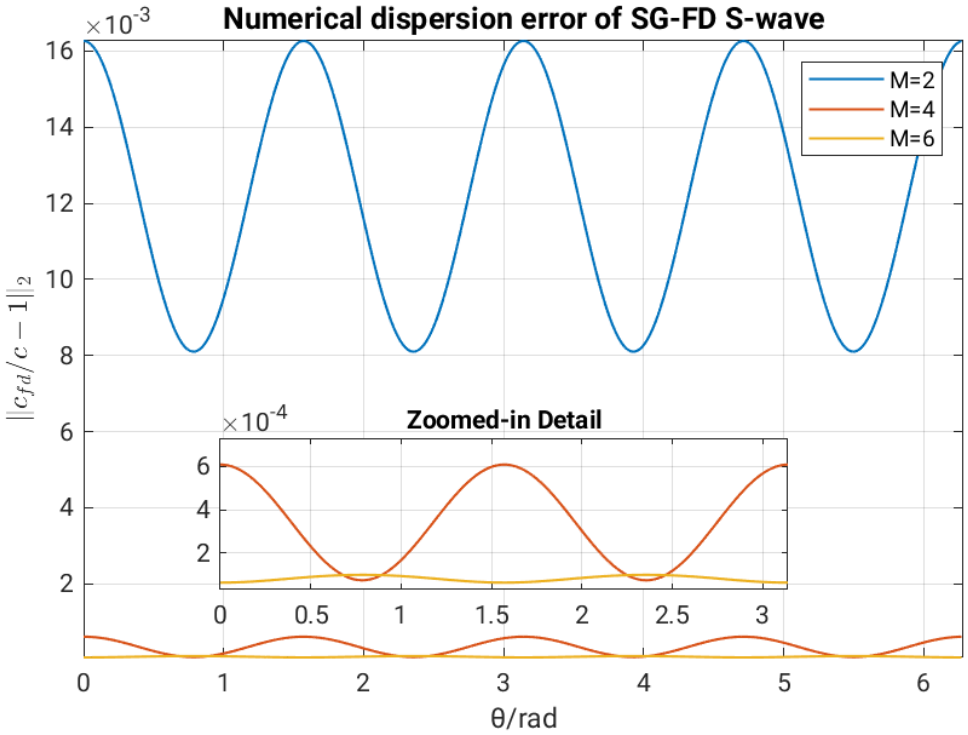

Figure 5.18: *Numerical dispersion error of S-wave in elastic SG-FD. The orders of accuracy are the 2nd (blue), 4th (orange), and 6th (yellow), respectively. The error is calculated by the L^2-norm between c_{fd}/c and 1 when $kh \approx 0.6283$.*

Chapter 6

Results of Homogeneous Media

This chapter presents and analyzes the results of the FD method simulation, including snapshots and seismograms in homogeneous media. Specifically, snapshots show the wavefield propagation; seismograms, derived from the receiver, show the simulated waveforms and are compared with analytical solutions. Furthermore, this chapter also performs an accuracy analysis, comparing the numerical dispersion curves presented in chapter 4. The homogeneous model used throughout this chapter is the one introduced in section 5.1. Specific analyzes are divided into elastic and acoustic cases.

6.1 Acoustic FD results in homogeneous media

6.1.1 Snapshots and seismograms

CG-FD results

For acoustic CG-FD, the simulations are based on the second-order acoustic wave equation, and the resulting pressure snapshots are shown in fig. 6.1. The snapshots for the second, fourth, and sixth-order schemes all reproduce the expected wavefield clearly. Only minor visual differences are observed between the different spatial orders, and even the second-order result is already satisfactory for this simple homogeneous test.

The red point in the snapshots is the source point, and the blue points indicate the receiving points. Fig. 6.2 shows the corresponding normalized pressure seismograms together with the analytical solutions. The results show that, under acoustic conditions, the CG-FD seismograms already agree closely with the analytical solution at second order. In this configuration, increasing the spatial order produces only minor additional improvement.

SG-FD results

Fig. 6.3 shows the corresponding acoustic SG-FD pressure snapshots for different spatial orders. The same receiver configuration is used as in the CG-FD case, and the resulting pressure seismograms are shown in fig. 6.4. The SG-FD results lead to the same overall assessment as the CG-FD results: both the snapshots and the seismograms agree very well with the expected acoustic wavefield behavior.

Overall, in the acoustic case, both CG-FD and SG-FD reproduce the homogeneous wavefield satisfactorily, with almost no visually discernible dispersion. This observation is fully consistent with the dispersion analysis shown in fig. 5.10 and 5.11.

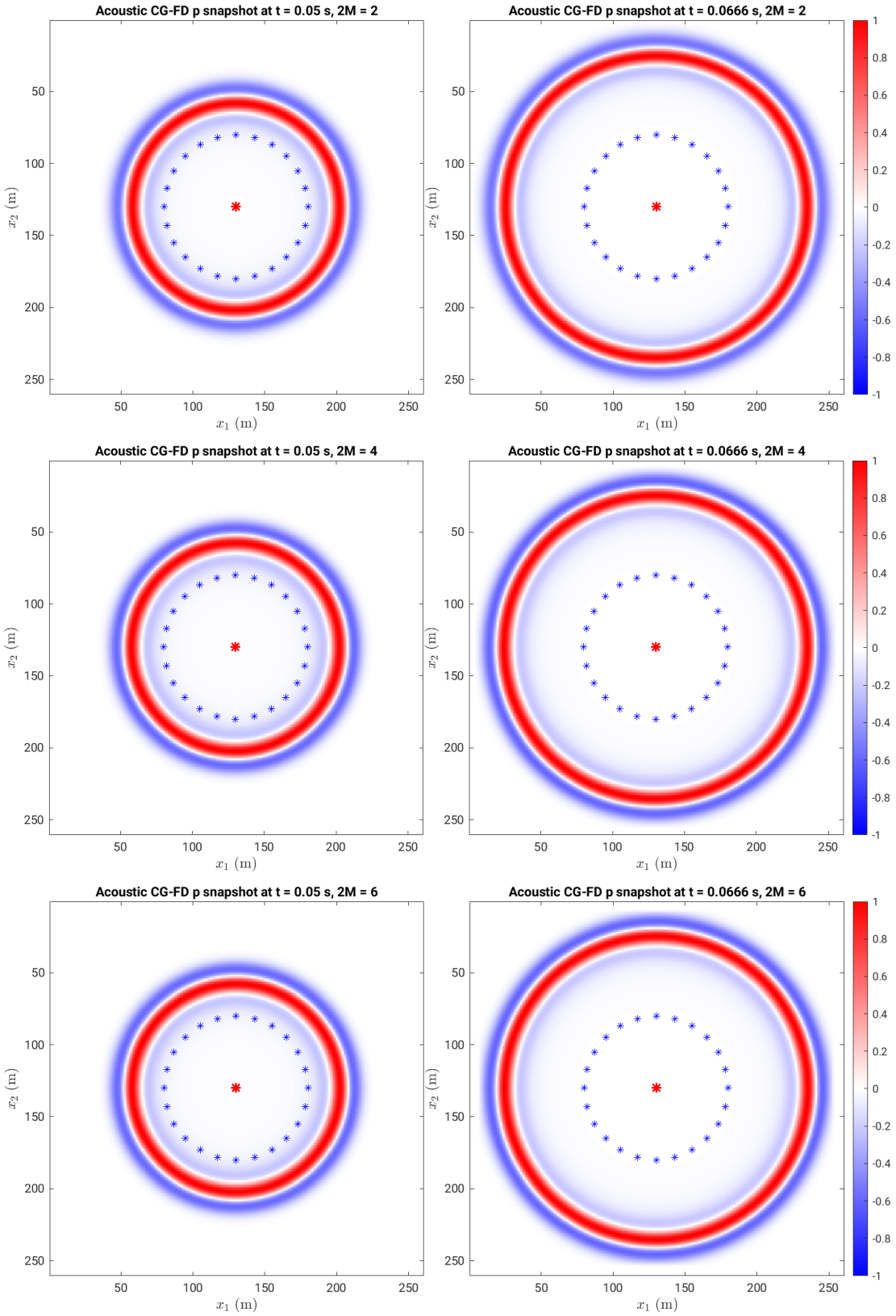

Figure 6.1: *Acoustic CG-FD pressure snapshots at* $0.05\,\mathrm{s}$ *(left) and* $0.0666\,\mathrm{s}$ *(right). The CG-FD is of second (top), fourth (mid) and sixth-order (bottom) accuracy. The model is homogeneous model in fig. 5.1. Grid spacing is* $h = 1\,\mathrm{m}$ *and time interval is* $\Delta t = 0.0001\,\mathrm{s}$*. The following all snapshots use this model and grid configuration. The waveform is excited at source point (red) and spread on 2D plane, passing the receiver points (blue).*

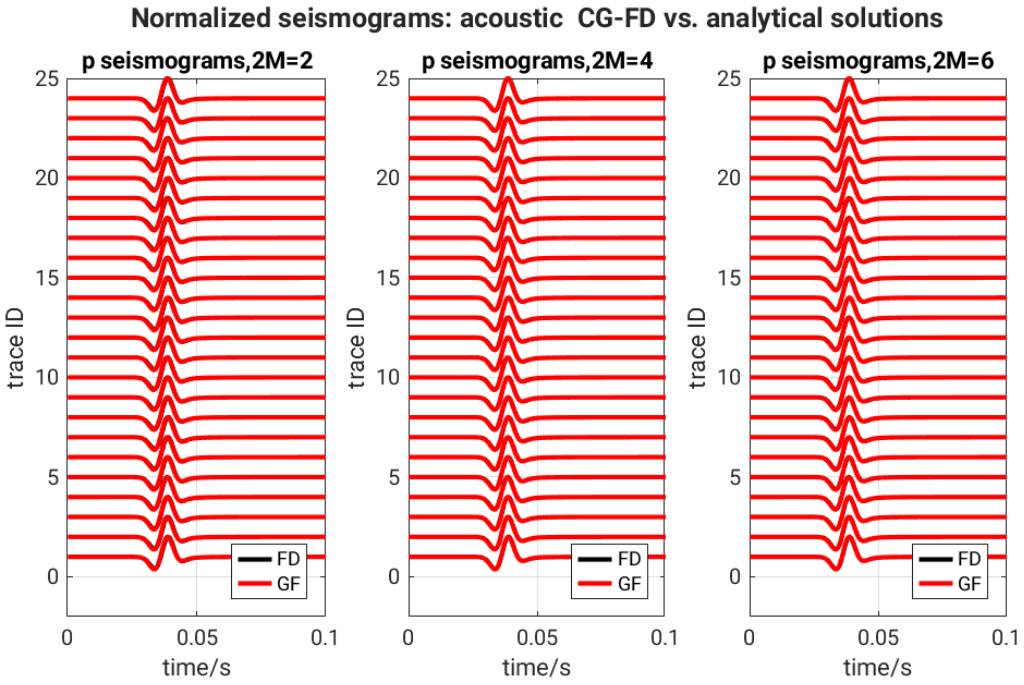

Figure 6.2: *A comparison of normalized pressure seismograms between acoustic CG-FD results (black) and analytical solutions (red) in different orders of accuracy. The Green's function solution is used as analytical solution.*

6.1.2 Accuracy analysis

Although both methods perform very well in the acoustic case, a quantitative error analysis is still useful in order to resolve the small differences between the numerical results and the analytical benchmark. For this purpose, we compute the L^2-norm between the waveform and the analytical solution. Figs. 6.5 and 6.6 show these results.

However, it should be noted that the figures are not directly comparable with the dispersion-curves error in section 5.5 because the latter are evaluated at a single frequency corresponding to f_c, whereas the seismogram errors are based on a finite source bandwidth.

Both figs. 6.5 and fig. 6.6 show that the seismogram error depends on propagation angle and reaches its maximum in the axial directions. This angular dependence is reduced substantially by increasing the spatial order and becomes almost negligible at sixth order. A comparison between the two figures shows that CG-FD yields slightly smaller errors than SG-FD in the acoustic case, which is consistent with the small difference already suggested by the dispersion analysis.

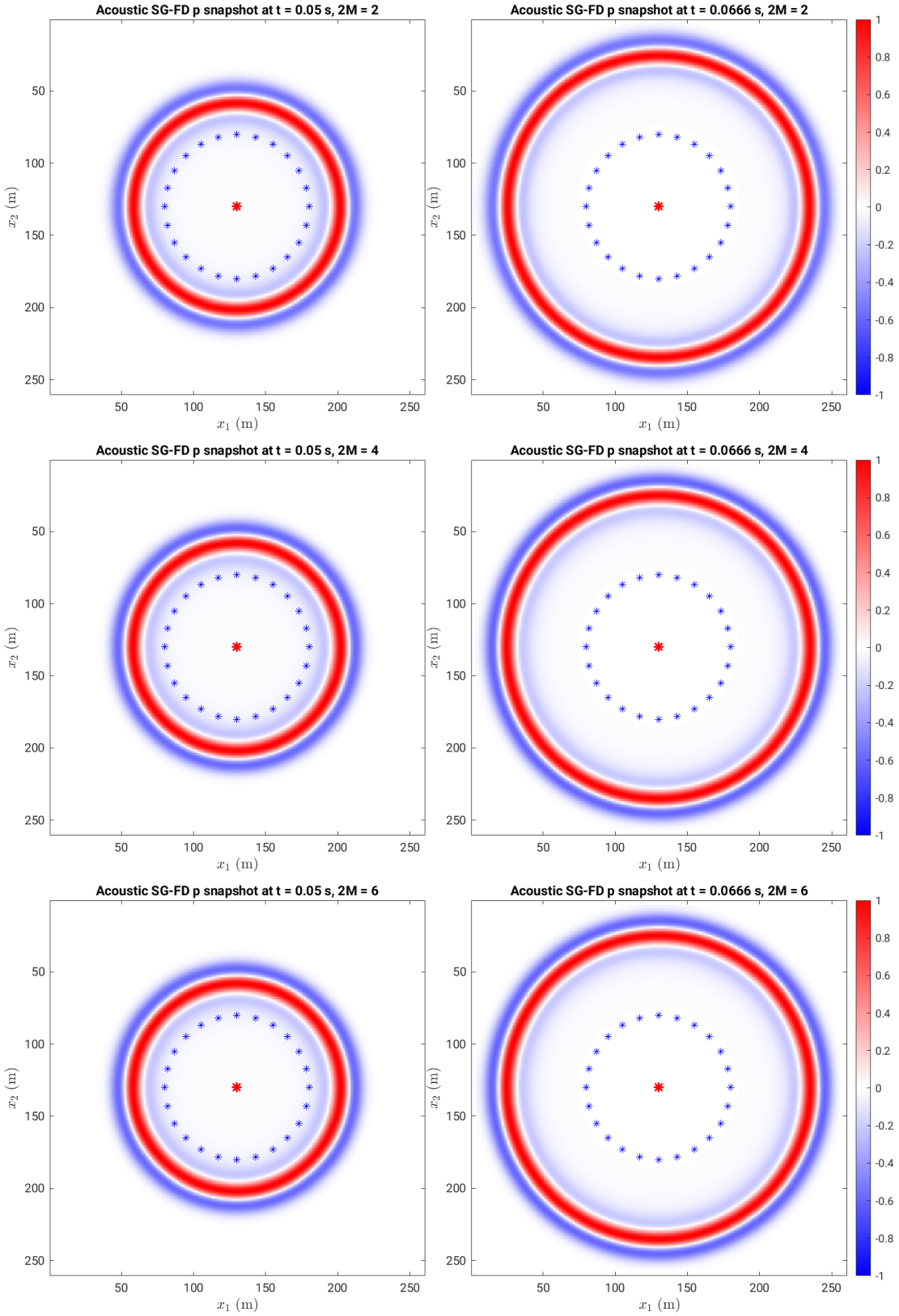

Figure 6.3: *Acoustic SG-FD pressure snapshots at* 0.05 s *(left) and* 0.0666 s *(right). The SG-FD is of second (top), fourth (mid) and sixth-order (bottom) accuracy, respectively. The results use same configuration as CG-FD.*

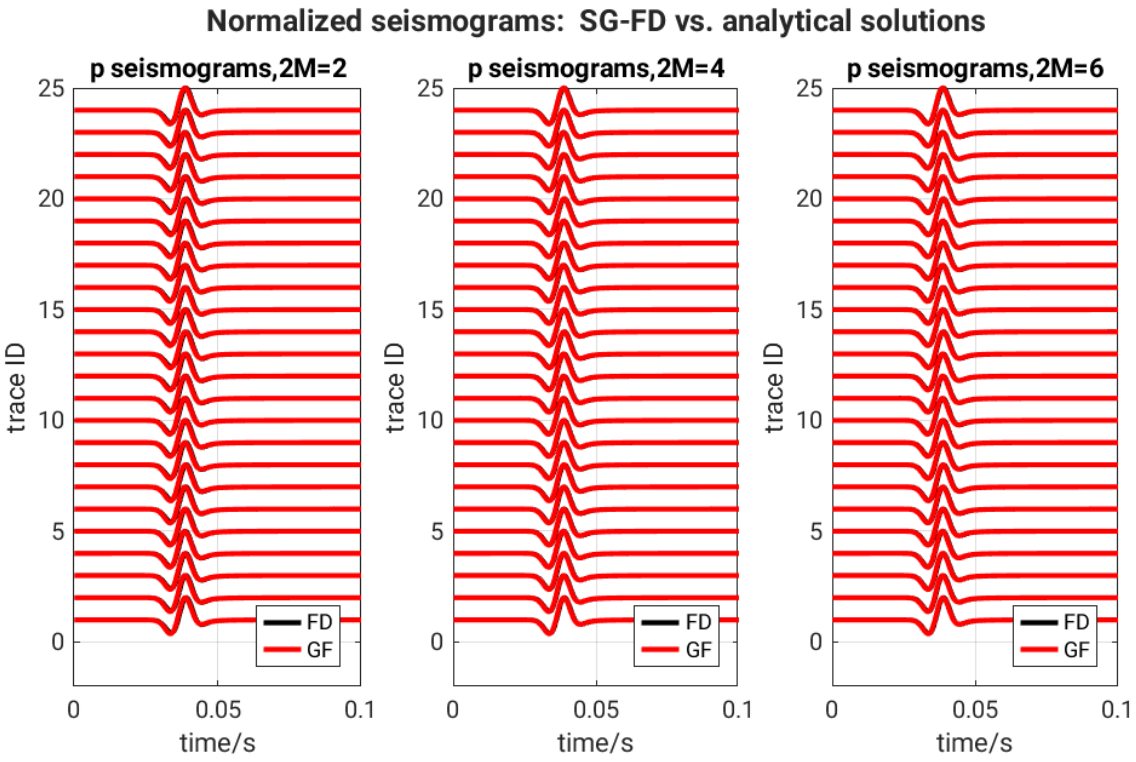

Figure 6.4: *A comparison of normalized pressure seismograms between acoustic SG-FD results (black) and analytical solutions (red) in different orders of accuracy. The results use same configuration as CG-FD.*

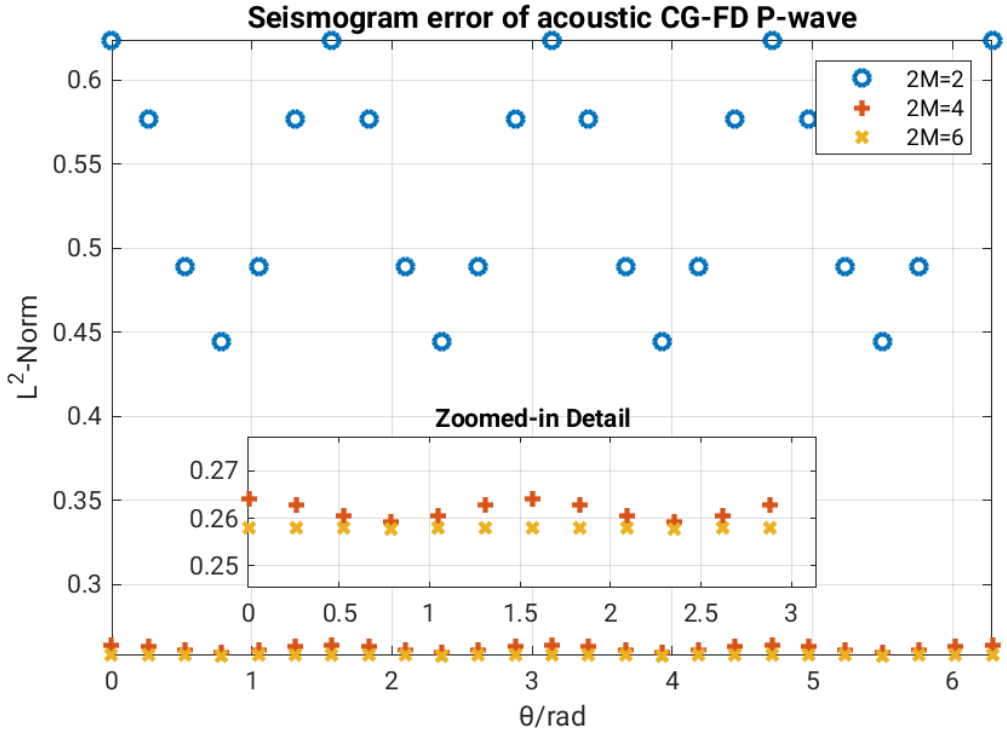

Figure 6.5: *L^2-norm error between the seismograms in acoustic CG-FD and analytical solutions as a function of propagation angle. The model is homogeneous model. The orders of accuracy are 2nd (blue), 4th (orange), and 6th (yellow), respectively. Both the seismograms and analytical solutions are obtained from fig. 6.2.*

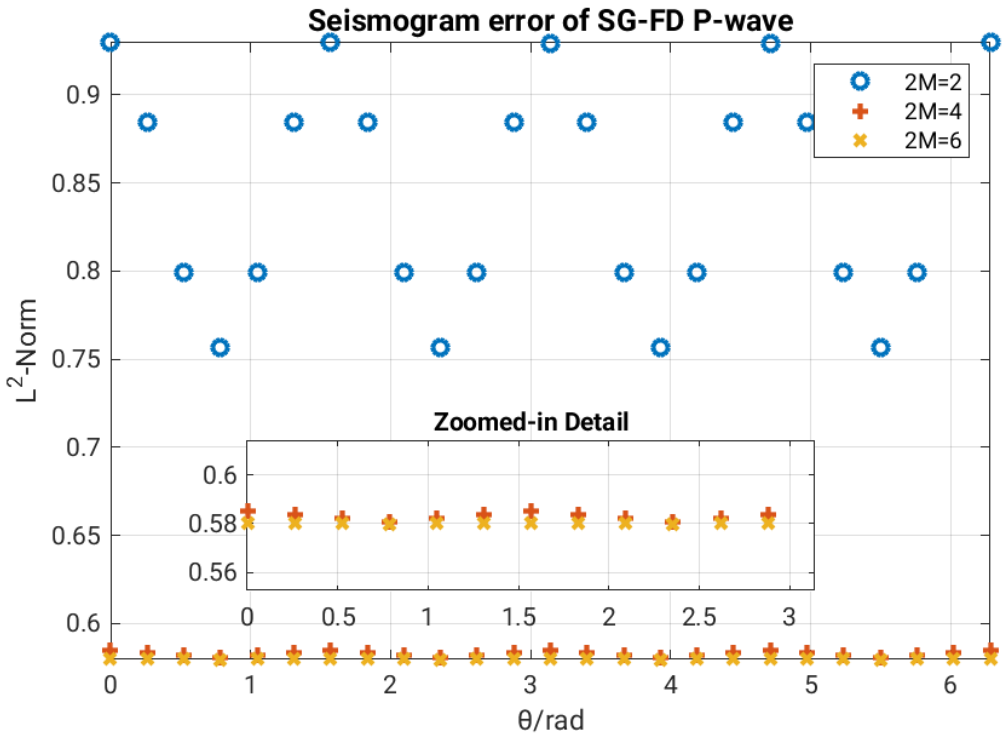

Figure 6.6: *L^2-norm error between the seismograms in acoustic SG-FD and analytical solutions as a function of propagation angle. The model is homogeneous model. The orders of accuracy are 2nd (blue), 4th (orange), and 6th (yellow), respectively. Both the seismograms and analytical solutions are obtained from fig. 6.4.*

6.2 Elastic FD results in homogeneous media

6.2.1 Snapshots and seismograms

CG-FD results

For elastic CG-FD, based on the second-order elastic wave equation, we simulated snapshots of the wavefield of u_1 and u_2.

Figs. 6.7 and 6.8 show the corresponding snapshots for different spatial orders. The wavefields are reproduced clearly in all cases, but visible numerical dispersion remains at a low order. The most prominent dispersion is associated with the S-wave, which is consistent with the dispersion curves discussed in section 5.4, where the S-wave was shown to be more sensitive than the P-wave.

Moreover, the S-wave dispersion exhibits opposite behavior in the axial and diagonal directions. This effect is especially clear in the second-order u_2 results shown in fig. 6.8. Along the diagonal directions, the dispersion is concentrated near the wavefront, whereas along the coordinate axes, it is more visible in the trailing part of the wave packet. This behavior agrees with the dispersion relations shown in figs. 5.12 and 5.13.

The corresponding receiver seismograms are compared with the analytical solutions in figs. 6.9 and 6.10. At second order, the P-wave part of the seismograms already agrees reasonably well with the analytical solution, whereas the S-wave part shows strong numerical dispersion. This situation improves markedly at higher spatial order. At sixth order, the numerical seismograms almost coincide with the analytical solution.

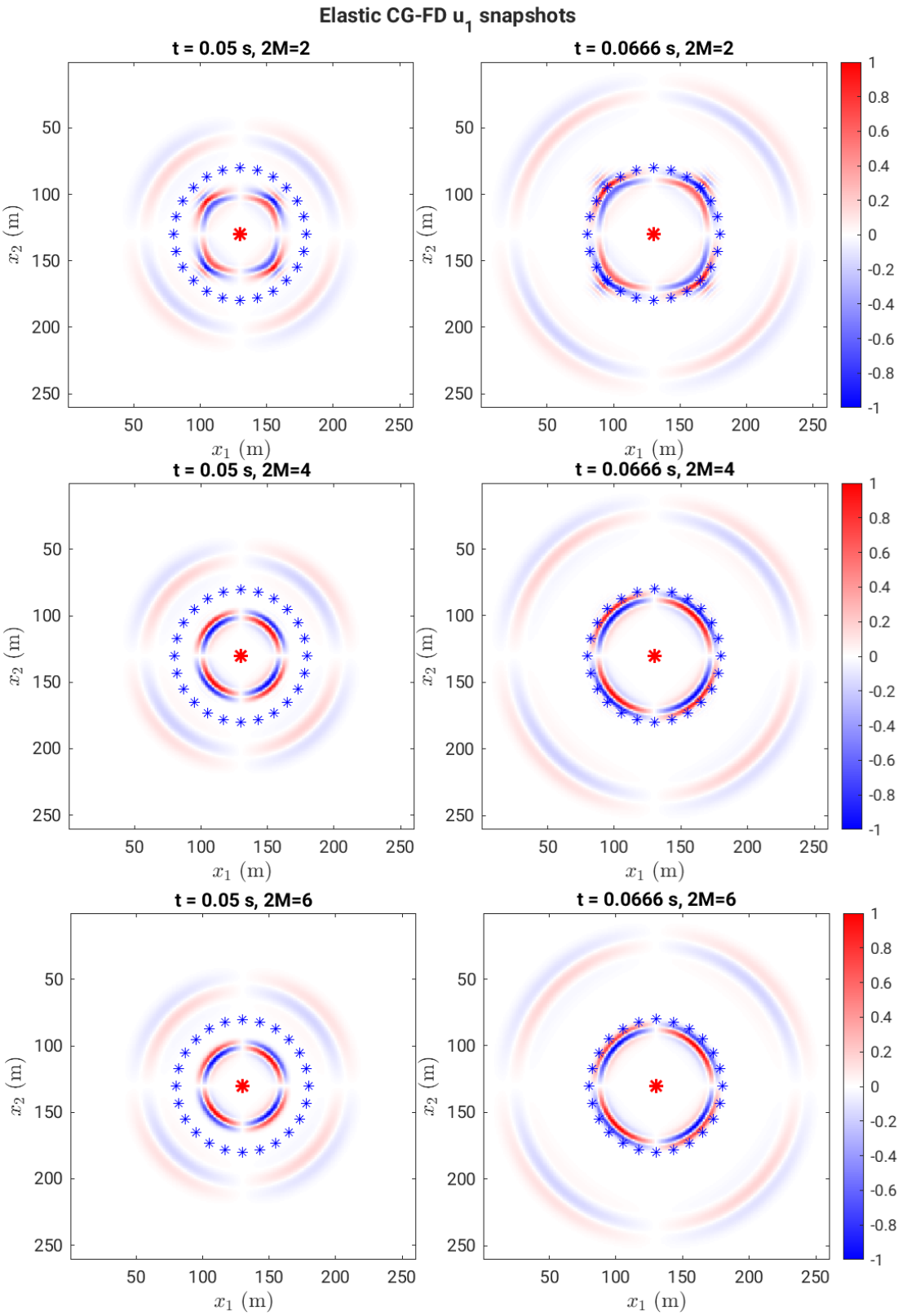

Figure 6.7: *Elastic CG-FD snapshots of* u_1 *at* $0.05\,\mathrm{s}$ *(left) and* $0.0666\,\mathrm{s}$ *(right). The CG-FD is of second (top), fourth (mid) and sixth-order (bottom) accuracy, respectively. The model is homogeneous model in fig. 5.1. Grid spacing is* $h = 1\,\mathrm{m}$ *and time interval is* $\Delta t = 0.0001\,\mathrm{s}$*. The following all snapshots use this model and grid configuration. The waveform is excited at source point (red) and spread on 2D plane, passing the receiver points (blue).*

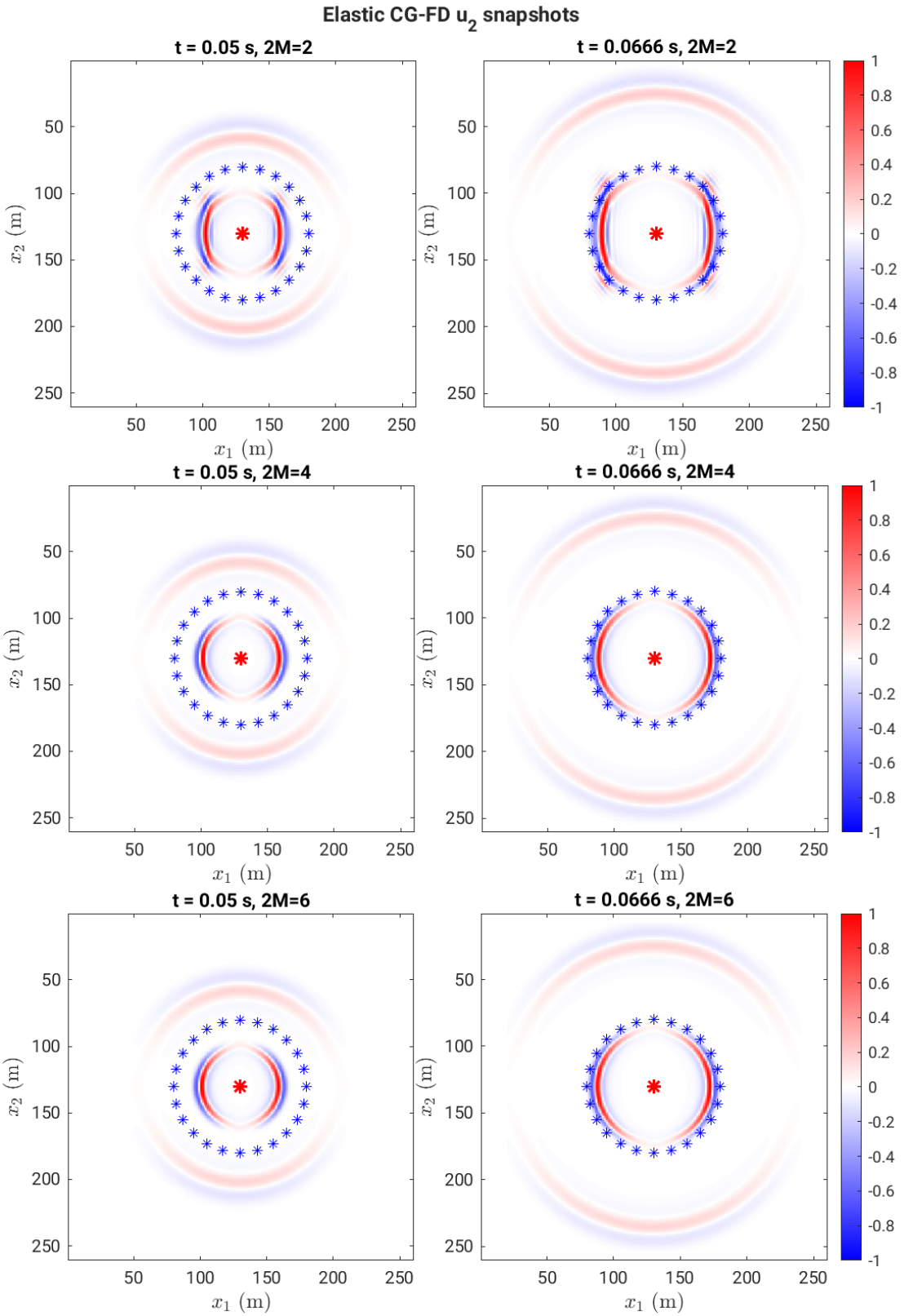

Figure 6.8: *Elastic CG-FD snapshots of* u_2 *at* 0.05 s *(left) and* 0.0666 s *(right). The CG-FD is of second (top), fourth (mid) and sixth-order (bottom) accuracy, respectively. The figure uses the same configuration with fig. 6.7.*

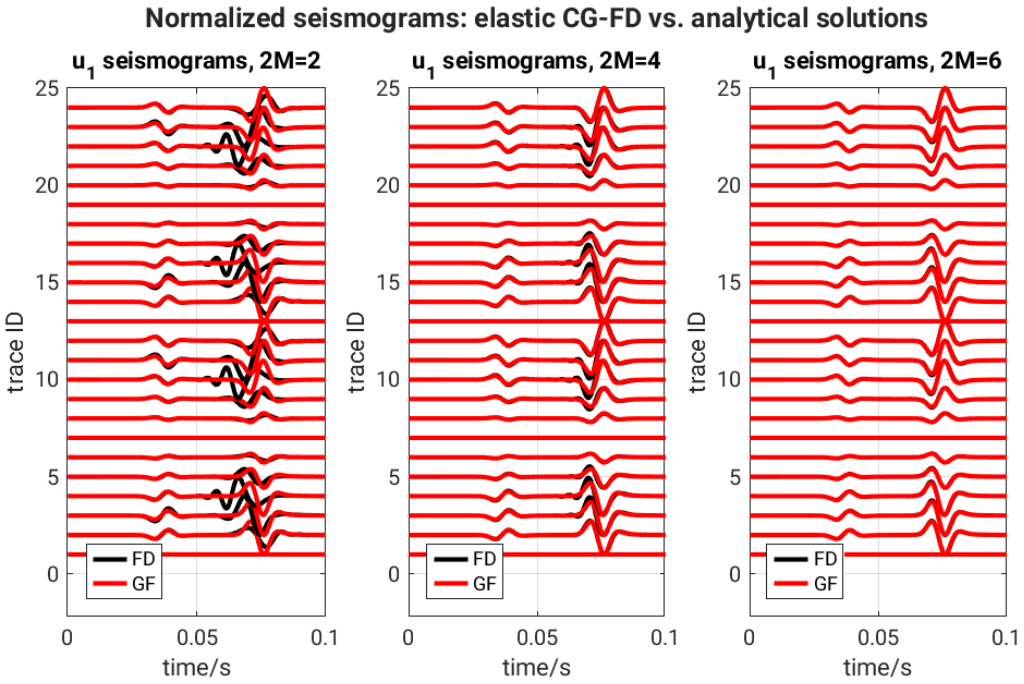

Figure 6.9: *A comparison of normalized u_1 seismograms between elastic CG-FD results (black) and analytical solutions (red) in different orders of accuracy. The Green's function solution is used as analytical solution.*

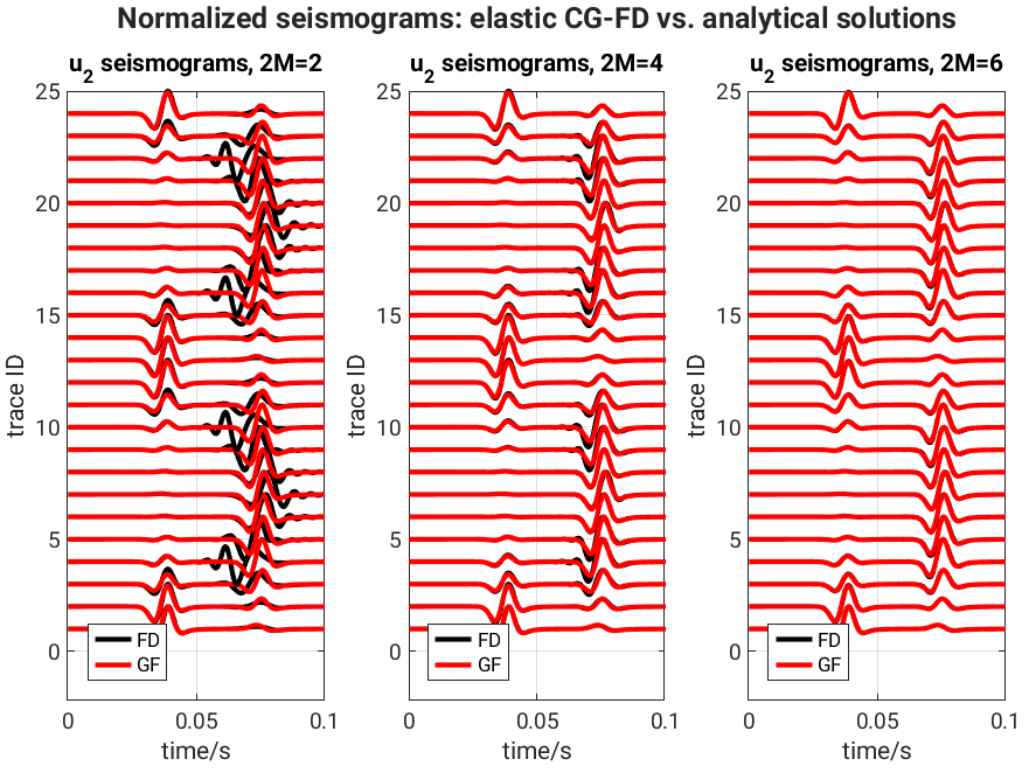

Figure 6.10: *A comparison of normalized u_2 seismograms between elastic CG-FD results (black) and analytical solutions (red) in different orders of accuracy. The Green's function solution is used as analytical solution.*

SG-FD results

We perform the same analysis for SG-FD, which is based on the first-order elastic wave equation. Figs. 6.11 and 6.12 show the v_1 and v_2 snapshots for different spatial orders, and figs. 6.13 and 6.14 show the corresponding seismograms together with the analytical solutions.

In the elastic case, we compare the wavefield snapshots and seismograms between the SG-FD and CG-FD schemes. Overall, the SG-FD snapshots exhibit noticeably less numerical dispersion. The SG-FD seismograms match the analytical solutions well; for the second-order accurate scheme, the visible dispersion is exclusively concentrated at the trailing edge of the wave packet. This behavior differs significantly from the CG-FD results, where the S-wave dispersion artifacts can appear at both the leading and trailing edges.

Overall, both CG-FD and SG-FD work well in the elastic homogeneous case. However, CG-FD requires a higher spatial order to reach the same level of accuracy because SG-FD inherently exhibits weaker numerical dispersion.

6.2.2 Accuracy analysis

A quantitative error analysis is performed for both methods by computing the L^2-norm between the waveform and the analytical solution. Figs. 6.15 – 6.18 show these results.

The analysis shows that the dominant contribution to the numerical error comes from the S-wave. In general, SG-FD yields smaller overall errors than CG-FD. At the same time, the spatial symmetry of the error patterns differs between the two schemes. In CG-FD, the errors for both u_1 and u_2 show a highly symmetric angular distribution. In SG-FD, by contrast, only the v_2 component preserves this symmetry, whereas the v_1 component exhibits a clearly asymmetric error pattern.

A plausible explanation is related to the staggered placement of the variables and the source injection strategy. In the SG-FD implementation, the vertical force source is injected directly at the v_2 nodes. In the standard 2D SG-FD layout, the velocity components are spatially offset in different orthogonal directions: v_1 nodes are shifted by half a grid spacing in the horizontal direction, while the vertical velocity v_2 nodes are shifted by half a grid spacing in the vertical direction. When a vertical force source is injected directly at the v_2 nodes, the source location is inherently asymmetric with respect to the staggered v_1 grid layout. This two-dimensional geometric offset inherently breaks the symmetry of the v_1 error distribution. In contrast, the CG-FD method defines all wavefield variables at the exact same spatial nodes, completely avoiding this geometric offset and thereby preserving a perfectly symmetric error distribution.

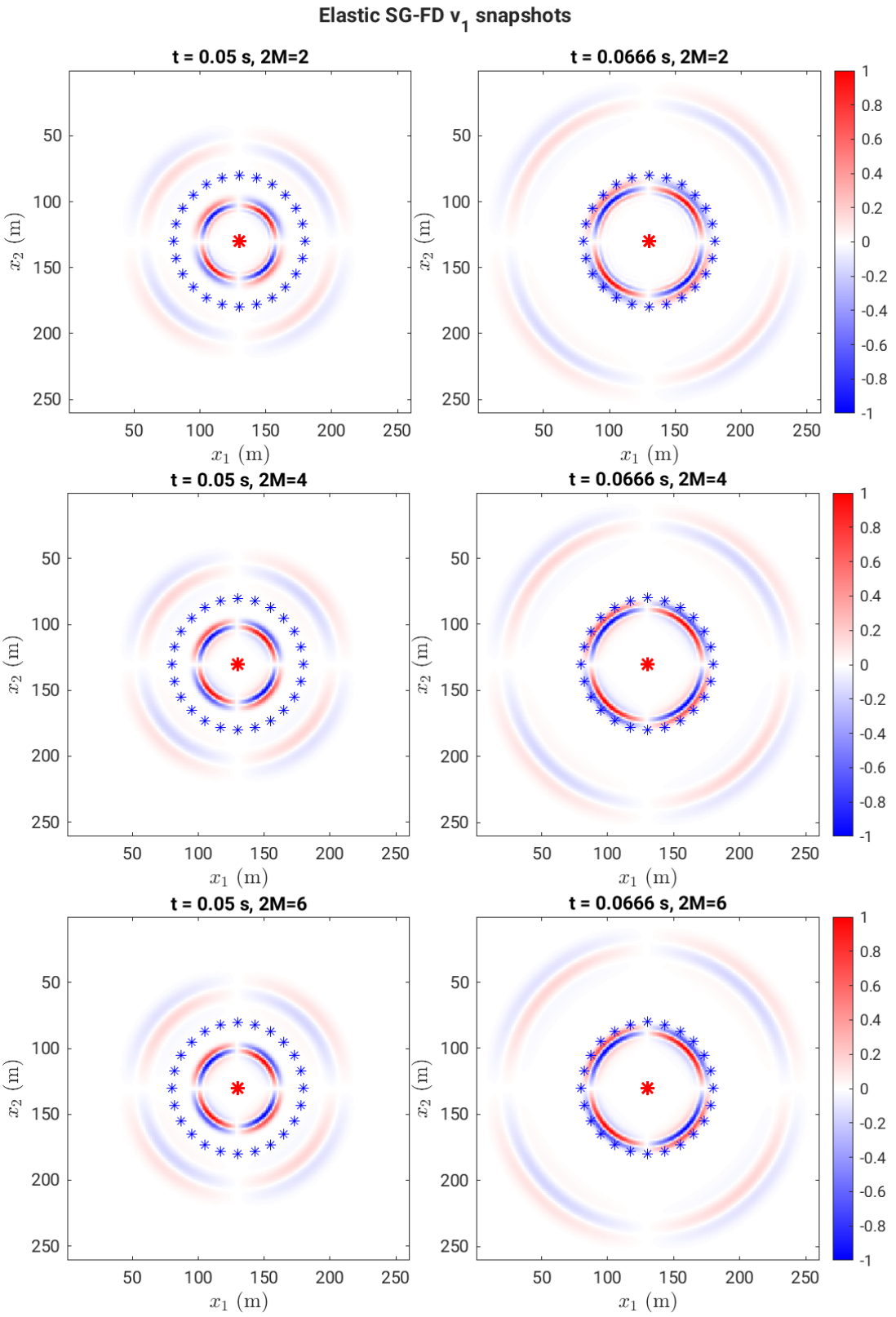

Figure 6.11: *Elastic SG-FD snapshots of* v_1 *at* $0.05\,\mathrm{s}$ *(left) and* $0.0666\,\mathrm{s}$ *(right). The SG-FD results are of second (top), fourth (mid) and sixth (bottom) orders accuracy, respectively. The model is homogeneous model in fig. 5.1. Grid spacing is* $h = 1\,\mathrm{m}$ *and time interval is* $\Delta t = 0.0001\,\mathrm{s}$*. The following all snapshots use this model and grid configuration. The waveform is excited at source point (red) and spread on 2D plane, passing the receiver points (blue).*

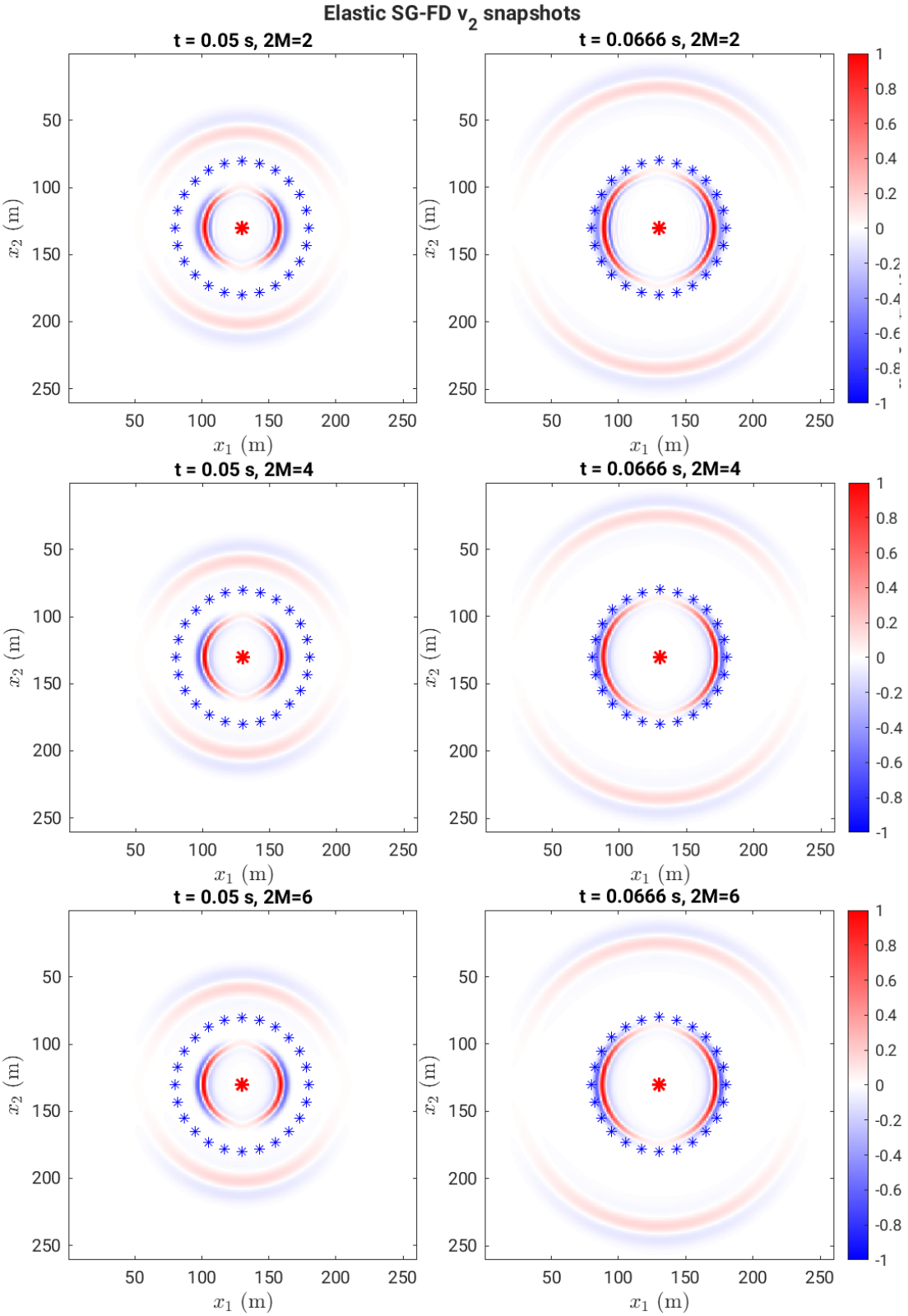

Figure 6.12: *Elastic SG-FD snapshots of v_2 at 0.05 s (left) and 0.0666 s (right). The SG-FD results are of second (top), fourth (mid) and sixth (bottom) orders accuracy, respectively. The figure uses the same configuration as fig. 6.11.*

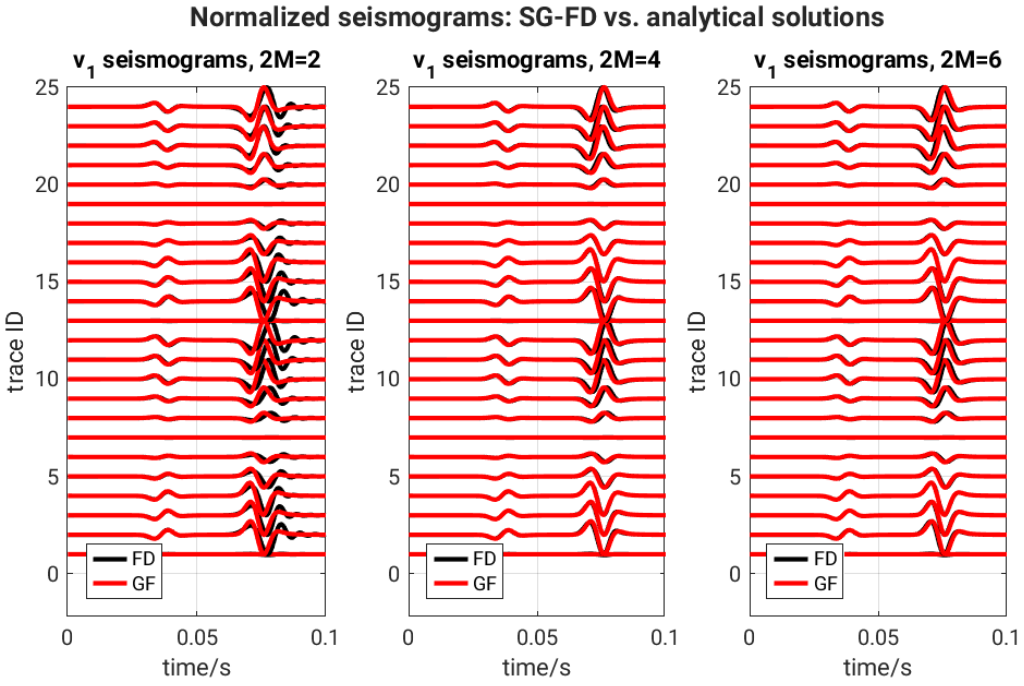

Figure 6.13: *A comparison of normalized v_1 seismograms between elastic SG-FD results (black) and analytical solutions (red) in different orders of accuracy. The Green's function solution is used as analytical solution.*

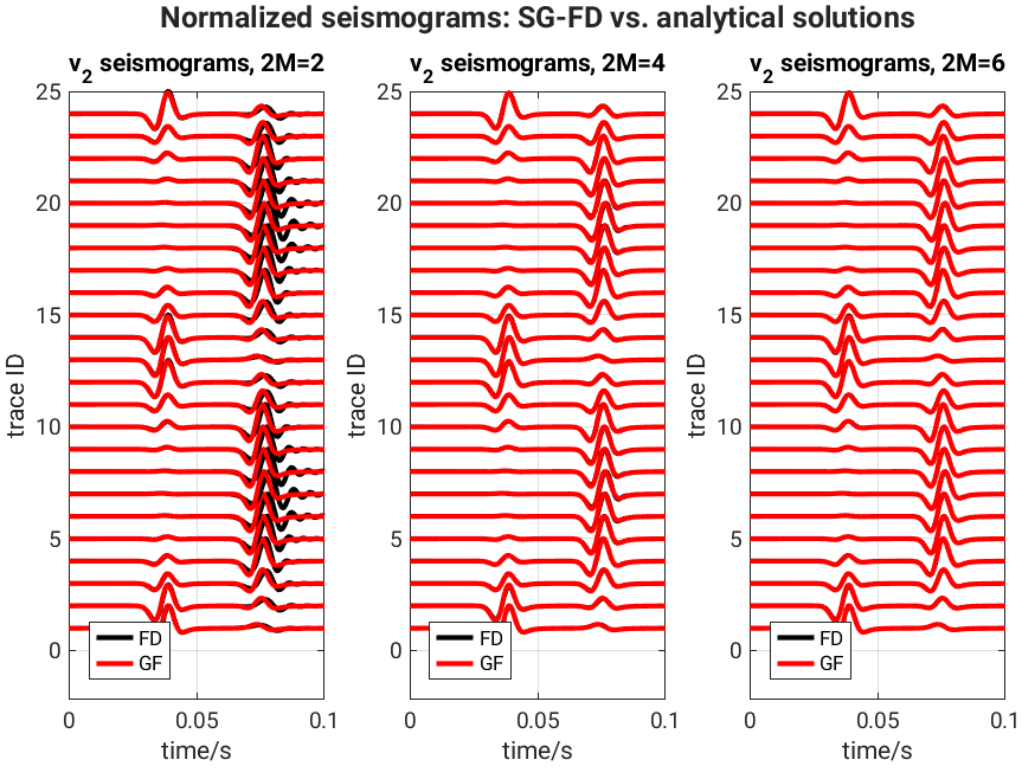

Figure 6.14: *A comparison of normalized v_2 seismograms between elastic SG-FD results (black) and analytical solutions (red) in different orders of accuracy. The Green's function solution is used as analytical solution.*

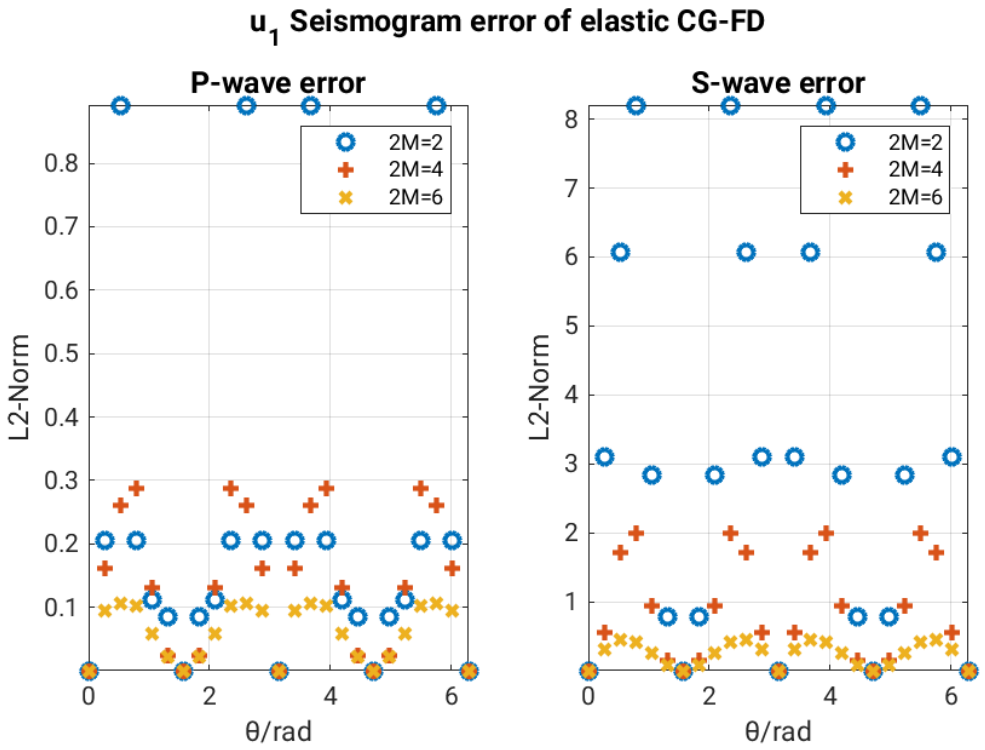

Figure 6.15: *L^2-norm error between the u_1 seismograms in elastic CG-FD and analytical solutions as a function of propagation angle. The model is homogeneous model. The orders of accuracy are 2nd (blue), 4th (orange), and 6th (yellow). Both the seismograms and analytical solutions are obtained from fig. 6.9.*

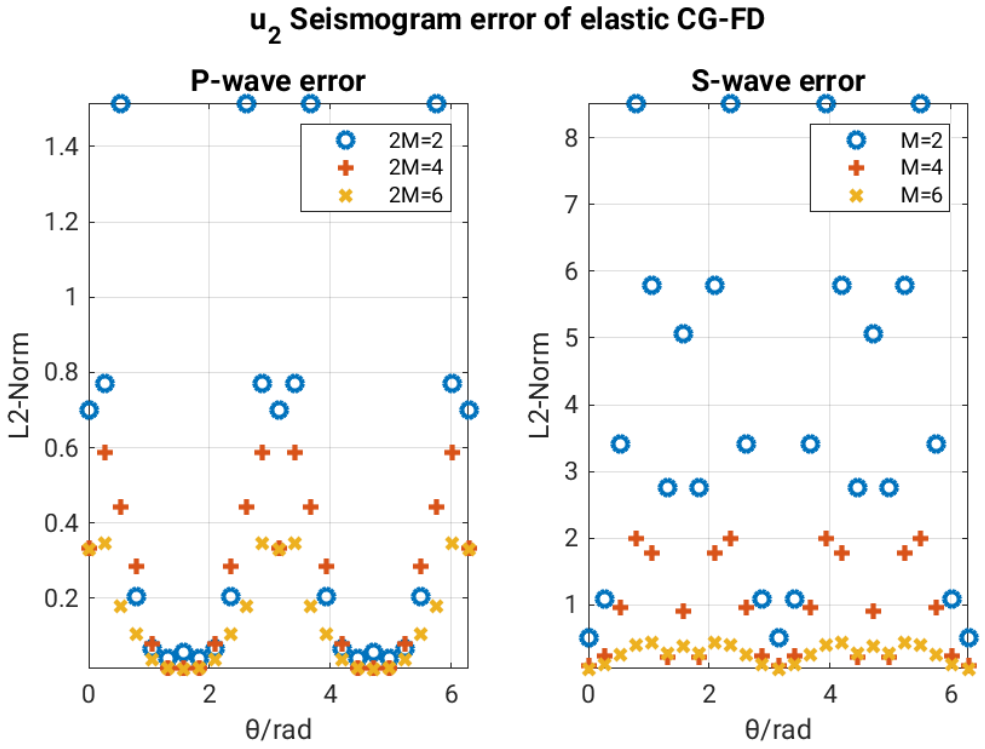

Figure 6.16: *L^2-norm error between the u_2 seismograms in elastic CG-FD and analytical solutions as a function of propagation angle. The configuration is the same as in fig. 6.15. Both the seismograms and analytical solutions are obtained from fig. 6.10.*

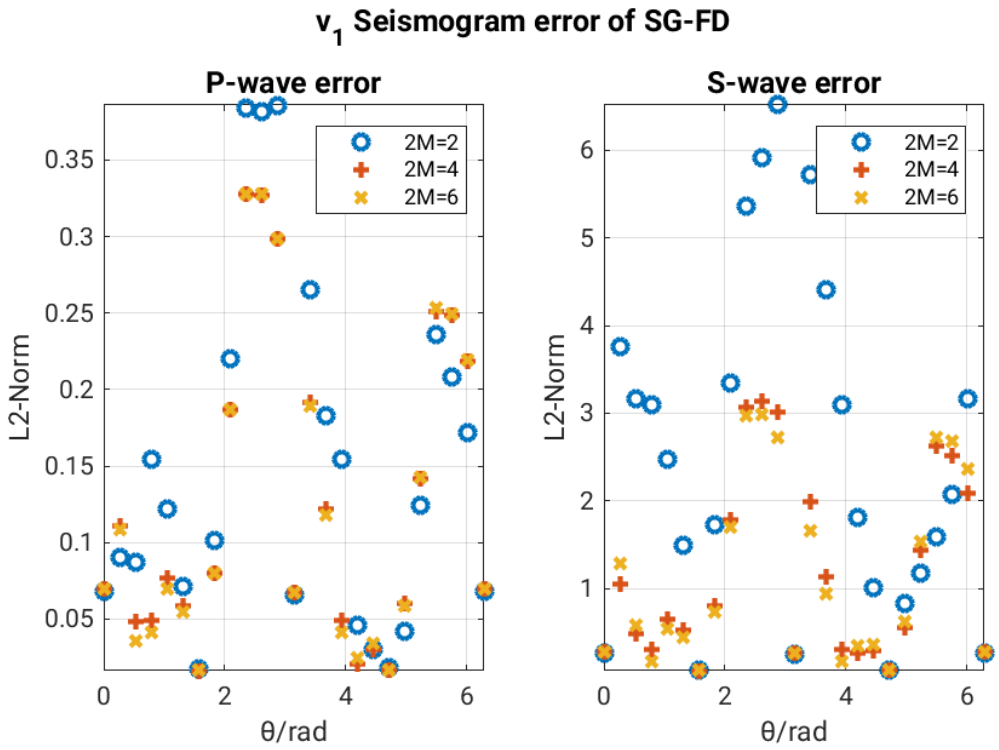

Figure 6.17: *L^2-norm error between the v_1 seismograms in elastic SG-FD and analytical solutions as a function of propagation angle. The configuration is the same as in fig. 6.15. Both the seismograms and analytical solutions are obtained from fig. 6.13.*

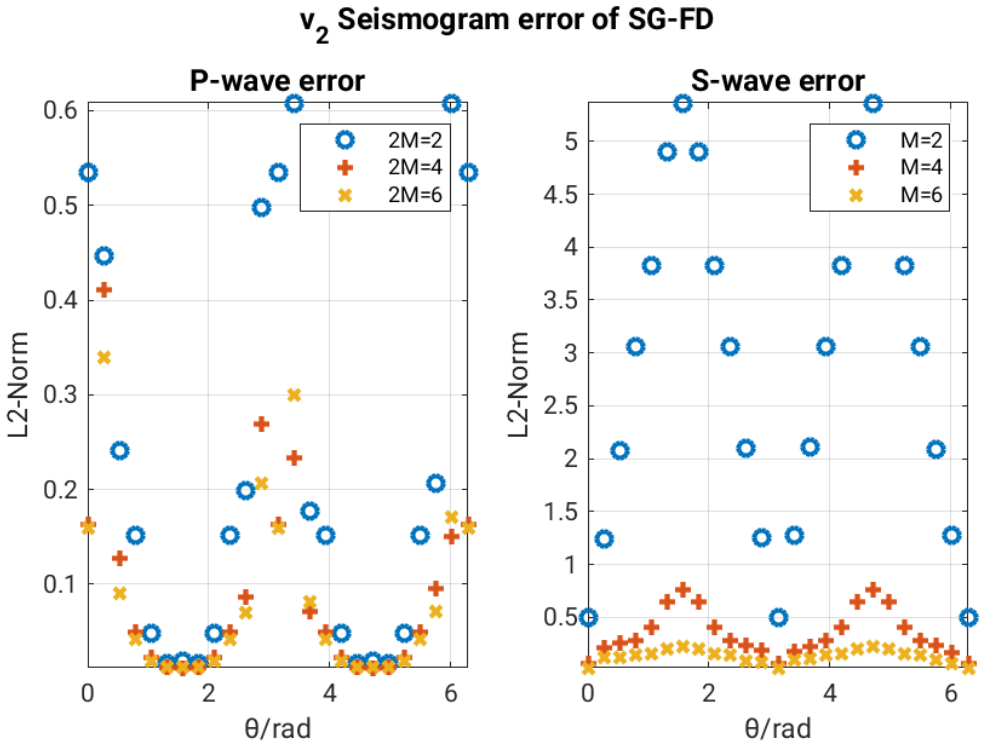

Figure 6.18: *L^2-norm error between the v_2 seismograms in elastic SG-FD and analytical solutions as a function of propagation angle. The model is homogeneous model. The configuration is the same as in fig. 6.15. Both the seismograms and analytical solutions are obtained from fig. 6.14.*

Chapter 7

Results of heterogeneous media

This chapter presents the finite-difference simulation results in heterogeneous media, including snapshots and seismograms. Unlike the homogeneous case, these results are not independently validated here; therefore, the purpose of this chapter is limited to a preliminary comparison between CG-FD and SG-FD. To facilitate direct comparison, some figures are organized in a different way from chapter 6.

7.1 Heterogeneous model

A two-layer model with homogeneous layers is used as a simple heterogeneous test model in this chapter. The model is shown in fig. 7.1. The parameters of the upper layer are the same as those of the homogeneous model in fig. 5.1. In the acoustic case, we again set $v_s = 0\,\mathrm{m/s}$.

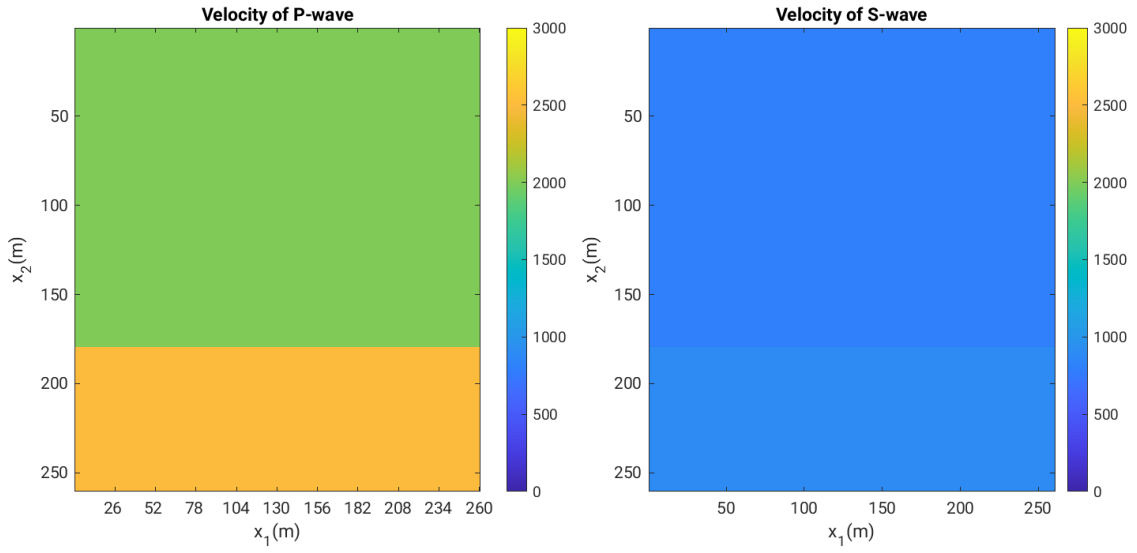

Figure 7.1: *A two-layer model with homogeneous layers. The upper layer is characterized by* $v_p = 2000.0\,\mathrm{m/s}$, $v_s = 800.0\,\mathrm{m/s}$, *and* $\rho = 2000.0\,\mathrm{kg/m^3}$, *while the lower layer is defined by* $v_p = 2500.0\,\mathrm{m/s}$, $v_s = 900.0\,\mathrm{m/s}$, *and* $\rho = 5000.0\,\mathrm{kg/m^3}$. *The interface between the two layers is located at* $x_2 = 180\,\mathrm{m}$. *This configuration serves as a simple heterogeneous model for testing.*

7.2 Acoustic FD results in heterogeneous media

Based on the acoustic wave equation of heterogeneous media, eq. 2.8, and the first-order wave equation, eq. 2.5, we perform the CG-FD and SG-FD simulations, respectively. The snapshot results of acoustic CG-FD for different spatial orders are shown in fig. 7.2, while the results of SG-FD are shown in fig. 7.3. The P-wave wavefield is clearly visible. There are no significant visible differences between the snapshots of both methods. To observe more subtle differences, we compare the seismograms recorded at the receiver locations. The seismograms is shown in fig. 7.8. Analytical solutions are not used in this chapter; to distinguish them from the results in chapter 6, the CG-FD results are plotted with blue curves.

Note that in the snapshots at $t = 0.0666\,\mathrm{s}$, the wave has already reached the grid boundaries. Therefore, in the seismogram results, some later events originate from reflections at the grid boundaries. These events are not interpreted physically here. Since no absorbing boundary conditions were applied in this thesis, such boundary reflections are numerical artifacts and should be excluded from the comparison.

Both methods reproduce the main acoustic wavefield features clearly, including the direct arrivals and the reflections from the interface. In the seismograms, the reflected waves begin to be recorded by some receivers at approximately 0.05 s. The traveltimes of both the direct and reflected arrivals agree well between CG-FD and SG-FD. At the same time, differences in normalized amplitudes can be observed. These differences mainly arise from the interface reflections and the waveforms at the receivers located near the source. Because the heterogeneous-case results are not independently validated in this thesis, these amplitude differences should be interpreted cautiously. At this stage, they should be regarded as a preliminary observation rather than a firm physical conclusion.

7.3 Elastic FD results in heterogeneous media

Based on the heterogeneous second-order elastic wave equation, eq. 2.6, and the first-order elastic wave equation, eq. 2.5, we perform the CG-FD and SG-FD simulations, respectively. Figs. 7.4 and 7.5 show the u_1 and u_2 snapshots for elastic CG-FD. Figs. 7.6 and 7.7 show the v_1 and v_2 snapshot results for elastic SG-FD.

The waveforms after $t = 0.0666\,\mathrm{s}$ exhibit opposite polarities. As discussed in the previous section, these events are not considered in this analysis. Due to the significantly larger amplitudes of the S-waves, the reflected P-waves become almost invisible after normalization. However, by cross-referencing the acoustic seismograms, the arrival times of P-wave reflections in the elastic case can be accurately identified. Although an enlarged view is not explicitly shown in this thesis, an enlarged view of these reflections reveals that the CG-FD and SG-FD results display opposite polarities. Because S-waves have higher amplitudes, further research is properly investigate this phenomenon regarding S-wave reflections. Furthermore, because the S-wave velocity is relatively low, the S-wave reflections from the interface might not have been recorded within the current time window of the seismograms; therefore, a new model or a new receiver array would need to be designed.

In summary, across both the acoustic and elastic results, the waveforms of the direct arrivals match well between the CG-FD and SG-FD methods. However, for the reflected waves, although the traveltimes are consistent, the normalized amplitudes and even the polarities exhibit noticeable differences. Consequently, no systematic conclusions regarding heterogeneous media are drawn in this chapter.

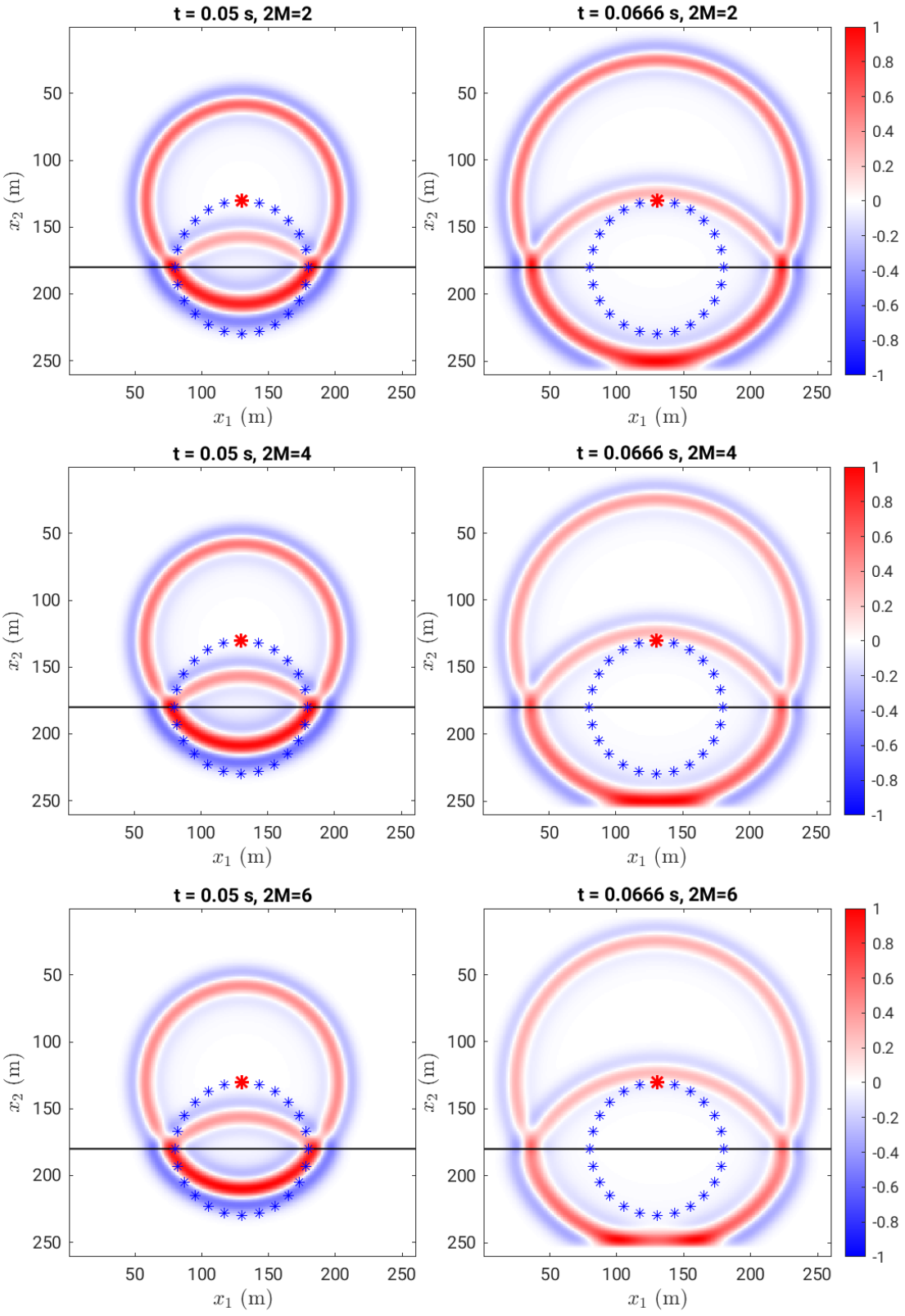

Figure 7.2: *Acoustic CG-FD pressure snapshots at* 0.05 s *(left) and* 0.0666 s *(right). The CG-FD results are of second (top), fourth (mid) and sixth (bottom) orders accuracy, respectively. The model is the heterogeneous model in fig. 7.1. Grid spacing is* $h = 1\,\mathrm{m}$ *and time interval is* $\Delta t = 0.0001\,\mathrm{s}$. *The following all snapshots use this model and grid configuration. The waveform is excited at source point (red) and spread on 2D plane, passing the receiver points (blue). The black line shows the interface between the layers.*

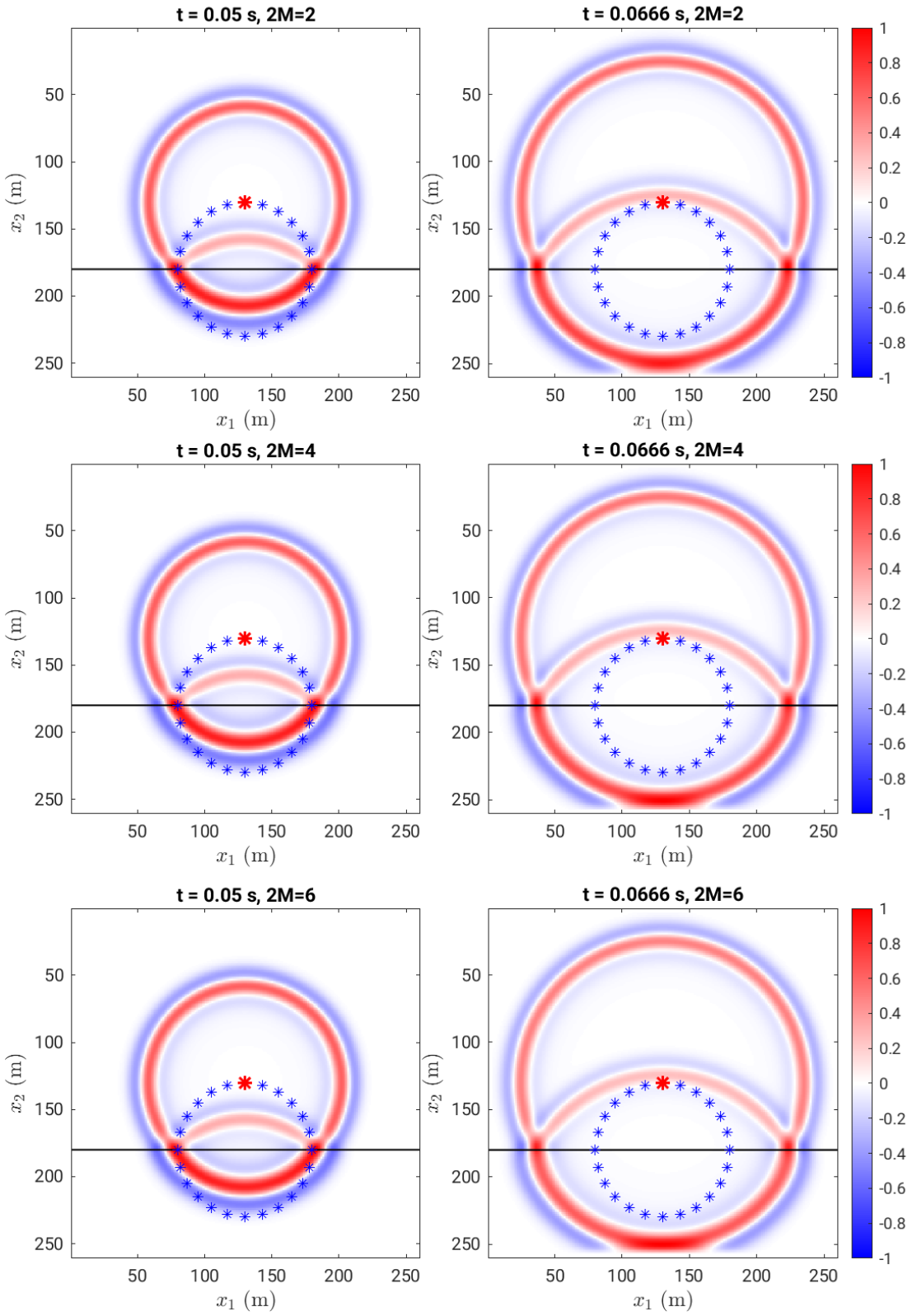

Figure 7.3: *Acoustic SG-FD pressure snapshots at* 0.05 s *(left) and* 0.0666 s *(right). The SG-FD results are of second (top), fourth (mid) and sixth (bottom) orders accuracy, respectively. The results in this figure use same configuration as CG-FD in fig. 7.2.*

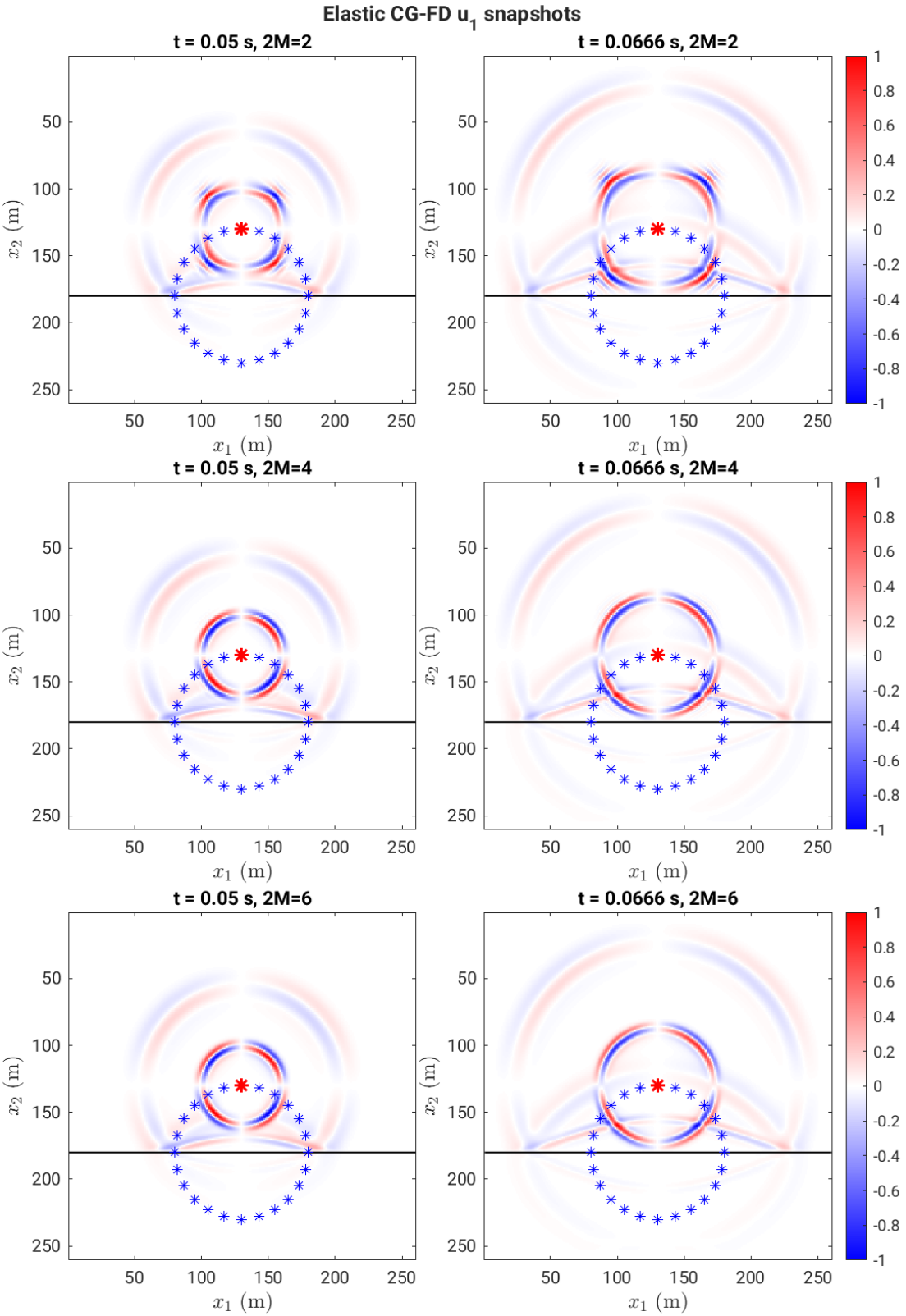

Figure 7.4: *Elastic CG-FD u_1 snapshots at* 0.05 s *(left) and* 0.0666 s *(right). The CG-FD results are of second (top), fourth (mid) and sixth (bottom) orders accuracy, respectively. The figure uses the same configuration as fig. 7.2.*

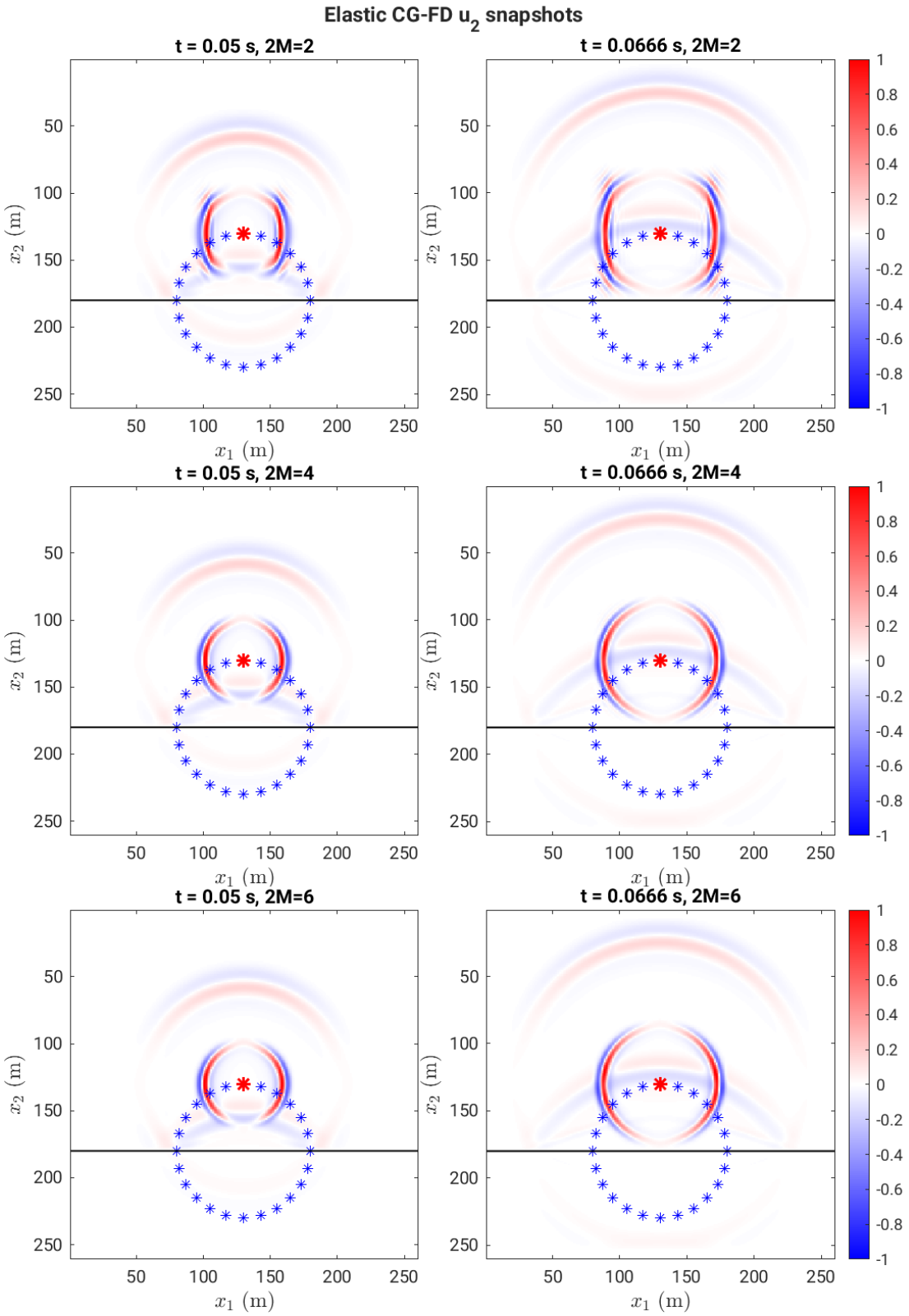

Figure 7.5: *Elastic CG-FD u_2 snapshots at* 0.05 s *(left) and* 0.0666 s *(right). The CG-FD results are of second (top), fourth (mid) and sixth (bottom) orders accuracy, respectively.*

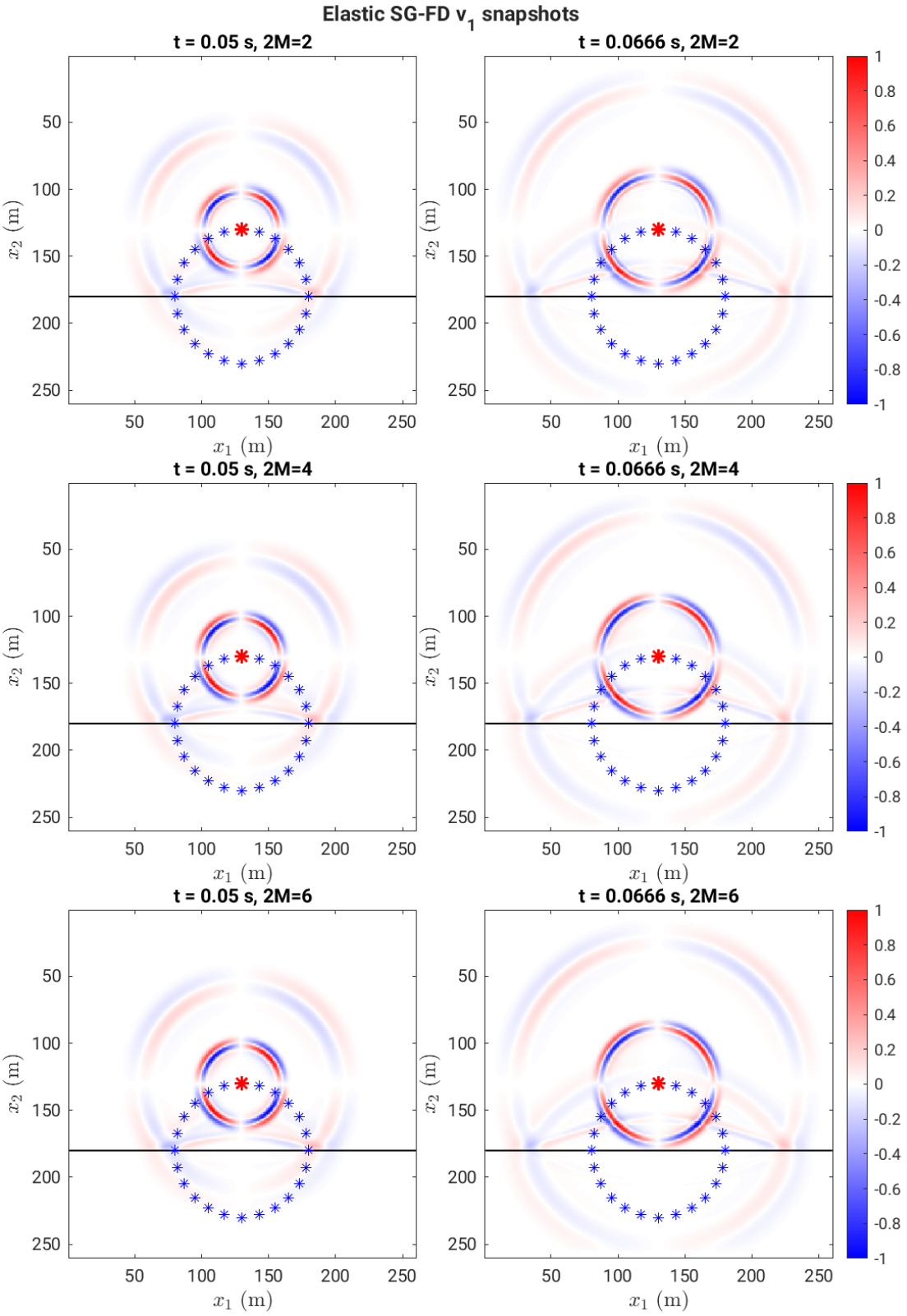

Figure 7.6: *Elastic SG-FD v_1 snapshots at* 0.05 s *(left) and* 0.0666 s *(right). The SG-FD results are of second (top), fourth (mid) and sixth (bottom) orders accuracy, respectively.*

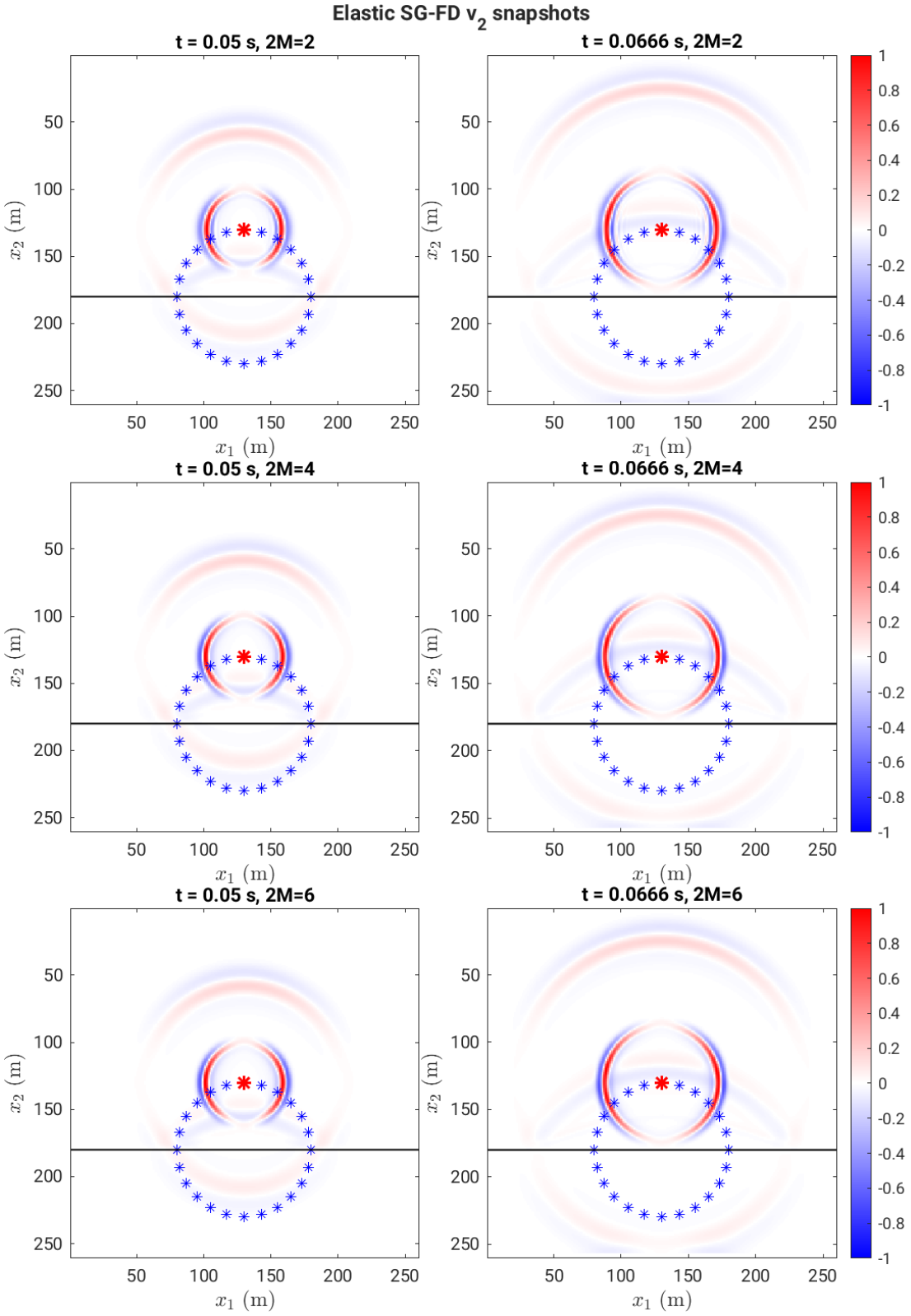

Figure 7.7: *Elastic SG-FD v_2 snapshots at* 0.05 s *(left) and* 0.0666 s *(right). The SG-FD results are of second (top), fourth (mid) and sixth (bottom) orders accuracy, respectively.*

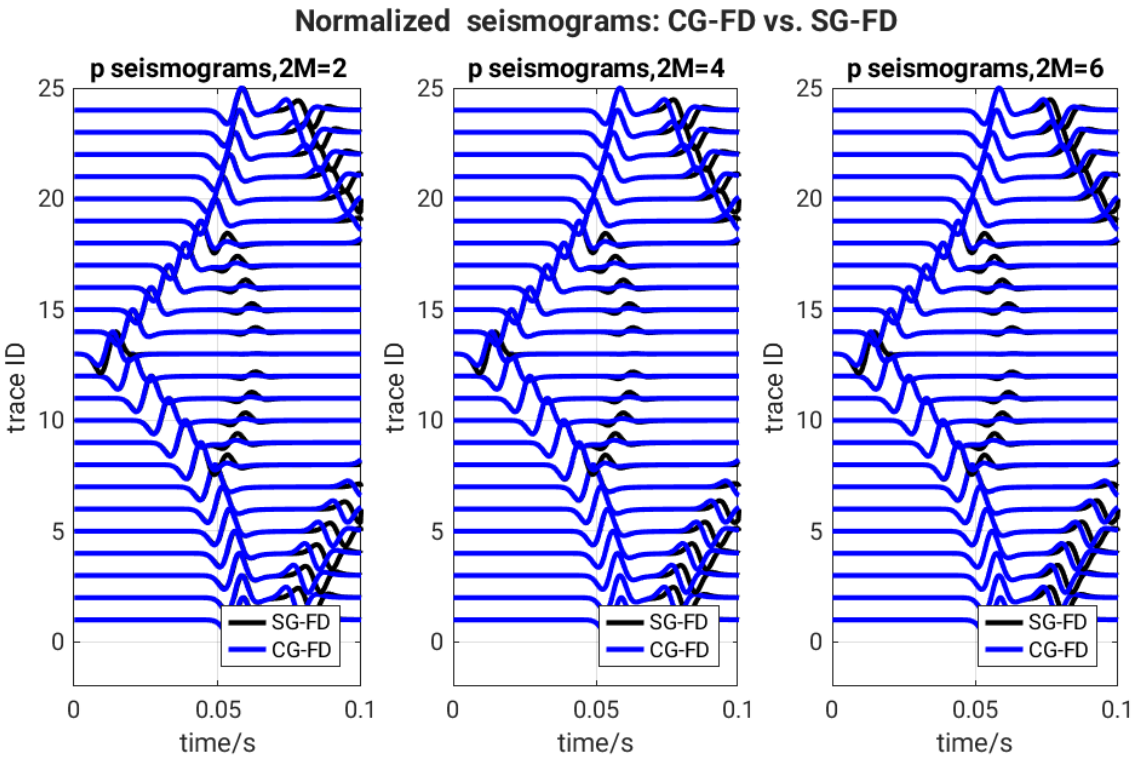

Figure 7.8: *Comparison of normalized pressure seismograms: CG-FD (blue) versus SG-FD (black). The case is acoustic case. The trace IDs correspond to the receiver array shown in fig. 7.3, starting with* 1 *at the* x_2 *positive direction (bottom receiver) and increasing in a counterclockwise direction. The vertical spacing between adjacent traces is set such that a true amplitude of* 1 *exactly spans the distance to the neighboring baseline.*

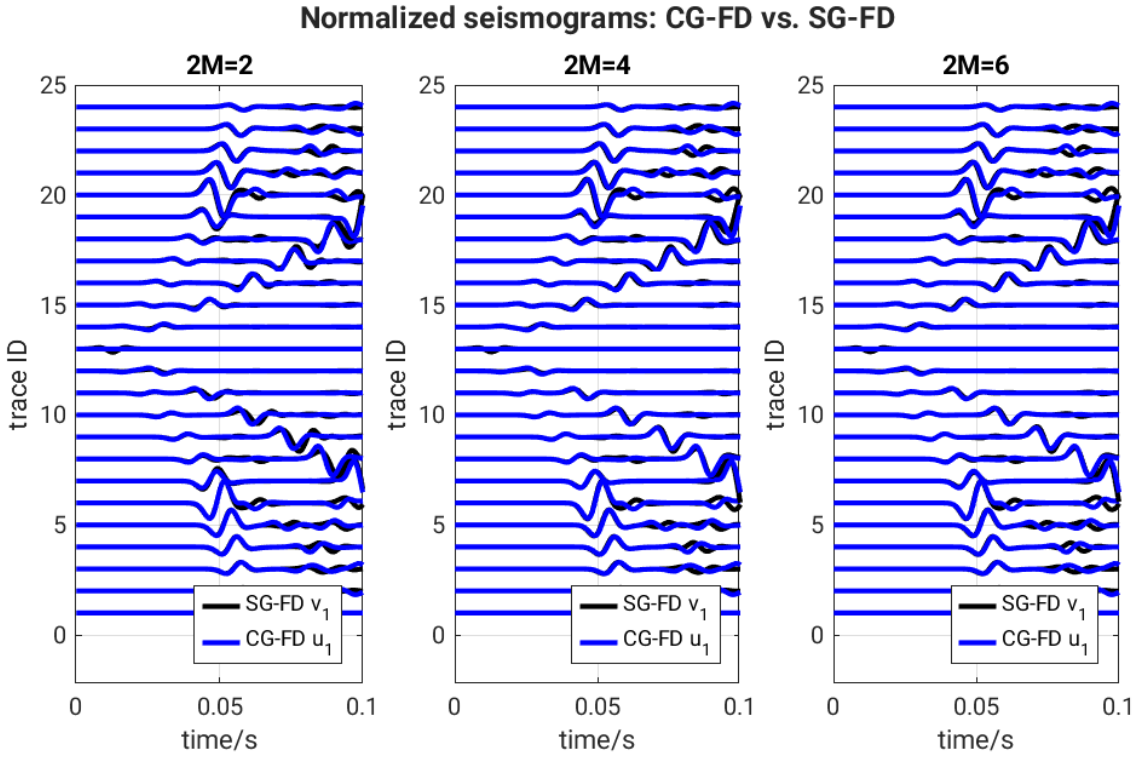

Figure 7.9: *Comparison of normalized seismograms: u_1 from elastic CG-FD (blue) versus v_1 from elastic SG-FD (black). This figure use same configuration as fig. 7.8.*

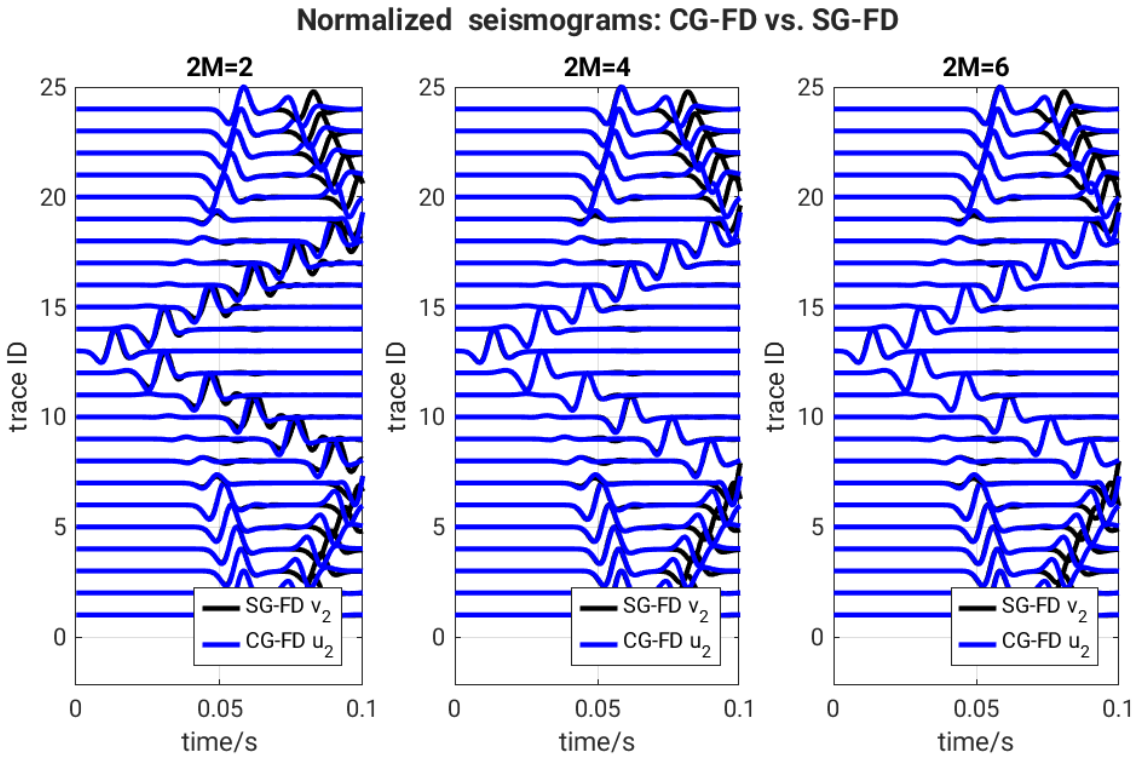

Figure 7.10: *Comparison of normalized seismograms: u_2 from elastic CG-FD (blue) versus v_2 from elastic SG-FD (black). This figure use same configuration as fig. 7.9.*

Chapter 8

Summary

This thesis develops CG-FD schemes and an SG-FD scheme for isotropic acoustic and elastic wave propagation in two dimensions, allowing arbitrary spatial accuracy orders. For CG-FD, new stability-limit expressions are derived for both the isotropic acoustic and elastic cases, and their global bounds are determined numerically by a grid scan method. These limits are verified using specifically designed test models. The resulting stability limits and numerical dispersion relations are then compared directly with those of SG-FD. Finally, both schemes are applied to homogeneous and heterogeneous models in order to compare snapshots and seismograms.

In isotropic media, the comparison between CG-FD and SG-FD must clearly distinguish between the acoustic and elastic cases. In the acoustic case, when the acoustic wave equation is used, CG-FD performs nearly as well as SG-FD in both dispersion analysis and waveform simulations. In the elastic case, CG-FD exhibits both advantages and disadvantages relative to SG-FD. Its main advantage is the less restrictive stability condition, which depends on the S-wave to P-wave velocity ratio γ. Smaller values of γ lead to larger stability limits. Its main disadvantage is stronger numerical dispersion, especially for diagonal propagation. Moreover, smaller values of γ also lead to worse dispersion. In this sense, γ affects stability and dispersion in opposite directions.

The overall conclusion is, therefore, that CG-FD can serve as a viable alternative to SG-FD in isotropic media, but it generally requires a higher spatial order to suppress dispersion to a comparable level in the elastic case. This isotropic comparison provides the necessary baseline for the investigation of more complex media.

For future work, the current code is already able to generate snapshots and seismograms in heterogeneous media, but these results still lack independent validation. In particular, the traveltimes of the main arrivals agree reasonably well, whereas the amplitudes and even polarization of the reflections differ. This indicates that the heterogeneous implementation requires further refinement and validation. Once the isotropic case has been fully consolidated, the next step should be to extend the study to anisotropic media.

CG-FD provides an alternative approach to staggered grid FD in isotropic media, which enables us to do more with anisotropic media in the future. For anisotropic media, we expect much improved accuracy and reduced runtime because no averaging of material parameters or wavefield interpolation is required.

Bibliography

Alterman, Z. and Karal Jr, F. (1968). "Propagation of elastic waves in layered media by finite difference methods". *Bulletin of the Seismological Society of America* 58.1, pp. 367–398.

Boore, D. (1972). "Finite difference methods for seismic wave propagation in heterogeneous materials". In: *Methods in Computational Physics: Advances in Research and Applications*. Vol. 11. Elsevier, pp. 1–37.

Carcione, J. M., Kosloff, D., and Kosloff, R. (1988). "Wave propagation simulation in a linear viscoelastic medium". *Geophysical Journal International* 95.3, pp. 597–611.

Cynar, S. J. (1987). "Using Gaussian elimination for computation of the central difference equation coefficients". *ACM Signum Newsletter* 22.2, pp. 12–19.

Gao, K. and Huang, L. (2017). "An improved rotated staggered-grid finite-difference method with fourth-order temporal accuracy for elastic-wave modeling in anisotropic media". *Journal of Computational Physics* 350, pp. 361–386.

Igel, H. (2017). *Computational seismology: a practical introduction*. Oxford University Press.

Kelly, K. R., Ward, R. W., Treitel, S., and Alford, R. M. (1976). "Synthetic seismograms; a finite-difference approach". *Geophysics* 41.1, pp. 2–27.

Koene, E. F., Robertsson, J. O., and Andersson, F. (2021). "Anisotropic elastic finite-difference modeling of sources and receivers on Lebedev grids". *Geophysics* 86.2, A21–A25.

Kosloff, D. D. and Baysal, E. (1982). "Forward modeling by a Fourier method". *Geophysics* 47.10, pp. 1402–1412.

Lay, T. and Wallace, T. C. (1995). *Modern global seismology*. Vol. 58. Elsevier.

Levander, A. R. (1988). "Fourth-order finite-difference P-SV seismograms". *Geophysics* 53.11, pp. 1425–1436.

Lines, L. R., Slawinski, R., and Bording, R. P. (1999). "A recipe for stability of finite-difference wave-equation computations". *Geophysics* 64.3, pp. 967–969.

Lisitsa, V. and Vishnevskiy, D. (2010). "Lebedev scheme for the numerical simulation of wave propagation in 3D anisotropic elasticity". *Geophysical Prospecting* 58.4, pp. 619–635.

Liu, Y. and Sen, M. K. (2011). "Scalar wave equation modeling with time–space domain dispersion-relation-based staggered-grid finite-difference schemes". *Bulletin of the Seismological Society of America* 101.1, pp. 141–159.

Mai, D. (Sept. 2024). “3D anisotropic Finite-Difference modelling on the standard staggered grid”. Master’s thesis. Karlsruhe, Germany: Karlsruhe Institute of Technology (KIT), Geophysical Institute (GPI).

Marfurt, K. J. (1984). “Accuracy of finite-difference and finite-element modeling of the scalar and elastic wave equations”. *Geophysics* 49.5, pp. 533–549.

Moczo, P., Kristek, J., and Halada, L. (2000). “3D fourth-order staggered-grid finite-difference schemes: Stability and grid dispersion”. *Bulletin of the Seismological Society of America* 90.3, pp. 587–603.

Moczo, P., Robertsson, J. O., and Eisner, L. (2007). “The finite-difference time-domain method for modeling of seismic wave propagation”. *Advances in geophysics* 48, pp. 421–516.

Morse, P. M. and Feshbach, H. (1946). *Methods of theoretical physics*. Technology Press.

Saenger, E. H. and Bohlen, T. (2004). “Finite-difference modeling of viscoelastic and anisotropic wave propagation using the rotated staggered grid”. *Geophysics* 69.2, pp. 583–591.

Saenger, E. H., Gold, N., and Shapiro, S. A. (2000). “Modeling the propagation of elastic waves using a modified finite-difference grid”. *Wave motion* 31.1, pp. 77–92.

Shi, Z. (2026). *Zuoyi’s Master Thesis Code*. https://github.com/ZuoyiShi2487089/Zuoyi-s-Master-thesis-code.git. GitHub repository, accessed: March 27, 2026.

Tan, S. and Huang, L. (2014). “A staggered-grid finite-difference scheme optimized in the time–space domain for modeling scalar-wave propagation in geophysical problems”. *Journal of Computational Physics* 276, pp. 613–634.

Tarantola, A. (1984). “Inversion of seismic reflection data in the acoustic approximation”. *Geophysics* 49.8, pp. 1259–1266.

Virieux, J. (1984). “SH-wave propagation in heterogeneous media: Velocity-stress finite-difference method”. *Exploration Geophysics* 15.4, pp. 265–265.

Virieux, J. (1986). “P-SV wave propagation in heterogeneous media: Velocity-stress finite-difference method”. *Geophysics* 51.4, pp. 889–901.

Appendix A

Derivation of 2D Elastic Wave Equation in Heterogeneous Media

We combine the equation of motion and the isotropic stress–strain relation to obtain the second order elastic wave equation. By substituting eq. 2.4 into eq. 2.1, the three-dimensional (3D) elastic wave equation for isotropic media is written as

$$\begin{aligned}\rho\frac{\partial^2 u_i}{\partial t^2} &= \frac{\partial}{\partial x_j}\left(\lambda\theta\delta_{ij}\right) + \frac{\partial}{\partial x_j}\left(2\mu\epsilon_{ij}\right) + f_i \\ &= \frac{\partial}{\partial x_j}\left[\lambda\left(\frac{\partial u_1}{\partial x_1} + \frac{\partial u_2}{\partial x_2} + \frac{\partial u_3}{\partial x_3}\right)\delta_{ij}\right] + \frac{\partial}{\partial x_j}\left[\mu\left(\frac{\partial u_i}{\partial x_j} + \frac{\partial u_j}{\partial x_i}\right)\right] + f_i,\end{aligned} \tag{A.1}$$

For the two-dimensional(2D) x_1–x_2 case ($i, j = 1, 2$) in heterogeneous isotropic media, eq. A.1 changes to

$$\begin{aligned}\rho_{x_1,x_2}\frac{\partial^2 u_1}{\partial t^2} &= \frac{\partial}{\partial x_j}\Big[\lambda_{x_1,x_2}\left(\frac{\partial u_1}{\partial x_1} + \frac{\partial u_2}{\partial x_2}\right)\delta_{1j}\Big] + \frac{\partial}{\partial x_j}\Big[\mu_{x_1,x_2}\left(\frac{\partial u_1}{\partial x_j} + \frac{\partial u_j}{\partial x_1}\right)\Big] + f_1, \\ \rho_{x_1,x_2}\frac{\partial^2 u_2}{\partial t^2} &= \frac{\partial}{\partial x_j}\Big[\lambda_{x_1,x_2}\left(\frac{\partial u_1}{\partial x_1} + \frac{\partial u_2}{\partial x_2}\right)\delta_{2j}\Big] + \frac{\partial}{\partial x_j}\Big[\mu_{x_1,x_2}\left(\frac{\partial u_2}{\partial x_j} + \frac{\partial u_j}{\partial x_2}\right)\Big] + f_2.\end{aligned} \tag{A.2}$$

Expanding all terms gives the 2D elastic wave equation:

$$\begin{aligned}\rho\frac{\partial^2 u_1}{\partial t^2} &= (\lambda+2\mu)\frac{\partial^2 u_1}{\partial x_1^2} + \mu\frac{\partial^2 u_1}{\partial x_2^2} + (\lambda+\mu)\frac{\partial^2 u_2}{\partial x_1 \partial x_2} \\ &\quad + \frac{\partial\lambda}{\partial x_1}\left(\frac{\partial u_1}{\partial x_1} + \frac{\partial u_2}{\partial x_2}\right) + 2\frac{\partial\mu}{\partial x_1}\frac{\partial u_1}{\partial x_1} + \frac{\partial\mu}{\partial x_2}\left(\frac{\partial u_1}{\partial x_2} + \frac{\partial u_2}{\partial x_1}\right) + f_1, \\ \rho\frac{\partial^2 u_2}{\partial t^2} &= (\lambda+2\mu)\frac{\partial^2 u_2}{\partial x_2^2} + \mu\frac{\partial^2 u_2}{\partial x_1^2} + (\lambda+\mu)\frac{\partial^2 u_1}{\partial x_1 \partial x_2} \\ &\quad + \frac{\partial\lambda}{\partial x_2}\left(\frac{\partial u_1}{\partial x_1} + \frac{\partial u_2}{\partial x_2}\right) + 2\frac{\partial\mu}{\partial x_2}\frac{\partial u_2}{\partial x_2} + \frac{\partial\mu}{\partial x_1}\left(\frac{\partial u_1}{\partial x_2} + \frac{\partial u_2}{\partial x_1}\right) + f_2,\end{aligned} \tag{A.3}$$

where λ_{x_1,x_2} and μ_{x_1,x_2} are the spatially dependent Lamé parameters; ρ_{x_1,x_2} is the density; u_1 and u_2 are particle displacement components; f_1 and f_2 are body force components.

Appendix B

Derivation of Stability Limit & Dispersion Relation of CG-FD for Homogeneous Media

B.1 Stability and dispersion relation of CG-FD method on elastic wave equation for homogeneous media

Consider a plane wave of the form

$$u = Ue^{i(-\omega t + k_1 x_1 + k_2 x_2)}. \tag{B.1}$$

Then we have

$$\begin{aligned} u_1 &= U_1 e^{i(-\omega t + k_1 x_1 + k_2 x_2)}, \\ u_2 &= U_2 e^{i(-\omega t + k_1 x_1 + k_2 x_2)}. \end{aligned} \tag{B.2}$$

Here, $k_1 = k\sin\theta$, $k_2 = k\cos\theta$, where θ is the angle between the wave propagation direction and the x_2-axis. The Courant numbers are $r_p = \alpha\Delta t/h$ and $r_s = \beta\Delta t/h$. Inserting the plane wave into the update formula (eq. 3.19) gives

$$\begin{aligned} U_1(e^{i\omega\Delta t} + e^{-i\omega\Delta t} - 2) &= r_p^2 U_1 \sum_{m=1}^{M} a_m (e^{imkh\sin\theta} + e^{-imkh\sin\theta} - 2) \\ &\quad + r_s^2 U_1 \sum_{m=1}^{M} a_m (e^{imkh\cos\theta} + e^{-imkh\cos\theta} - 2), \\ &\quad + \frac{(r_p^2 - r_s^2)U_2}{4} \sum_{m=1}^{M} b_m \sum_{l=1}^{M} b_l (e^{i(m\sin\theta + l\cos\theta)kh} + e^{-i(m\sin\theta + l\cos\theta)kh} \\ &\quad - e^{-i(m\sin\theta - l\cos\theta)kh} - e^{i(m\sin\theta - l\cos\theta)kh}) \\ U_2(e^{i\omega\Delta t} + e^{-i\omega\Delta t} - 2) &= r_p^2 U_2 \sum_{m=1}^{M} a_m (e^{imkh\cos\theta} + e^{-imkh\cos\theta} - 2) \\ &\quad + r_s^2 U_2 \sum_{m=1}^{M} a_m (e^{imkh\sin\theta} + e^{-imkh\sin\theta} - 2) \\ &\quad + \frac{(r_p^2 - r_s^2)U_1}{4} \sum_{m=1}^{M} b_m \sum_{l=1}^{M} b_l (e^{i(m\sin\theta + l\cos\theta)kh} + e^{-i(m\sin\theta + l\cos\theta)kh} \\ &\quad - e^{-i(m\sin\theta - l\cos\theta)kh} - e^{i(m\sin\theta - l\cos\theta)kh}). \end{aligned}$$

Using Euler's formula $e^{i\theta} = \cos\theta + i\sin\theta$, the above can be simplified to

$$\begin{aligned}
U_1[2\cos(\omega\Delta t) - 2] &= r_p^2 U_1 \sum_{m=1}^{M} a_m[2\cos(mk_1h) - 2] + r_s^2 U_1 \sum_{m=1}^{M} a_m[2\cos(mk_2h) - 2] \\
&\quad + (r_p^2 - r_s^2)U_2 \sum_{m=1}^{M} b_m \sum_{l=1}^{M} b_l[2\cos(mk_1h + lk_2h) - 2\cos(mk_1h - lk_2h)]/4, \\
U_2[2\cos(\omega\Delta t) - 2] &= r_p^2 U_2 \sum_{m=1}^{M} a_m[2\cos(mk_2h) - 2] + r_s^2 U_2 \sum_{m=1}^{M} a_m[2\cos(mk_1h) - 2] \\
&\quad + (r_p^2 - r_s^2)U_1 \sum_{m=1}^{M} b_m \sum_{l=1}^{M} b_l[2\cos(mk_1h + lk_2h) - 2\cos(mk_1h - lk_2h)]/4.
\end{aligned} \tag{B.3}$$

Using the identities $2\cos\theta - 2 = -4\sin^2(\theta/2)$ and $\cos(\theta_1 \pm \theta_2) = \cos\theta_1\cos\theta_2 \mp \sin\theta_1\sin\theta_2$, we can obtain:

$$\begin{aligned}
U_1 \sin^2\frac{\omega\Delta t}{2} &= r_p^2 U_1 \sum_{m=1}^{M} a_m \sin^2\frac{mk_1h}{2} + (r_p^2 - r_s^2)U_2 \sum_{m=1}^{M} b_m \sum_{l=1}^{M} b_l \frac{\sin(mk_1h)\sin(lk_2h)}{4} \\
&\quad + r_s^2 U_1 \sum_{m=1}^{M} a_m \sin^2\frac{mk_2h}{2}, \\
U_2 \sin^2\frac{\omega\Delta t}{2} &= r_p^2 U_2 \sum_{m=1}^{M} a_m \sin^2\frac{mk_2h}{2} + (r_p^2 - r_s^2)U_1 \sum_{m=1}^{M} b_m \sum_{l=1}^{M} b_l \frac{\sin(mk_1h)\sin(lk_2h)}{4} \\
&\quad + r_s^2 U_2 \sum_{m=1}^{M} a_m \sin^2\frac{mk_1h}{2}.
\end{aligned} \tag{B.4}$$

To simplify the equation, we first define the discretization operators:

$$\begin{aligned}
S_t &= \sin^2\frac{\omega\Delta t}{2}, \\
S_{12} &= \sum_{m=1}^{M} b_m \sum_{l=1}^{M} b_l \frac{\sin(mk_1h)\sin(lk_2h)}{4}, \\
S_{11} &= \sum_{m=1}^{M} a_m \sin^2\frac{mk_1h}{2}, \\
S_{22} &= \sum_{m=1}^{M} a_m \sin^2\frac{mk_2h}{2}.
\end{aligned} \tag{B.5}$$

Then we define

$$\begin{aligned}
A &= r_p^2 A' = r_p^2 S_{11} + r_p^2\gamma^2 S_{22}, \\
D &= r_p^2 D' = r_p^2 S_{22} + r_p^2\gamma^2 S_{11}, \\
B &= r_p^2 B' = r_p^2(1 - \gamma^2)S_{12},
\end{aligned} \tag{B.6}$$

where $\gamma = \beta/\alpha$, i.e., $r_s = \gamma r_p$. Furthermore, we define

$$C_1 = S_t - A, \quad C_2 = C_3 = -B, \quad C_4 = S_t - D. \tag{B.7}$$

Then eq. B.4 can be written as

$$\begin{bmatrix} C_1 & C_2 \\ C_3 & C_4 \end{bmatrix} \begin{bmatrix} U_1 \\ U_2 \end{bmatrix} = 0. \tag{B.8}$$

For nonzero solutions of U_1 and U_2, the determinant must vanish, i.e., $C_1C_4 - C_2C_3 = 0$. We obtain:

$$(S_t - A)(S_t - D) - B^2 = 0. \tag{B.9}$$

Solving the quadratic equation for S_t gives

$$S_t = \frac{(A + D) \pm \sqrt{(A - D)^2 + 4B^2}}{2}. \tag{B.10}$$

Stability requires $S_t \leq 1$ for both solutions, i.e.,

$$r_p \leq r_{\max} = \sqrt{\frac{2}{(1+\gamma^2)(S_{11} + S_{22}) + (1-\gamma^2)\sqrt{(S_{11} - S_{22})^2 + 4S_{12}^2}}}, \tag{B.11}$$

where $r_{\max}$ is the stability limit for arbitrary order accuracy. When $M = 1$, eq. B.11 reduces to (Marfurt, 1984)

$$r_{\max} = \frac{1}{\sqrt{1+\gamma^2}}, \tag{B.12}$$

For the results of higher-orders accuracy, the verification of eq. B.11 is mentioned in Section 5.2.

From eq. B.10, the numerical dispersion relation is

$$\frac{c_{\text{fd}}}{c} = \frac{\omega \Delta t}{khr_p} = \frac{2}{khr_p} \arcsin\left(r_p \sqrt{\frac{1+\gamma^2}{2}(S_{11} + S_{22}) + \frac{1-\gamma^2}{2}\sqrt{(S_{11} - S_{22})^2 + 4S_{12}^2}} \right) \tag{B.13}$$

or

$$\frac{c_{\text{fd}}}{c} = \frac{\omega \Delta t}{khr_s} = \frac{2}{khr_s} \arcsin\left(r_p \sqrt{\frac{1+\gamma^2}{2}(S_{11} + S_{22}) - \frac{1-\gamma^2}{2}\sqrt{(S_{11} - S_{22})^2 + 4S_{12}^2}} \right). \tag{B.14}$$

B.2 Stability and dispersion relation of CG-FD method on acoustic wave equation

B.2.1 Derivation of stability limit and dispersion relation

Consider a harmonic plane wave of the form

$$p = p_0 e^{i(-\omega t + kx_1 \sin\theta + kx_2 \cos\theta)}. \tag{B.15}$$

Inserting this plane wave into the update formula 3.21 gives

$$\begin{aligned} e^{i\omega\Delta t} + e^{-i\omega\Delta t} - 2 = r^2 \Bigg(& \sum_{m=1}^{M} a_m (e^{ikmh\sin\theta} + e^{-ikmh\sin\theta} - 2) \\ & + \sum_{m=1}^{M} a_m (e^{ikmh\cos\theta} + e^{-ikmh\cos\theta} - 2) \Bigg). \end{aligned} \tag{B.16}$$

Using Euler's formula $e^{i\theta} = \cos\theta + i\sin\theta$, the above simplifies to

$$2\cos(\omega\Delta t) - 2 = r^2 \sum_{m=1}^{M} a_m [2\cos(mkh\sin\theta) - 2] + r^2 \sum_{m=1}^{M} a_m [2\cos(mkh\cos\theta) - 2]. \tag{B.17}$$

Using the trigonometric identity $2\cos\theta - 2 = -4\sin^2(\theta/2)$, we obtain

$$\sin^2\left(\frac{\omega\Delta t}{2}\right) = r^2 \sum_{m=1}^{M} a_m \left[\sin^2\left(\frac{mkh\sin\theta}{2}\right) + \sin^2\left(\frac{mkh\cos\theta}{2}\right)\right]. \tag{B.18}$$

The numerical dispersion relation for the 2D FD scheme for acoustic case is

$$\frac{c_{\mathrm{fd}}}{c} = \frac{\omega\Delta t}{khr} = \frac{2}{khr}\arcsin\left[r\sqrt{\sum_{m=1}^{M} a_m \left[\sin^2\left(\frac{mkh\sin\theta}{2}\right) + \sin^2\left(\frac{mkh\cos\theta}{2}\right)\right]}\right]. \tag{B.19}$$

The stability limit requires $\sin^2(\omega\Delta t/2) \leq 1$, which gives

$$r \leq r_{\max} = \frac{1}{\sqrt{\sum_{m=1}^{M} a_m \left[\sin^2\left(\frac{mkh\sin\theta}{2}\right) + \sin^2\left(\frac{mkh\cos\theta}{2}\right)\right]}}, \tag{B.20}$$

where $r_{\max}$ represents the stability limit of CG-FD for acoustic case. In eq. B.20, the point where $r_{\max}$ is minimum is not fixed. Therefore, we should apply the grid scan method to find its global minimum.

B.2.2 Discussion of different stability limit expressions

For practical implementations, Lines et al. (1999) derived a generalized, strictly conservative stability limit based on the sum of the absolute values of the spatial difference weights. For the 2D case, a sufficient condition for stability is

$$r_{\max} = \frac{1}{\sqrt{\sum_{m=1}^{M} |a_m| + \left|\sum_{m=1}^{M} a_m\right|}}, \tag{B.21}$$

which is obtained from standard von Neumann stability analysis. We use a grid scan method in programming to find the global limit. Although the limit result of eq. B.20 is higher than the result of eq. B.21, their results are very close. This slight difference occurs because the conservative formula assumes all finite-difference terms can simultaneously reach their maximum values. It also ignores the cancellation effect caused by the alternating signs of the high-order coefficients. Despite this minor difference, the two limits are highly consistent. This verifies that our derived limit aligns with classical stability criteria, while removing the unnecessary conservative margin introduced by the absolute value inequality.

Furthermore, we calculate the mathematical relationship between eq. B.20 and B.21. Based on the trigonometric function relationship, which is $\sin^2\alpha = (1-\cos 2\alpha)/2$, eq. B.20 can be rewritten as

$$r \leq r_{\max} = \frac{1}{\sqrt{\sum_{m=1}^{M} a_m \left(1 - \frac{\cos(mkh\sin\theta)}{2} - \frac{\cos(mkh\cos\theta)}{2}\right)}}. \tag{B.22}$$

It is obvious that

$$\begin{aligned} &\sum_{m=1}^{M} a_m \leq \left|\sum_{m=1}^{M} a_m\right|, \\ &\sum_{m=1}^{M} a_m \left(-\frac{\cos(mkh\sin\theta)}{2} - \frac{\cos(mkh\cos\theta)}{2}\right) \leq \sum_{m=1}^{M} |a_m|, \end{aligned} \tag{B.23}$$

which constitutes the core conservative practice in conventional analysis.

Appendix C

Derivation of Stability Limit & Dispersion Relation of SG-FD

The derivation begins with the 2D first order elastic wave equations (eq. 2.5). The procedure for deriving the dispersion relation follows the analysis framework outlined by Liu and Sen (2011). Based on this framework, we derive the stability limit. To begin the analysis, we discretize all the spatial and temporal derivatives in the elastic wave equations as follows:

$$
\begin{aligned}
\frac{\partial v_1(i,j,n)}{\partial t} &\approx \frac{v_1^{n+1}[i,j] - v_1^n[i,j]}{\Delta t}, \\
\frac{\partial \sigma_{11}(i,j,n)}{\partial x_1} &\approx \frac{1}{h}\sum_{m=1}^{M} \beta_m(\sigma_{11}^{n+}[i^- + m, j] - \sigma_{11}^{n+}[i^+ - m, j]), \\
\frac{\partial \sigma_{12}(i,j,n)}{\partial x_2} &\approx \frac{1}{h}\sum_{m=1}^{M} \beta_m(\sigma_{12}^{n+}[i, j^- + m] - \sigma_{12}^{n+}[i, j^+ - m]), \\
\frac{\partial v_2(i,j,n)}{\partial t} &\approx \frac{v_2^{n+1}[i^+,j^+] - v_2^n[i^+,j^+]}{\Delta t}, \\
\frac{\partial \sigma_{12}(i,j,n)}{\partial x_1} &\approx \frac{1}{h}\sum_{m=1}^{M} \beta_m(\sigma_{12}^{n+}[i + m, j^+] - \sigma_{12}^{n+}[i - m + 1, j^+]), \\
\frac{\partial \sigma_{22}(i,j,n)}{\partial x_2} &\approx \frac{1}{h}\sum_{m=1}^{M} \beta_m(\sigma_{22}^{n+}[i^+, j + m] - \sigma_{22}^{n+}[i^+, j - m + 1]), \\
\frac{\partial \sigma_{11}(i,j,n)}{\partial t} &\approx \frac{\sigma_{11}^{n+}[i^+,j] - \sigma_{11}^{n-}[i^+,j]}{\Delta t}, \\
\frac{\partial v_1(i,j,n)}{\partial x_1} &\approx \frac{1}{h}\sum_{m=1}^{M} \beta_m(v_1^{n}[i + m, j] - v_1^{n}[i - m + 1, j]), \\
\frac{\partial v_2(i,j,n)}{\partial x_2} &\approx \frac{1}{h}\sum_{m=1}^{M} \beta_m(v_2^{n}[i^+, j^- + m] - v_2^{n}[i^+, j^+ - m]).
\end{aligned}
\tag{C.1}
$$

Plane wave at staggered grid points:

$$\begin{aligned} v_1^n[m,j] &= Ae^{i(k_1(x+mh)+k_2(y+jh)-\omega(t+n\Delta t))}, \\ v_2^n[m^+,j^+] &= Ce^{i(k_1(x+mh+0.5h)+k_2(y+jh+0.5h)-\omega(t+n\Delta t))}, \\ \sigma_{11}^{n+}[m^+,j] &= De^{i(k_1(x+mh+0.5h)+k_2(y+jh)-\omega(t+n\Delta t+0.5\Delta t))}, \\ \sigma_{12}^{n+}[m,j^+] &= Ee^{i(k_1(x+mh)+k_2(y+jh+0.5h)-\omega(t+n\Delta t+0.5\Delta t))}, \\ \sigma_{22}^{n+}[m^+,j] &= Fe^{i(k_1(x+mh+0.5h)+k_2(y+jh)-\omega(t+n\Delta t+0.5\Delta t))}. \end{aligned} \tag{C.2}$$

Substituting eq. C.2 into elastic wave equations (eq. 2.5), we obtain

$$\begin{aligned} gA &\approx bf_1D + bf_2E, \\ gC &\approx bf_1E + bf_2F, \\ gD &\approx (\lambda+2\mu)f_1A + \lambda f_2C, \\ gF &\approx \lambda f_1A + (\lambda+2\mu)f_2C, \\ gE &\approx \mu f_2A + \mu f_1C, \end{aligned} \tag{C.3}$$

with $b = 1/\rho$ and

$$\begin{aligned} g &= -\sin(\omega\Delta t/2), \\ f_1 &= \frac{\Delta t}{h}\sum_{m=1}^{M}\beta_m \sin((m-0.5)k_1h), \\ f_2 &= \frac{\Delta t}{h}\sum_{m=1}^{M}\beta_m \sin((m-0.5)k_2h). \end{aligned} \tag{C.4}$$

Eliminating E, D, F gives

$$E \approx \frac{\mu f_2A + \mu f_1C}{g}, \quad D \approx \frac{gA - bf_2E}{bf_1}, \quad F \approx \frac{gC - bf_1E}{bf_2}. \tag{C.5}$$

Homogeneous system for A, C:

$$\begin{bmatrix} g^2 - b(\lambda+2\mu)f_1^2 - b\mu f_2^2 & -b(\lambda+\mu)f_1f_2 \\ b(\lambda+\mu)f_1f_2 & g^2 - b\mu f_1^2 - b(\lambda+2\mu)f_2^2 \end{bmatrix} \begin{bmatrix} A \\ C \end{bmatrix} \approx 0. \tag{C.6}$$

Solving gives

$$g^2 \approx \alpha^2(f_1^2+f_2^2), \quad \text{or} \quad g^2 \approx \beta^2(f_1^2+f_2^2), \tag{C.7}$$

with $\alpha^2 = b(\lambda+2\mu)$, $\beta^2 = b\mu$.

Stability requires $g^2 \leq 1$, i.e.,

$$r \leq r_{\max} = \frac{1}{\sqrt{\left(\sum_{m=1}^{M}\beta_m \sin((m-0.5)k_1h)\right)^2 + \left(\sum_{m=1}^{M}\beta_m \sin((m-0.5)k_2h)\right)^2}}. \tag{C.8}$$

Numerical inspection shows that the minimum $r_{\max}$ is attained at $kh = \sqrt{2}\pi$, $\theta = n\pi/4$ with $n = 1, 3, 5, 7$. Therefore, eq. C.8 can be simplified as

$$r_{\max} = \frac{1}{\sqrt{2}\sum_{m=1}^{M}|\beta_m|}. \tag{C.9}$$

Substituting eq. C.4 into the solutions (eq. C.7), we obtain

$$\left(\sum_{m=1}^{M}\beta_m \sin((m-0.5)k_1h)\right)^2+\left(\sum_{m=1}^{M}\beta_m \sin((m-0.5)k_2h)\right)^2 \approx \frac{\sin^2(0.5w\Delta t)}{r_p^2}, \quad \text{(C.10)}$$

or

$$\left(\sum_{m=1}^{M}\beta_m \sin((m-0.5)k_1h)\right)^2+\left(\sum_{m=1}^{M}\beta_m \sin((m-0.5)k_2h)\right)^2 \approx \frac{\sin^2(0.5w\Delta t)}{r_s^2}, \quad \text{(C.11)}$$

where $r_p = \alpha\Delta t/h$ and $r_s = \beta\Delta t/h$. From eq. C.10 and C.11, we obtain the dispersion relation as

$$\begin{aligned}\frac{c_{\mathrm{fd}}}{c} &= \frac{w\Delta t}{khr_p}\\ &\approx \frac{2}{khr_p}\arcsin\sqrt{r_p^2\left[\left(\sum_{m=1}^{M}\beta_m \sin((m-0.5)k_1h)\right)^2+\left(\sum_{m=1}^{M}\beta_m \sin((m-0.5)k_2h)\right)^2\right]},\end{aligned} \quad \text{(C.12)}$$

or

$$\begin{aligned}\frac{c_{\mathrm{fd}}}{c} &= \frac{w\Delta t}{khr_s}\\ &\approx \frac{2}{khr_s}\arcsin\sqrt{r_s^2\left[\left(\sum_{m=1}^{M}\beta_m \sin((m-0.5)k_1h)\right)^2+\left(\sum_{m=1}^{M}\beta_m \sin((m-0.5)k_2h)\right)^2\right]}.\end{aligned} \quad \text{(C.13)}$$

Acknowledgments

I would like to express my sincere gratitude to my supervisor, Prof. Dr. Thomas Bohlen, for his continuous guidance, patience, and support throughout my thesis. I am also deeply grateful to my co-supervisor, apl. Prof. Dr. Joachim Ritter, for his support of my research.

Furthermore, I want to express my special thanks to all the members of the Applied Geophysics group at the Geophysical Institute (GPI). Your kind assistance, willingness to help, and the welcoming research environment you created have been deeply appreciated.

I also want to extend my thanks to my friends and fellow classmates at KIT, particularly Xikai Wei, Hanzhe Xiao, Yunfeng Liang, Yajian Gao, Jiong Yi, Shuobang Sun and Yijia Chen. Thank you for your companionship and encouragement, which have been invaluable to my progress.

I would also like to acknowledge the Karlsruhe Institute of Technology (KIT) for providing the MATLAB campus license, and GPI for supplying the computing facilities, both of which were essential for conducting the numerical simulations in this work.

Most importantly, my deepest gratitude goes to my family for their unconditional love and financial support, which made my studies possible. Finally, I would like to acknowledge the assistance of ChatGPT and Google Gemini in polishing and refining the English expression of this thesis.